Diving Control and Optimal Design of Semental Lining in Shield Tunneling Method(Dissertation_全文)

AUTHOR(S):

Narentorn Yingyongrattanakul

CITATION:

Narentorn Yingyongrattanakul. Diving Control and Optimal Design of Semental Lining in Shield Tunneling Method. 京都大学, 2002, 博士(工学)

ISSUE DATE:

2002-03-25

URL:

https://doi.org/10.14989/doctor.k9555

Driving Control and Optimal Design of Segmental Lining in Shield Tunneling Method

March, 2002

Narentorn Yingyongrattanakul

Driving Control and Optimal Design of Segmental Lining in Shield Tunneling Method

March, 2002

Narentorn Yingyongrattanakul

ACKNOWLEDGEMENTS

There is no question that I owe a dept gratitude to all those people I met in Kyoto University for what I have learned. I would like to express my gratitude to Professor Toshihisa Adachi. I have benefited enormously from the criticism and advice of him during six years in Japan. I would also like to express my gratitude to the members of my committee, Professor Yuzo Ohnishi and Takeshi Tamura for their valuable suggestions.

I am also deeply indebted to Associate Professor Kazuyoshi Tateyama, who had marvelous understanding of the subject and of myself, without him I would not have been able to complete this works. I would like to express my special gratitude to my academic advisor in Thailand, Assistant Professor Wanchai Teparaksa who offered me in valuable help in different ways.

I wish to express sincere gratitude to Professors Yoshio Nakamura, Fusao Oka and Koichi Ono for their helps and suggestions during my student day in Kyoto University. Special thanks are due to Associate Professors Makoto Kimura, Mamoru Mimura, Hiroyasu Otsu and Takeshi Kodaka for their encouragement in several ways.

I would like to acknowledgement to the cheery encouragement and moral support of Dr. Kiyoshi Kishida and Dr. Keijiro Yamada, the Research Associates at Kyoto University. I am also grateful thank to Mr. Takao Yano for assistance in the experimental works.

Warm thanks go to my colleagues and former colleagues of both Geotechnical Engineering and Urban Infrastructure Systems laboratories at Kyoto University for their support and friendship. They accepted me generously into their classroom, and they will be in my mind all the time. I am also extremely grateful to Mr. Makoto Kurahashi for his assistance and support in my researches. Special thanks go to Dr. Tirawat Boonyatee who sincerely advices me in several ways.

Finally, I would like to thank my parents for their never declining faith in my abilities.

TABLE OF CONTENTS

LIST OF TABLES

LIST OF FIGURES

Chapter 1
INTRODUCTION

1.1 Background

Nowadays the shield tunneling method is considered to be the most popular method for tunneling works in urban areas. This is because it provides high advance rates, exact tunnel profiles, the least impact on surface structures, a high level of safety for workers, and it is environmentally friendly. Up to the present, the movement of shield machines has been controlled by rear jacks thrusting against the segments assembled in the previous steps of construction. The advancing control of shield machines can be determined by controlling the extension of each thrust jack to dig the tunnel along the specified route. In order to program a shield to move precisely along the designated excavation route, it is necessary to adjust the driving forces and the driving moments according to the ground properties of the excavation. Ordinarily, the advancing control of shield machines is mainly based on the measurement results of the previous excavation steps. Recently, however, the methods most widely used to control the excavation processes of shield machines are AI (artificial intelligence) systems such as, Fussy systems. These methods can determine the control forces by learning such previous data as the applied forces, the shield postures, the errors from the designated alignment, etc., and by estimating their correlations. Then, the required driving forces and driving moments for excavating at the next step are estimated. A shield machine occasionally has to excavate near existing underground structures such as group piles, subway stations, and subway tunnels. In these cases, the advancing control of the machine must also be concerned with the effects of its movement, such as ground loosening, additional earth pressure, etc., on the nearby underground structures. The additional pressure caused by the shield movement should be reduced as much as possible. Thus, it is necessary to develop a control method that can consider both the machine moving postures and the effects of the excavation processes. That is to say, a method is required which is able to automatize the directional control of shield machines to move along the designated alignment and to minimize

the effects of the excavation on the surrounding structures. The method is called the *automatic* and *optimum* control method for shield machines.

Recent trends in construction of underground road tunnels include a larger width, a flatter shape and more stability. Due to the rapid expansion of urban areas and traffic requirements, a large cross section is increasingly required for underground road tunnels. The shield tunneling method is one of the most popular methods applied to the construction of underground tunnels in urban areas, because it provides high advance rates, exact tunnel profiles, the least impact on surface structures, a high level of safety for workers, and it is environmental friendly. The tunnel with a large cross section that is considered in this study is a tunnel for a three-lane road for which the width and the area are more than 16 m and 100 m^2, respectively. For this kind of tunnel, a conventional circular-shaped tunnel is impractical because a large shield machine is required, a large amount of soil must be excavated and discarded, and lots of space will be left unutilized. In order to overcome these problems, other types of flat tunnels, namely, elliptical and horseshoe-shaped tunnels, are taken into consideration. Thus a study on the mechanical behavior, and the design method of flat-shaped tunnels is needed. Moreover, with conventional design methods, the lining is designed to be uniform in thickness, having the same thickness over the entire cross section. The stability of a tunnel lining can be improved by increasing its thickness. In this research, the idea of improving the stability of tunnel linings by nonuniformly varying the lining thickness, without increasing the overall lining area, is proposed and proved.

1.2 Objectives

The main objectives of this research are: (1) to simulate the shield excavation processes by the finite element method and to use it for the driving control of shield machines, (2) to investigate the mechanical behavior of flat-shaped tunnels, and (3) to develop a numerical method for determining the optimal shape of tunnel linings.

1.2.1 Simulations of the shield excavation processes by FEM and its application to the driving control of shield machines

The advancement and the excavation processes of a shield machine in three-dimensional space are simulated using the finite element method. The shield-soil interactions are modeled by the

specially defined elements adjacent to the machine. The movement of the shield machine is simulated with finite element remesh techniques after each small step of movement. The driving forces and the driving moments required to control the machine to move along the designated alignment are calculated by summing all the forces acting on the machine. This simulation method is then used to analyze the experimental problems in order to investigate the effects of such excavation conditions as the ground properties, the excavation depth, and the radius of the excavation curve, on the required control forces and moments. Moreover, the application of this simulation method to the automatic advancing control of a shield machine for general excavation work is proposed. Finally, the simulation of a shield tunneling project in Kyoto City is analyzed to compare the numerical results with the data from field measurements.

1.2.2 Experimental study on flat-shaped tunnel linings

Two small-scale loading devices have been developed for conducting the model tests. Model loading tests are carried out to investigate the behavior of flat-shaped tunnels under certain gravity loads. A two-way loading device has been developed to investigate the behavior of the tunnel linings under the adjustable loads. The tests are conducted on three types of flat-shaped tunnels namely circulars, elliptical and horseshoe. The strain and the member force values of the tunnel linings are measured after loading. The effects of various parameters on the stability of the tunnels are investigated and discussed.

Note that these model tests are not used for the purpose of replacing the prototype tests, but are intended to be a tool for a fundamental study on the physical interaction between soil and tunnels during loading. Both types of model tests are conducted under two-dimensional plane strain conditions. The tunnel linings are imaged in a straight alignment, and the effects of the shield movement are not taken into account in this experiment.

1.2.3 Optimal design for the segmental linings

A shape optimization program has been developed with the idea of improving the tunnel stability by varying the lining thickness. The developed code is made as a versatile analytical tool for analyzing the optimal shape for structural and geotechnical problems. A method for applying the optimization program to the design of tunnel linings is proposed.

1.3 Arrangement and outline

In Chapter 2, the general aspects of the shield tunneling method are reviewed and the design method for the tunnel linings of shield tunnels is described. Then, previous studies on tunnel linings including numerical and experimental approaches, are summarized.

In Chapter 3, simulation techniques for the shield excavation processes by FEM in three-dimension space are described. An analyses of the experimental problems are carried out to investigate the excavation conditions for controlling the driving forces and the driving moments of the shield machine. The validity of the proposed method is proved by simulating the above-mentioned excavation project in Kyoto City and comparing the calculated results with the measured data.

The experiments on the flat-shaped model linings and the results are reported in Chapter 4. From the model loading tests, the effects of the tunnel shape, the pattern of the lining thickness, and the overburden depth on tunnel stability are demonstrated and discussed. Two-way loading tests are also carried out to investigate the further behavior of flat-shaped tunnels. Not only the effects of the tunnel shape and the pattern of the lining thickness, but the effects of the lateral pressure ratio are also investigated. The efficiency of nonuniform linings to improve tunnel stability is illustrated.

The development and the application of the optimization program, based on the finite element method, is presented in Chapter 5. The basic theories and the calculation procedures of the structural optimization program are described. Next, the application of the optimization program for analyzing tunnel problems is demonstrated. The validation of the program is proved by analyzing the two-way loading tests and then comparing the analytical results with the experimental data. This chapter also presents an example problem in which the application method uses the optimization program to improve the stability of tunnel linings.

The conclusions drawn from each chapter are summarized in Chapter 6.

Chapter 2
LITERATURE REVIEW

In this chapter, an overview of the shield tunneling method will be described, and then the general design method for tunnel linings will be summarized. Next, the numerical methods for analyzing shield tunneling are presented. Finally, papers describing model tests on tunnel linings are reviewed and discussed.

2.1 General aspects of the shield tunneling method

The shield tunneling method was invented in the United Kingdom by M.T. Brunel in 1818, and was first used in 1825 for constructing a tunnel under the Thames River. The shield is usually made of cylindrical steel in order to prevent the ground from collapsing and to provide adequate space for the excavation and the lining. The shell is supported by ribs and ring girders and is moved by built-in hydraulic jacks. **Figure 2.1** shows the construction sequence of shield tunneling work with the simplified longitudinal sections of a conventional type of shield (Fujita, 1989). Various pieces of equipment and other devices are installed in the shield to make the operation easier. The shield is assembled in a launching shaft, and the construction sequence of the shield tunneling can be described as follows:

1) Excavate ahead for a distance equivalent to the length of one segmental lining, while supporting the tunnel face with jacks and face-supporting pressure.

2) Advance the shield one ring length forward by applying the jack thrust against the lining, which has already been built.

3) Install the segments, each one ring in length, in the shield tail after retracting the jacks.

4) Fill the tail void which has developed between the lining and the open ground by grouting.

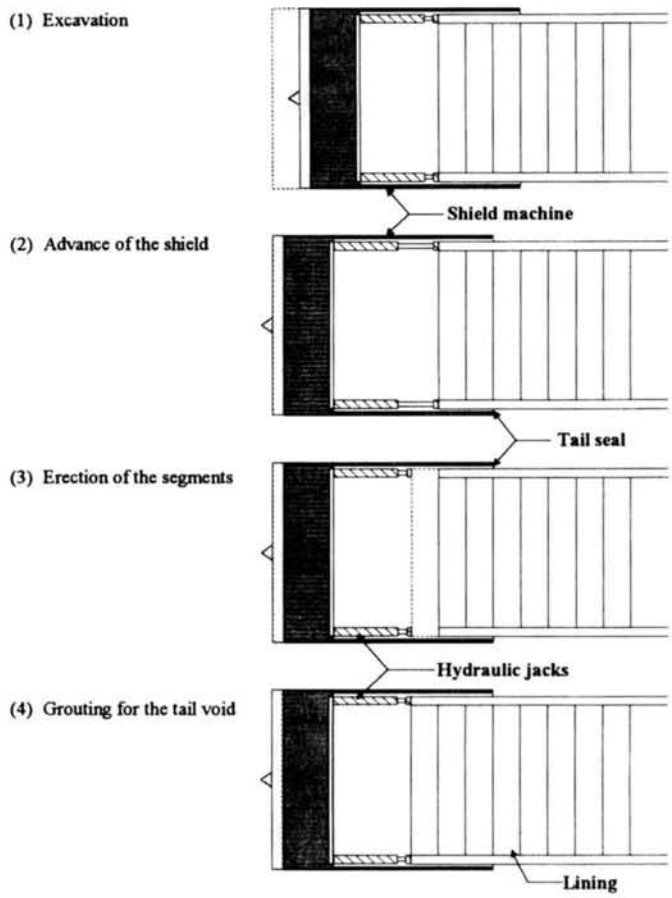

Figure 2.1 Construction sequence of shield tunneling work (Fujita, 1989)

2.2 Design method for the drive unit of shield machines

According to the Japan Society of Civil Engineers (JSCE, 1996), the total thrust of a shield machine shall be determined by summing the various resisting forces against the machine's advancement with a necessary margin. While advancing, a shield machine meets the following resistive forces:

1) Resistance caused by the friction or the adhesion between the outer surface of the shield machine and the ground (F_1)

2) Penetration resistance of cutter bits in the hood section as the machine advances (F_2)

3) Resistance at the cutting face (F_3)

a) Pressure inside the chamber for a closed-face type of shield machine

b) Resistance to the advancement of the cutter head in the case of a mechanical shield machine

c) Reaction from face jacks in the case of manual and semi-mechanical shield machines

4) Resistance to changes in direction (resistance resulting from a curved tunnel route, from making corrections to the directional deviation, or from stabilizers and flaps used to make changes in direction) (F_4)

5) Resistance due to the friction between segments and skin plates at the tail section (F_5)

6) Hauling resistance of the trailing gear

The sum of these resistive forces (ΣF) is given by the following equation. For individual resistance force, in the case of a particular machine type, should be carefully studied to determine the total thrust. A suitable margin should be also allowed.

$$\sum F = F_1 + F_2 + F_3 + F_4 + F_5 + F_6 \tag{2-1}$$

$$F_1 = \begin{cases} \mu_1 \cdot (\pi D_0 \cdot L \cdot P_m + W) \text{.....for sandy soil} \\ c \cdot \pi D_0 \cdot L \text{.....for cohesive soil} \end{cases} \tag{2-2}$$

$$F_2 = l \cdot t \cdot K_p \cdot P_m \tag{2-3}$$

$$F_3 = P_f \frac{\pi}{4} D_0^{\,2} \tag{2-4}$$

$$F_4 = R \cdot S \tag{2-5}$$

$$F_5 = \mu_2 \cdot G_1 \tag{2-6}$$

$$F_6 = \mu_3 \cdot G_2 \tag{2-7}$$

where μ_1 = the coefficient of friction between the steel and the soil

μ_2 =the coefficient of friction between the steel and the steel/concrete

μ_3 = the coefficient of friction between the wheel and the steel

D_0 = the outer diameter of the shield machine

L = the length of the shield machine

W = the weight of the shield machine

G_1 = the weight of the segments

G_2 = the weight of the trailing gear

P_m = the average earth pressure acting on the shield machine

P_f = the pressure acting on the cutting face (such as the reaction acting on the face jacks, the earth pressure acting on the bulkhead, the slurry pressure, etc.)

c = cohesion

K_p = the coefficient of passive earth pressure

R = the resistance to the earth pressure (support force, passive earth pressure, etc.)

I = the perimeter of the cutting face

t = the thickness of the penetrating cutting bits

S = the projected area of the resistance plate in the direction of the advancement

2.3 Design method for the tunnel linings of shield tunnels

This section summarizes the general design method for the tunnel linings of shield tunnels in Japan according to the Japan Society of Civil Engineers (JSCE, 1996). Measurement of the thickness of the primary and the secondary linings in a tunnel cross section are defined in **Figure 2.2**.

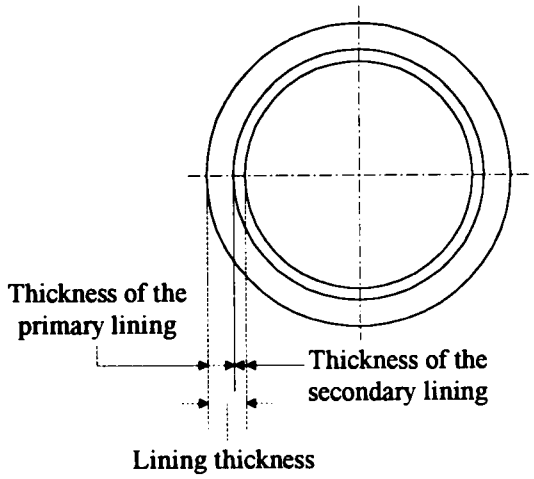

Figure 2.2 Tunnel lining for shield tunnels

Shield tunnels for railways and roads are generally designed by considering the fact that the primary lining, built from segmental rings, is the main structure. It is most common to construct the primary lining with cast-in-place reinforced concrete (RC). The secondary lining is generally constructed for the purposes of corrosion protection, alignment adjustment, waterproofing of the interior lining, vibration protection and protection against the deterioration of its durability. Cast-in-place plain concrete normally used for secondary lining. In this case, the thickness of the secondary lining is usually approximately 15 cm-30 cm.

2.3.1 Design loads

The lining (refer to the primary lining) must be constructed so as to ensure and satisfy its safety and function, not only after the tunnel is ready for use, but also during the construction stage. Various combinations of loads should be considered according to the purposes and the usage of the tunnel. **Table 2.1** presents a classification of the loads that should be considered in the design of tunnel linings.

Table 2.1 Classification of design loads

Primary loads	1. Vertical and horizontal loads 2. Water pressure 3. Dead weight 4. Effects of surcharge 5. Soil reaction
Secondary loads	6. Internal loads 7. Construction loads 8. Effects of earthquakes
Special loads	9. Effects of the consideration of two or more shield tunnels construction 10. Effects of working in the vicinity 11. Effects of ground subsidence 12. Others

Primary loads are the basic loads which always must be considered in the design of tunnel linings. Secondary loads are the loads which act during construction or after the completion of the tunnel. They should be taken into account according to the objectives, the conditions of the construction, and the location of the tunnel. Special loads are loads which should to be specifically considered according to the conditions of the ground and the tunnel usage.

The above loads are generally regarded as static loads, but a dynamic response analysis is also introduced when the effects of an earthquake are being evaluated. The design of linings which reflect the results of such an analysis is becoming popular.

Among the loads listed in **Table 2.1**, construction loads (see secondary loads) such as the thrust force of the shield jacks and the backfill grouting pressure, etc., as well as the effects of earthquakes, are short-term loads. However, since primary loads can also experience changes in their loading condition on the lining during the tunnel operation, decisions regarding design loads should be made giving due consideration to these loading conditions.

Hence, this article only gives a basic stance for the design concepts of tunnel linings. Only the primary loads, which are the most important loads, are described. The primary loads acting on a circular tunnel with the usual calculation method and the modified usual calculation method, are shown in **Figure 2.3**.

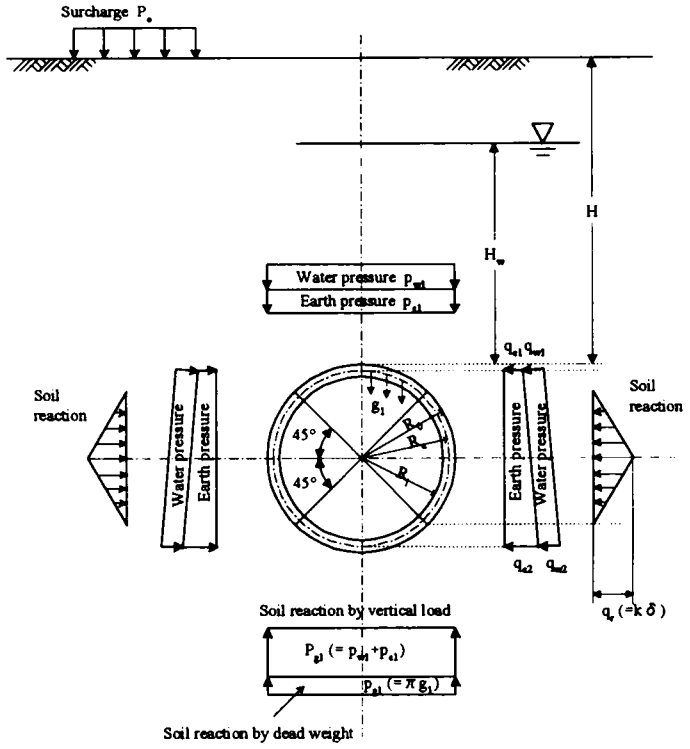

Figure 2.3 The primary loads with the usual calculation method and the modified usual calculation method (effective stress method)

Vertical and horizontal earth pressure

Calculation of earth pressure

There are two ideas for evaluating earth pressure. One is to separate the groundwater pressure from the soil pressure (effective stress method) and the other is to include the groundwater pressure with the soil pressure (total stress method). In general, the effective stress method tends to be used for sandy soil while the total stress method tends to be adopted for cohesive soil. As for the unit weight of soil, the wet unit weight is used for the levels above the ground water and the submerged unit weight is used for the levels below the groundwater with the effective stress method. While the total stress method, the wet unit weight is used for levels above the ground water, but the unit weight including water is used for levels below the groundwater.

Vertical earth pressure

For a tunnel with an overburden which is smaller than the tunnel diameter, it is common not to expect the arch action effect of the soil. When the overburden is larger than the tunnel diameter, it is possible to adopt the loosening pressure for the design vertical earth pressure since trust can be comparatively be put on the arch effect of the soil. With sandy soil, the loosening pressure is often adopted if the overburden is 1-2D_0 or more (D_0 is the outside of the segmental ring). With cohesive soil, the loosening pressure is often adopted if the depth of the overburden is 1-2 D_0 or more and the tunnel is in stiff clay ($N \geq 8$). With medium stiff clay ($4 \leq N < 8$) or soft clay ($2 \leq N < 4$), the loosening pressure is not adopted and the weight of the full overburden is considered.

The expression proposed by Terzaghi (1943), shown in **Figure 2.4**, is generally used for the calculation of the loosening pressure. When the loosening pressure is adopted as the vertical earth pressure, a lower limit is often specified in consideration of the changes in loading during the construction process and after the completion of the tunnel. The lower limit of the vertical earth pressure differs according to the usage of the tunnel.

To calculate the loosening pressure in a ground composed of multiple soil layers, the ground is assumed to be monolithic, based on a predominant soil layer among the layers, or the loosening pressure is directly calculated based on the alteration of the strata.

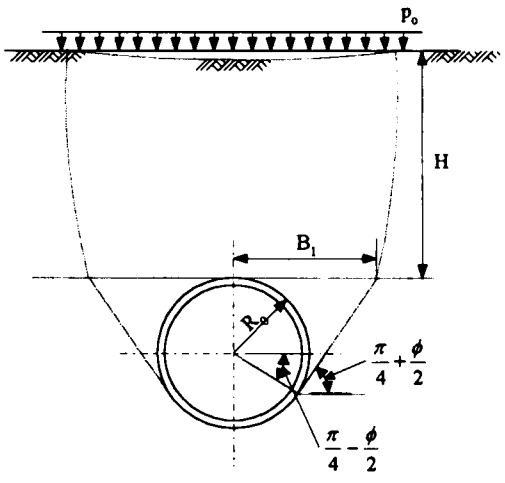

$$\sigma_v = \frac{B_1(\gamma - c/B_1)}{K_0 \tan\phi} \cdot \left(1 - e^{-K_0 \tan\phi H/B_1}\right) + p_0 \cdot e^{-K_0 \tan\phi H/B_1}$$

$$B_1 = R_0 \cdot \cot\left(\frac{\pi/4 + \phi/2}{2}\right)$$

σ_v: Terzaghi's loosening pressure
h_0: Converted height of the loosening soil ($= \sigma_v / \gamma$)
K_0: Ratio of horizontal earth pressure to vertical earth pressure (usually 1.0 can be adopted as K_0)
ϕ: Internal friction angle of the soil
p_0: Surcharge
γ: Unit weight of the soil
c: Cohesion of the soil

However, when p_0/γ is small compared with H, the loosening pressure can be calculated using the following equation:.

$$\sigma_v = \frac{B_1(\gamma - c/B_1)}{K_0 \tan\phi} \cdot \left(1 - e^{-K_0 \tan\phi H/B_1}\right)$$

Figure 2.4 Loosening pressure (Terzaghi, 1994)

The loosening pressure for sections other than the circle can also be calculated from Terzaghi's expression if the loosening width (B_1) can be suitably evaluated. The distribution of load, however, needs to be carefully decided because it may vary according to the configuration of the tunnel's cross section.

Horizontal earth pressure

The design vertical pressure, determined with the total stress method can be assumed to be a surcharge acting on the horizontal plane at the tunnel crown. The horizontal earth pressure can generally be determined by multiplying the vertical earth pressure by the coefficient of the lateral earth pressure. When a soil reaction can not be expected, it is possible to select the coefficient of earth pressure at rest as the coefficient of lateral earth pressure. When a soil reaction can be expected, it is usual to adopt a reduced coefficient of earth pressure at rest. The coefficients of lateral earth pressure and the coefficient of soil reaction for each ground condition are shown in **Table 2.2**.

Water pressure

The groundwater level shall be determined by figuring out which design is safer in terms of the possible changes in the groundwater level during and after construction. The vertical water pressure shall be a uniformly distributed load and its magnitude shall be the hydrostatic pressure acting on the highest point of the tunnel crown and the hydrostatic pressure acting on the lowest point of the tunnel bottom. The horizontal water pressure shall be a uniformly distributed load and its magnitude shall be the hydrostatic pressure.

Table 2.2 Coefficients of lateral earth pressure and soil reaction

Design methods	Ground conditions	λ	k (kN/mm^3)	Approx. N-value
Effective stress method	Very dense sandy soil	0.35-0.45	30-50	$30 \leqq N$
	Medium dense sandy soil	0.45-0.55	10-30	$15 \leqq N < 30$
	Loose sandy soil	0.50-0.60	0-10	$N < 15$
	Hard cohesive soil	0.35-0.45	30-50	$25 \leqq N$
	Stiff cohesive soil	0.45-0.55	10-30	$8 \leqq N < 25$
	Medium stiff cohesive soil	0.45-0.55	5-10	$4 \leqq N < 8$
Total stress method	Medium stiff cohesive soil	0.55-0.65	5-10	$4 \leqq N < 8$
	Soft cohesive soil	0.65-0.75	0-5	$2 \leqq N < 4$
	Very soft cohesive soil	0.75-0.85	0	$N < 2$

Dead weight

Dead weight is a load in the vertical direction which is distributed along the centroid of the lining. The dead weight of the primary lining shall be calculated by the following equation:

$$g_1 = \frac{W_1}{2\pi \cdot R_c} \tag{2-8}$$

where g_1 is the dead weight in unit length of the primary lining exerted along the centroid of the lining per unit length in a longitudinal direction, W_1 is the dead weight of the primary lining per unit length in a longitudinal direction, and R_c is the radius of the centroid of the primary lining

Effects of surcharge

The effects of surcharge shall be determined if the tunnel is located near roads or buildings. To calculate the transmission of stress in the ground, the available methods include "Boussinesq's equation" and Westergaard's equation" (Boussinesq, 1883; Westergaard, 1938). Numerical analyses, such as FEM etc, are also available.

Soil Reaction

The extent of the generation, the shape of the distribution, and the intensity of the soil reaction shall be determined in connection with the design calculation method being employed, which will be described in the next section.

2.3.2 Structural calculation of segmental linings

Member forces depend on load conditions, especially the soil reaction, as well as the modeling of the segmental ring structure. These conditions shall be clearly defined. Since a segmental ring consists of several segments assembled by bolts, its deformation tends to be larger than that of a ring with uniform bending rigidity which has the same rigidity as the main section of a segment. This is because the rigidity of joints is lower than that of the main section of a segment. Thus, it is important to determine how to evaluate decreases in the rigidity of joints in order to calculate the member forces. Moreover, since bolts are used to connect the segment joints and ring joints are staggered in Japan, it is very important to evaluate the effects of the adjacent rings for the design calculation. Schematic drawings of the structural models of the segmental rings are shown in **Figure 2.5**, and the design load distributions proposed for these models are shown in **Figure 2.6**.

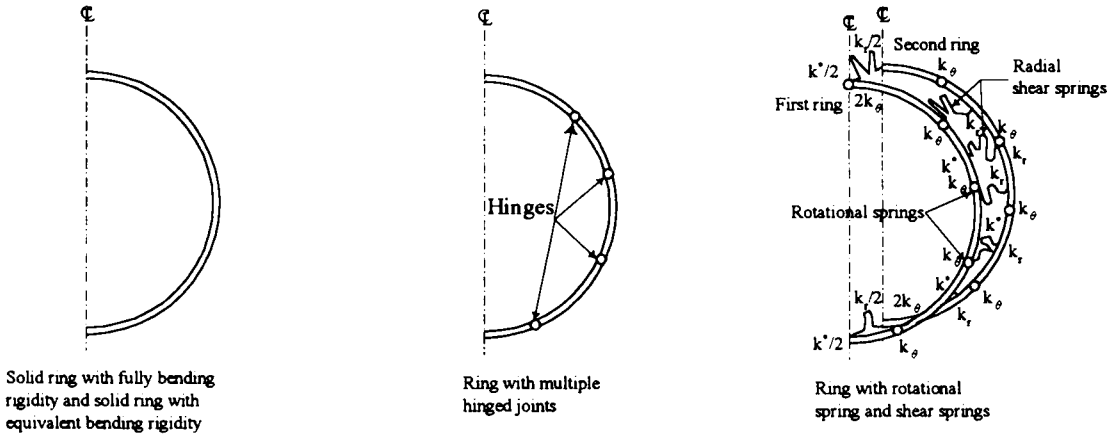

Figure 2.5 Schematic drawings of the design models

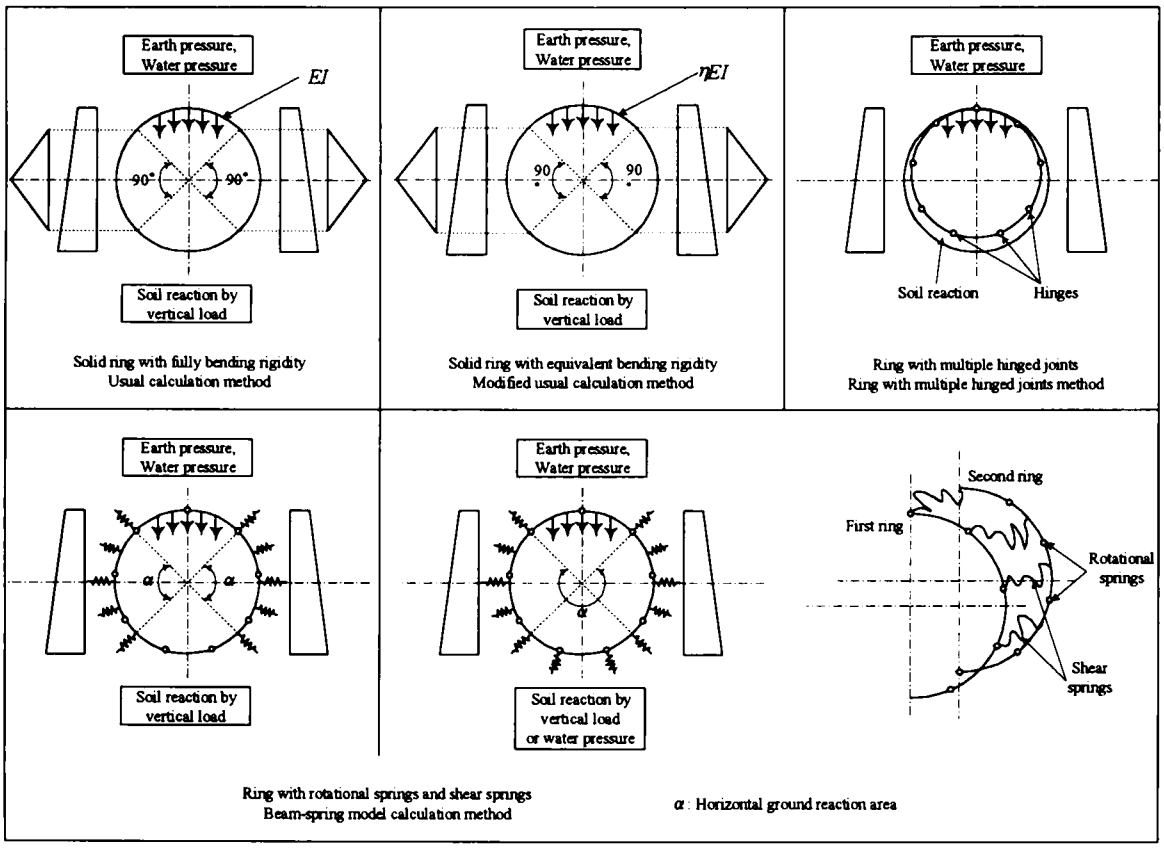

Figure 2.6 Design load distributions proposed for the above models

The models for the design calculations are classified by joint evaluations and soil-structure interactions, as explained below.

Usual calculation method

This method was proposed in about 1960 and has been widely used in Japan. A common load distribution model for this method is shown in **Figure 2.3**, where the soil reaction in a vertical direction is uniform and the soil reaction in a horizontal direction is triangularly distributed between 45° and 135° from the crown to both sides.

The segmental rings are assumed to be rings with uniform bending rigidity EI, where E is the modulus of elasticity for the lining and I is the moment of inertia for the lining. The decrease in the rigidity of the segment joints is ignored. This ring model is the *solid ring with fully bending rigidity* model.

The horizontal deformation of a ring at the spring line, which will determine the magnitude of the horizontal soil reaction, differs according to, whether the fact that the soil reaction derived from the dead weight of the lining is considered or not. Equations to calculate the member forces are shown in **Table 2.3**.

Table 2.3 Equations to calculate the member forces with the usual calculation method and the modified usual calculation method

Load	Bending moment	Axial force	Shear force
Vertical load $(p_{e1} + p_{w1})$	$M = \frac{1}{4}(1 - \sin^2\theta)(p_{e1} + p_{w1})R_c^2$	$N = (p_{e1} + p_{w1})R_c \cdot \sin^2\theta$	$Q = -(p_{e1} + p_{w1})R_c \cdot \sin\theta \cdot \cos\theta$
Horizontal load $(q_{e1} + q_{w1})$	$M = \frac{1}{4}(1 - 2\cos^2\theta)(q_{e1} + q_{w1})R_c^2$	$N = (q_{e1} + q_{w1})R_c \cdot \cos^2\theta$	$Q = (q_{e1} + q_{w1})R_c \cdot \sin\theta \cdot \cos\theta$
Horizontal triangular load $(q_{e2} + q_{w2} - q_{e1} - q_{w1})$	$M = \frac{1}{48}(6 - 3\cos\theta - 12\cos^2\theta + 4\cos^3\theta)(q_{e2} + q_{w2} - q_{e1} - q_{w2})R_c^2$	$N = \frac{1}{16}(\cos\theta + 8\cos^2\theta - 4\cos^3\theta)(q_{e2} + q_{w2} - q_{e1} - q_{w2})R_c$	$Q = \frac{1}{16}(\sin\theta + 8\sin\theta \cdot \cos\theta - 4\sin\theta \cdot \cos^2\theta)(q_{e2} + q_{w2} - q_{e1} - q_{w2})R_c$
Soil reaction $(q_r = k \cdot \delta)$	$0 \le \theta < \frac{\pi}{4}$ $M = (0.2346 - 0.3536\cos\theta)k \cdot \delta \cdot R_c^2$ $\frac{\pi}{4} \le \theta \le \frac{\pi}{2}$ $M = (-0.3487 + 0.5\sin^2\theta + 0.2357\cos^3\theta)k \cdot \delta \cdot R_c^2$	$0 \le \theta < \frac{\pi}{4}$ $N = 0.3536\cos\theta \cdot k \cdot \delta \cdot R_c$ $\frac{\pi}{4} \le \theta \le \frac{\pi}{2}$ $N = (-0.7071\cos\theta + \cos^2\theta + 0.7071\sin^2\theta \cdot \cos\theta)k \cdot \delta \cdot R_c$	$0 \le \theta < \frac{\pi}{4}$ $Q = 0.3536\cos\theta \cdot k \cdot \delta \cdot R_c$ $\frac{\pi}{4} \le \theta \le \frac{\pi}{2}$ $Q = (\sin\theta \cdot \cos\theta - 0.7071\cos^2\theta \sin\theta)k \cdot \delta \cdot R_c$
Dead load $(p_{g1} = \pi \cdot g_1)$	$0 \le \theta < \frac{\pi}{2}$ $M = (\frac{3}{8}\pi - \theta \cdot \sin\theta - \frac{5}{6}\cos\theta)g \cdot R_c^2$ $\frac{\pi}{2} \le \theta \le \pi$ $M = (-\frac{1}{8}\pi + (\pi - \theta)\sin\theta - \frac{5}{6}\cos\theta - \frac{1}{2}\pi \cdot \sin^2\theta)g \cdot R_c^2$	$0 \le \theta < \frac{\pi}{2}$ $N = (\theta \cdot \sin\theta - \frac{1}{6}\cos\theta)g \cdot R_c$ $\frac{\pi}{2} \le \theta \le \pi$ $N = (-\pi \cdot \sin\theta + \theta \cdot \sin\theta + \pi \cdot \sin^2\theta - \frac{1}{6}\cos\theta)g \cdot R_c$	$0 \le \theta < \frac{\pi}{2}$ $Q = (\theta \cdot \cos\theta + \frac{1}{6}\sin\theta)g \cdot R_c$ $\frac{\pi}{2} \le \theta \le \pi$ $Q = ((\pi - \theta)\cos\theta - \pi \cdot \sin\theta \cdot \cos\theta - \frac{1}{6}\sin\theta)g \cdot R_c$
Horizontal deformation of a ring at the spring line (δ)	Without considering the soil reaction derived from the dead weight of the lining: $\delta = \frac{\{2(p_{e1} + p_{w1}) - (q_{e1} + q_{w1}) - (q_{e2} + q_{w2})\}R_c^4}{24(\eta \cdot EI + 0.0454k \cdot R_c^3)}$ Considering the soil reaction derived from the dead weight of the lining: $\delta = \frac{\{2(p_{e1} + p_{w1}) - (q_{e1} + q_{w1}) - (q_{e2} + q_{w2}) + \pi g\}R_c^4}{24(\eta \cdot EI + 0.0454k \cdot R_c^3)}$ EI: Bending rigidity in the unit width		

Modified usual calculation method

Although it was known in the 1960s that a staggered arrangement could reinforce segment joints weak in rigidity it was not known how to evaluate the effects of adjacent rings. Since then, many load tests have been conducted to obtain deformation data on segmental rings with bolt joints. The concept of a coefficient of the effective ratio of bending rigidity (η) was introduced by scrutinizing test results and theoretical analyses.

Segmental rings are assumed to be rings with uniform bending rigidity, as in the usual calculation method. However, the coefficient of the effective ratio of bending rigidity ($\eta \leq 1$) is introduced to evaluate the rigidity of the joints. The rings are treated as being uniform, but less rigid. A bending moment is represented as ηEI. The redistribution of bending moments is then expressed by introducing a transfer ration of bending moment ζ. The moment of the main section is calculated as $(1+\zeta)\mathbf{M}$ and the moments of the segment joints are calculated as $(1-\zeta)\mathbf{M}$. This ring model is the *solid ring with equivalent bending rigidity* model.

This calculation model is a logical model for expanding the applications of the "usual calculation method". If a common load distribution is used, and $\eta = 1$, and $\zeta = 0$ are substituted, it becomes the same as the solid ring with fully bending rigidity.

Rings for the multiple-hinged joint calculation method

This is a method utilized under good ground conditions. It is widely used in the UK and in Russia. The segment joints are treated as hinges; thus the segmental rings are assumed as rings with many hinges. Segments are erected so that their joints are in a straight joint arrangement in expectation of ground reactions due to the ring deformation.

Beam-spring model calculation method

This is a method used to evaluate reductions in the bending rigidity and the splice effects of the staggered arrangement using a model in which a segment is considered to be a curved beam or a straight beam, the segment joint is thought of as a rotational spring, and the ring joint is considered to be a shear spring. As described in **Figure 2.6**, the beam-spring model has other modified types. One uses a soil spring to represent the soil reaction in vertical direction and the other is using small springs to represent reactions of its dead weight. With these calculation

methods, the iterative calculation assumes that the soil springs are used according to Winkler's hypothesis.

This method is widely used for roads and railroad tunnels with large diameters. It is also applied to tunnels with small diameters, which have complicated design conditions, or to evaluate the calculation results of the usual calculation method and the modified usual calculation method.

2.3.3 Shapes and dimensions of segmental lining

Bending moment (M), axial force (N), and shear force (Q) are determined from the member forces described in the previous section. The stress intensity at the surface of a tunnel lining can be calculated using the following equations:

$$\sigma = \frac{N}{A} \pm \frac{Md}{2I} \tag{2-9}$$

$$\tau = \frac{Q}{bjd} \tag{2-10}$$

where σ is the circumferential stress at the lining surface, τ is the shear stress at the lining surface, d is the lining thickness, jd is the moment arm of the lining section, b is the lining width, A is the cross sectional area, and I is the moment of inertia. The positive sign means compressive stress, while the negative sign stand for tensile stress.

Table 2.4 Allowable stress levels for concrete

Specified compressive strength		σ_{ck}	42	45	48	51	54
Allowable compressive stress for the bending moment		σ_{ca}	16	17	18	19	20
Allowable standard shearing stress	Shear stress by bending	τ_a	0.71	0.73	0.74	0.76	0.77
Allowable bond stress (deformed bar)		τ_0	2.0	2.1	2.1	2.2	2.2
Allowable bearing stress	Overall loading	σ_{ba}	15	16	17	18	19
	Local area loading	σ_{ba}	$\sigma_{ba} \le 1/2.8 \cdot \sigma_{ck}\sqrt{A/A_a}$ only $\sigma_{ba} \le \sigma_{ck}$				

The shape and the dimensions of a tunnel lining should be designed such that the compressive stress occurring at the lining surface does not exceed the allowable stress, as shown in **Table 2.4**. A reinforced steel bar should be added to withstand the tensile stress and the shear stress if the shear stress exceeds the allowable shearing stress of the concrete.

2.4 Numerical analysis for shield tunneling works

Tunneling inevitably causes ground movement, which in turn induces the local deflections and corresponding additional stress to existing buried and surface structures. Excessive stress levels and deflections may lead to the failure of the structures. The problem of ground behavior, due to tunneling, is one of the most typical soil-structure interaction problems. With this problem, the ground stiffness and the structural stiffness are the key factors affecting the behavior of the soil-structure systems. Thus, it is important to consider the size, the depth, and the materials of the structures in the design. Three design approaches which are commonly adopted are (1) the subgrade reaction method which is known as the Winkler model, (2) analytical methods, and (3) numerical methods such as the finite element method (FEM), the boundary element method (BEM), etc., which incorporate various soil models, different configurations, and different construction sequences. The analytical methods for analyzing the member forces in a segmental lining are described in the previous section. Numerical methods, especially FEM, can be applied to simulate the complex construction sequence and to determine the many effects of shield excavating on the surrounding structures. FEM is also widely used to evaluate the results of calculation obtained from the analytical methods. In this section, previous works of some shield tunneling simulations using FEM are described.

2.4.1 Analysis taking tail void size into consideration

Yamada et al. (1979) proposed a model, shown in **Figure 2.7**, to explain the release of stress by taking the tail void size and the segment rigidity into consideration. This model constrained the ground displacement to the size of the tail void in the FE analysis of an unsupported tunnel. The final displacement was achieved as the sum of the aboveground displacement and the displacement due to the segment deformation. It was also argued that a fairly realistic ground settlement analysis could be conducted by setting the ground's loosening zone and the

deformation coefficient in view of the ground disturbance caused by the advancement of the shield (Makata 1980).

Sakajo et al. (1996) studied the settlement induced by the tail void closure and the consolidation settlement using an FE analysis, for which the stress release and the enforced displacement around the tunnel were taken into account. This proposed method, where schematic method is shown in **Figure 2.8**, is similar to that studied by Mori and Akagi (1980, 1983), as shown in **Figure 2.9**. They suggested that the model based on the total stress, using an elastic soil model, was promising for predicting the ground movement in a two-dimensional FE analysis. The simulation was based on the effective stress, using an elasto-plastic soil model, and could explain the soil behavior due to the shield tunneling as well. Inokuma and Fujimoto (1996) proposed an FE analysis, which takes into account of the backfill grouting process and which has a major impact on the amount of tail void settlement, using a released force equivalent to that of the excavation. This analysis applied a released force equivalent to the rest of the initial stress after subtracting the injection pressure of the backfill grouting.

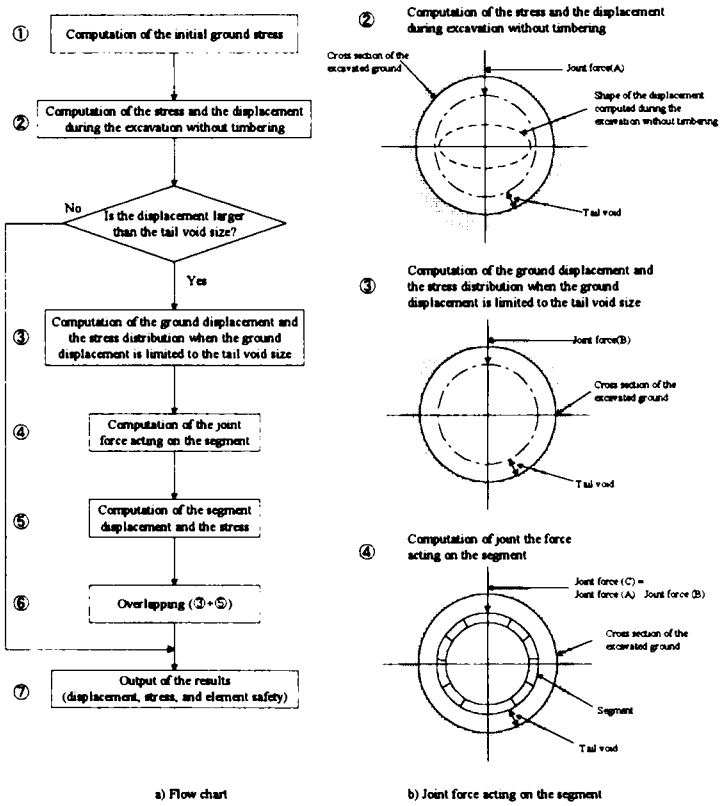

Figure 2.7 Model for analyzing the tail void size and the segment rigidity (Yamata et al., 1979)

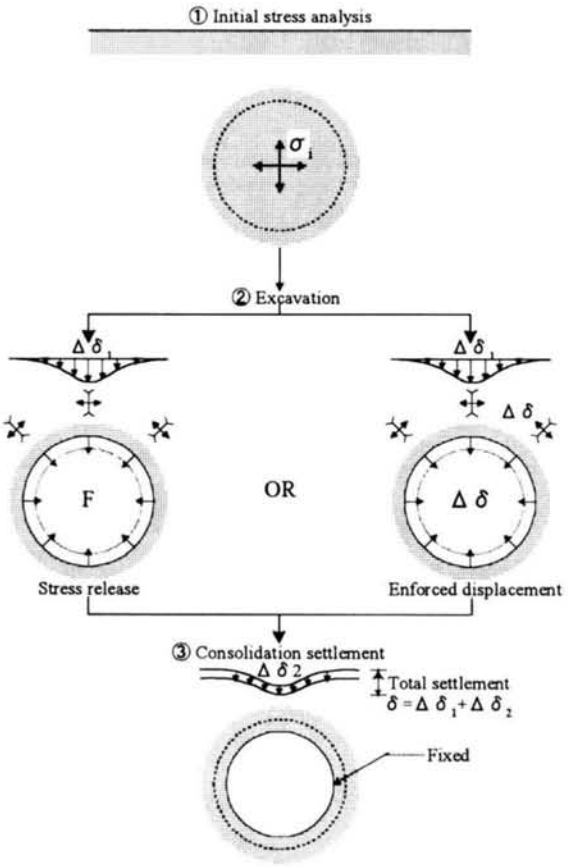

Figure 2.8 Proposed technique to predict the ground deformation in shield tunneling (Sakajo et al., 1996)

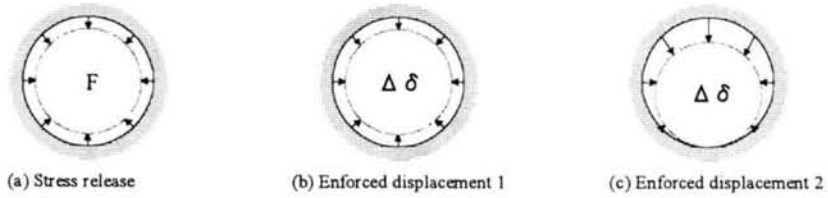

Figure 2.9 Various models used to analyze the shield tunneling excavation (Mori and Akagi, 1980, 1983)

2.4.2 Analysis using the rate of stress release

Furuyama et al. (1980) proposed a method to reduce the driving external force by introducing an appropriate rate of stress release based on the soil intake volume and the tail void volume. The rate of stress release was empirically determined from the results of previous works and from a reverse analysis of the actual measured data. Mair et al. (1981) studied the deformation levels

under undrained conditions and the temporary supported pressure in shallow tunnels in soft clay. The two-dimensional FE analysis was carried out with a program incorporating the Modified Cam-Clay (MCC) model. This study found that the MCC model was not suitable for anisotropic consolidated clay or for the 'dry' side of the critical state to predict the results of tunneling centrifuge model tests.

Stallebras et al. (1994) studied the deformation around shallow and deep tunnels constructed in stiff overconsolidated soil by using the CRISP (CRItical State Program) FE program. In order to accurately simulate the soil behavior, the three-surface kinematic hardening model was used in the analysis. The study demonstrated that the recent stress history of a soil has an important effect on the prediction of surface settlement troughs for both deep and shallow tunnels. In this study, the excavation of a tunnel was simulated by replacing the elements in the tunnel by nodal forces at the boundary which reduce the forces by 40%.

Hergarden et al. (1996) studied the influence of shield tunneling on adjacent and overlying structures through the centrifuge model tests and a two-dimensional FE analysis, of which the Mohr-Coulomb model was applied to Spesswhite Kaolin clay. The analysis was applied by imposing a uniformly distributed fictive load along the outer boundary of the tunnel as volume loss. They pointed out that if the soil parameters are determined carefully, a two-dimensional FE analysis could be used to accurately estimate the ground surface settlement directly after imposing the volume loss of the tunnel. Simpson et al. (1996) studied the FE analysis of the Heathrow Express trial tunnel using non-linear and anisotropic soil models. They showed that, in practice, the calculated widths of the settlement troughs agreed well with those of the observations. In this study, the tunneling was represented by removing the weight of the soil within the tunnel and reducing the stress in proportion to the initial values until the volume of ground loss was equal to that measurement.

2.4.3 Analysis taking external force into consideration

Nagamura et al. (1986) argued that the release of stress at the face was negligible in the case of a slurry shield excavated in a stiff ground, and that the settlement could be mainly simulated by the elastic deformation of the tail void. According to this model, Nagayama et al. (1988) proposed

the model shown in **Figure 2.10**, for which the tail void deformation was governed by the slurry pressure.

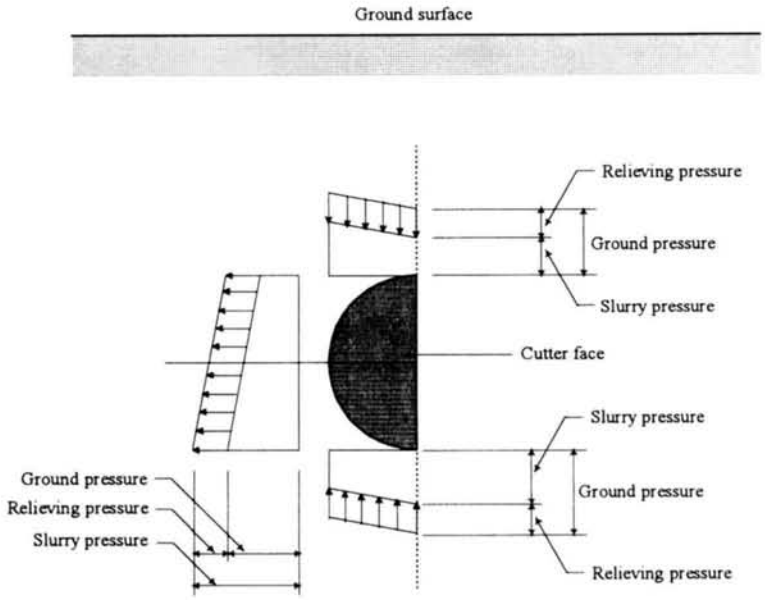

Figure 2.10 Proposed model to analyze the slurry shield tunneling method (Nagayama et al., 1988)

2.5 Model tests on tunnel linings

Model testing is broadly used to study the mechanical behavior of tunnel linings. Two-dimensional model tests can be applied effectively to determine the section force in the tunnel lining model. In this section, papers which cover the model testing of tunnel linings are reviewed and discussed.

Sakurai et al. (1994) studied the surface subsidence and the earth pressure acting on a tunnel lining due to the loosening of the ground in the case of shallow tunnels. A aluminum bars were used to simulate the ground material, and the air pressure was gradually reduced from a certain level to represent the excavation of the tunnel. An outline of the experimental equipment is shown in **Figure 2.11**. The heights of the loosening zone obtained from these tests all agree well with these in Terzaghi's theory. Imanishi et al. (1999) also used aluminum bars as the ground material to simulate a shield excavation. They applied a method of trapdoor testing and the deformation of a lining model to study the influences of excavating on an existing tunnel lining.

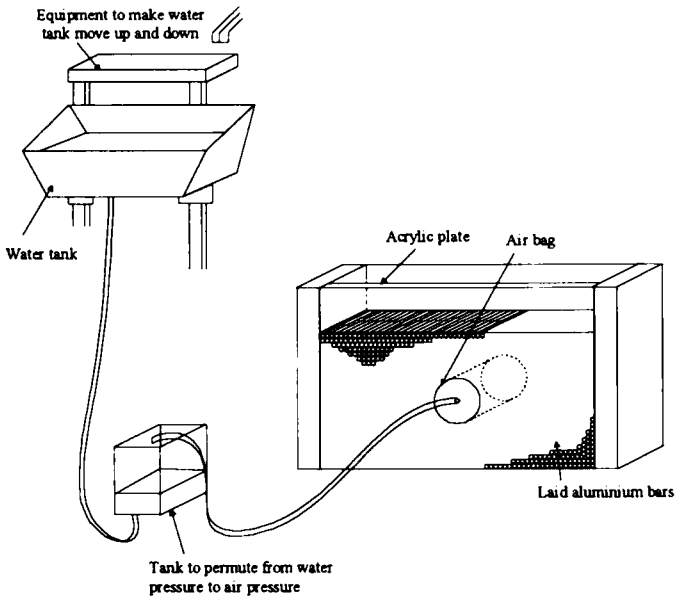

Figure 2.11 Devices developed for the model tests to simulate a tunnel excavation (Sakurai et al., 1994)

Kimura and Koizumi (1999) developed lateral loading model tests for the tunnel linings to be carried out in a sandbox in order to evaluate the interaction between the deformation of tunnel lining and the earth pressure acting upon it. The sand was loaded by screw jacks in vertical and horizontal directions, as shown in **Figure 2.12**. From the tests, the interaction between the ground and the tunnel lining can be explained by introducing of the active and passive ground spring constants as a response to the working realm. The same equipment was also used to study the mechanical behavior of a non-circular shaped tunnel (see e.g., Ohnishi et al., 1996; Takamoto et al., 1996). The lateral loading model testing method was also applied to study the relations among the materials of the lining model and the member forces by Okano et al. (1997).

In addition, Cao et al. (1993) developed the testing device shown in **Figure 2.13** to study the mechanical behavior of elliptical tunnels. The sand is loaded by a pressure bag covered four sides of the soil chamber. The results of these tests show that the concentrated stress occurring at the spring line of the tunnel lining can be effectively reduced by increasing the thickness of the spring line.

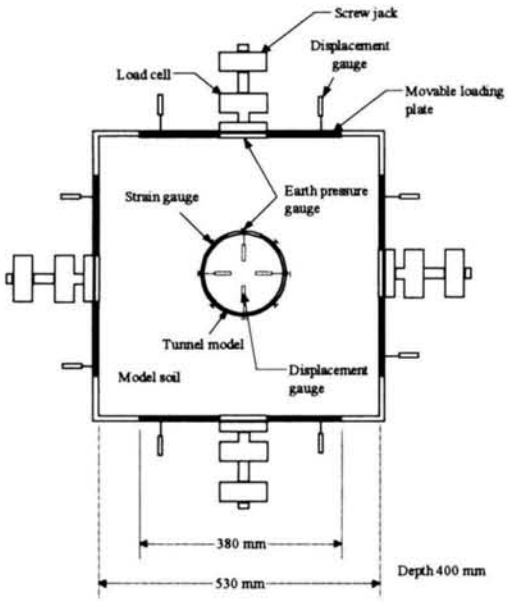

Figure 2.12 Lateral loading model testing device (Kimura and Koizumi, 1999)

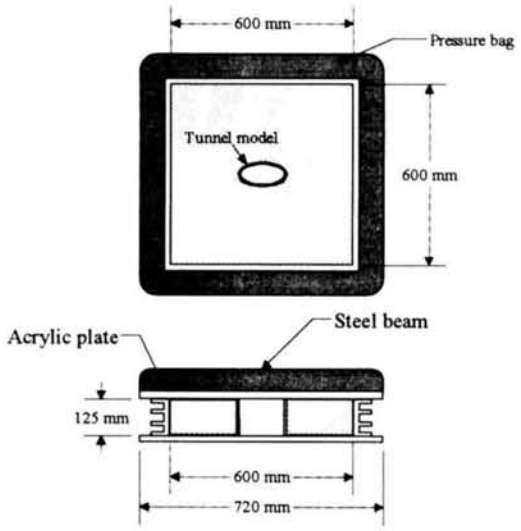

Figure 2.13 Loading model testing device (Cao et al., 1993)

Hisatake and Shibuya (1999, 2000) studied the effects of frictional forces occurring at the surface of the soil chamber using theoretical and experimental approaches. They concluded that the results, namely, stress, strain and displacement levels greatly depend on the size of the soil chamber. Furthermore, they proposed a calculation method for determining the size of the soil chamber that can minimize the errors caused by the frictional forces.

Centrifuge testing is also broadly used to study the earth pressure acting on tunnel linings. Sugiyama et al. (1999) studied the lining stress mechanism of a large circular tunnel in the case of a shallow excavation under a 50 g-centrifuge acceleration, while Ishimura et al. (1992) tested an elliptical tunnel under a 200 g-centrifuge acceleration. Sugihara et al. (1997) carried out a series of centrifugal tests to evaluate the earth pressure on a double-faced shield segment in a sandy ground. For centrifuge tests, the measured earth pressure acting on a tunnel lining is generally compared with the analytical data based on Terzaghi's theory, and then the correlations are proposed.

Chapter 3

SIMULATIONS OF THE SHIELD EXCAVATION PROCESSES BY FEM AND ITS APPLICATION TO THE DRIVING CONTROL OF SHIELD MACHINES

3.1 Introduction

In this chapter, the advancement and the excavation processes of a shield machine in three dimensional space are simulated using the finite element method. The shield-soil interactions are modeled by the specially defined elements adjacent to the machine. The movement of the shield machine is simulated with finite element remesh techniques after each small step of movement. The driving forces and the driving moments required to control the machine to move along the designated alignment are calculated by summing all the forces acting on the machine. Then, this simulation method is used to analyze the experimental problems in order to investigate the effects of such excavation conditions as ground properties, excavation depth, and the radius of the excavation curve, on the required driving forces and driving moments. Moreover, the simulation of a shield tunneling project in Kyoto City is analyzed to compare the numerical results with the data from field measurements. Finally, the application of this simulation method to the automatic driving control of a shield machine for general excavation work is proposed.

3.2 Finite element model

In this section the general aspects of the developed program are first outlined. Next, the constitutive equations for the materials used in this analysis are presented. Finally, a method for rearranging the finite element mesh method is described.

3.2.1 Outline of the analysis method

In order to simulate the shield excavation processes, a computer program has been developed for the three-dimensional finite element analysis, written in C++ Language. The specially defined finite elements, namely, the excavated, the interface, and the elongation elements, are introduced and applied to model the materials adjacent to the shield machine. An outline of the elements used in this simulation model and their properties are shown in **Figure 3.1** and **Table 3.1**, respectively. The shield machine is defined as a rigid boundary for which each node is controlled to move along the designated route. Acting forces at each node of the shield boundary are summed to obtain the total force acting on the shield machine. After a distance of movement, the analysis mesh is rearranged to avoid excessive mesh distortion. Then, the calculation is repeated using the same procedure. A flowchart of the calculation procedure is shown in **Figure 3.2**.

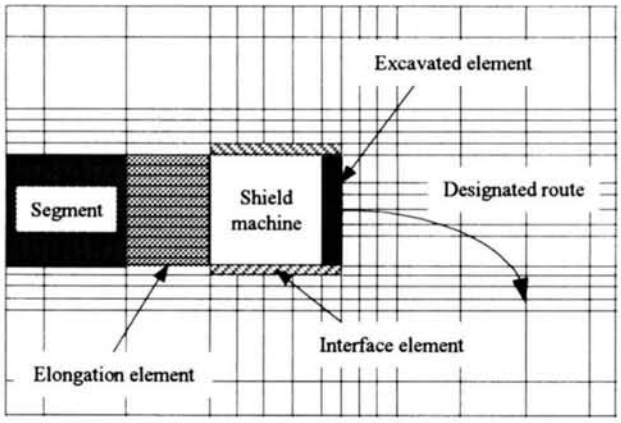

Figure 3.1 Model of elements used in the simulation model

Table 3.1 Properties of elements used in the analysis

Element name	Material type
Shield	Rigid boundary
Segment	Elastic
Elongation	Transverse isotropic elastic
Soil	Elasto-plastic Drucker-Prager and tension limiting
Interface	Transverse isotropic with the Mohr-Coulomb yield criteria
Excavated	Elastic

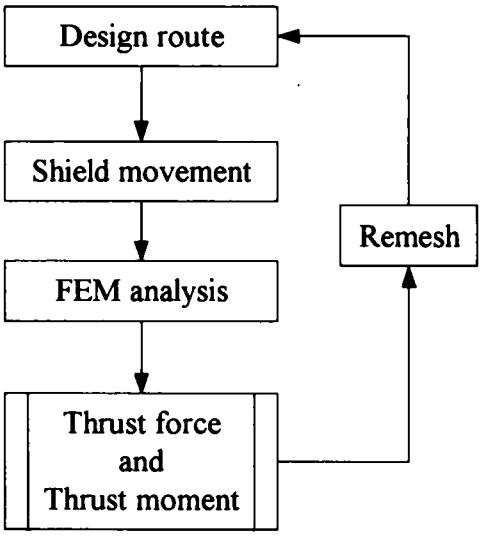

Figure 3.2 Flowchart of the calculation procedure

In this analysis, all finite elements are isotropic eight-node hexahedral elements. All fields, velocities, stress levels, etc., are assumed to be continuous over the element borders. This differs from common finite element programs where quantities like stress levels, etc. can show jumps over element borders. This continuity gives a more diffuse, but also a more stable, numerical scheme. In addition, all fields, velocities, stress values, etc., are stored in the element nodes. This also differs from common finite element programs for which all calculation fields are stored in integration points (Gauss points). This method leads to a relatively easy implementation of the remeshing and the refining techniques.

3.2.2 Properties and constitutive equations for the finite elements

Ground elements

The constitutive equation used for the ground materials is based on the Drucker-Prager model (1952). We selected this model because it requires few ground parameters, yet it still provides a rational explanation for the soil behavior.

As for the simple elastic material, the relation of stress and strain is defined by two parameters, namely, Young's modulus (E) and Poisson's ratio (ν). Strain can be translated into stress by multiplying it by elasticity matrix D, as shown in **Equation 3-1**, in other words,

$$\sigma = D\varepsilon \tag{3-1}$$

or in matrix notation,

$$\begin{bmatrix} \sigma_{xx} \\ \sigma_{yy} \\ \sigma_{zz} \\ \tau_{xy} \\ \tau_{yz} \\ \tau_{zx} \end{bmatrix} = \begin{bmatrix} \lambda+2G & \lambda & \lambda & 0 & 0 & 0 \\ \lambda & \lambda+2G & \lambda & 0 & 0 & 0 \\ \lambda & \lambda & \lambda+2G & 0 & 0 & 0 \\ 0 & 0 & 0 & G & 0 & 0 \\ 0 & 0 & 0 & 0 & G & 0 \\ 0 & 0 & 0 & 0 & 0 & G \end{bmatrix} \begin{bmatrix} \varepsilon_{xx} \\ \varepsilon_{yy} \\ \varepsilon_{zz} \\ \gamma_{xy} \\ \gamma_{yz} \\ \gamma_{zx} \end{bmatrix} \tag{3-2}$$

in which

$$\lambda = \frac{E\nu}{(1+\nu)(1-2\nu)}$$

$$G = \frac{E}{2(1+\nu)}$$

In the Drucker-Prager model, the state of the soil is determined from the yield surface, defined from the first principle stress invariant (J_1), the second deviatoric stress invariant (J_2), the internal friction angle (ϕ) and the cohesion (c). If the value of the yield function is lower than zero, the soil is considered to be an elastic state and the stress is related to the strain by stress-strain relation matrix D, as was defined in **Equations 3-1** and **3-2**. If the value of the yield function is equal to zero, the soil begins to yield by the shear stress. The yield function in the Drucker-Prager model is defined as

$$f(\sigma) = \sqrt{J_2} + \alpha J_1 - \kappa \tag{3-3}$$

where

$$\alpha = \frac{2\sin\phi}{\sqrt{3}(3-\sin\phi)}$$

$$\kappa = \frac{6c\cos\phi}{\sqrt{3}(3-\sin\phi)}$$

The deformation of soil in the plastic state is calculated by the plastic potential function. To account for dilatancy, the non-associated flow rule is used to define the plastic strain increments

in relation to the yield surface. If $d\varepsilon_p$ denotes an increment in plastic strain, then the plastic flow rule can be stated as

$$d\varepsilon^p = \Lambda \frac{\partial Q}{\partial \sigma} \tag{3-4}$$

Plastic potential Q is established from the same relation as that for the yield surface, except that the dilatancy angle (ψ) is used instead of the frictional angle (ϕ). The plastic potential function can be expressed as

$$Q(\sigma) = \sqrt{J_2} + \alpha' J_1 - \kappa' \tag{3-5}$$

in which

$$\alpha' = \frac{2\sin\psi}{\sqrt{3}(3-\sin\psi)}$$

$$\kappa' = \frac{6c\cos\psi}{\sqrt{3}(3-\sin\psi)}$$

With an infinitesimal level of stress, the changes in strain are summed and then divisible into elastic and plastic parts. This begins with the equation

$$d\varepsilon = d\varepsilon^e + d\varepsilon^p \tag{3-6}$$

From the relation in **Equations 3-1**, **3-4**, and **3-6**, the relation between the strain increments and the stress increments can be written as

$$d\sigma = Dd\varepsilon - \Lambda D \frac{\partial Q}{\partial \sigma} \tag{3-7}$$

or

$$d\varepsilon = D^{-1} d\sigma + \Lambda \frac{\partial Q}{\partial \sigma} \tag{3-8}$$

Multiplying **Equation 3-8** by $\left(\frac{\partial F}{\partial \sigma}\right)^T D$ and noting that $D \cdot D^{-1}$ is an identity matrix, we have

$$\left(\frac{\partial F}{\partial \sigma}\right)^T D d\varepsilon = \left(\frac{\partial F}{\partial \sigma}\right)^T d\sigma + \Lambda \left(\frac{\partial F}{\partial \sigma}\right)^T D \frac{\partial Q}{\partial \sigma} \tag{3-9}$$

After the material yields, the new yield surface must be such that stress $\sigma + d\sigma$ lies on it. In order words, the value of yield function $F(\sigma + d\sigma)$ always equals zero if the material continues to yield. Which the material is yielding, it can be written as

$$dF(\sigma) = 0 \tag{3-10}$$

which, on expansion by the chain rule, leads to

$$\left(\frac{\partial F}{\partial \sigma}\right)^T d\sigma = 0 \tag{3-11}$$

Substituting **Equation 3-11** into **Equation 3-9** leads to Λ being calculated as

$$\Lambda = \frac{1}{A} \cdot \left(\frac{\partial F}{\partial \sigma}\right)^T D d\varepsilon \tag{3-12}$$

where

$$A = \left(\frac{\partial F}{\partial \sigma}\right)^T D \frac{\partial Q}{\partial \sigma}$$

Substituting Λ from **Equation 3-12** into **Equation 3-7** gives the required relationship between $d\sigma$ and $d\varepsilon$, namely,

$$d\sigma = D_{ep} d\varepsilon \tag{3-13}$$

where elasto-plastic stress-strain relation D_{ep} can be written as

$$D_{ep} = D - \frac{1}{A} D \frac{\partial Q}{\partial \sigma} \left(\frac{\partial F}{\partial \sigma}\right)^T D$$

Note that this matrix is symmetric only for the associated flow rule. If the plasticity is non-associated, non-symmetric D_{ep} leads to non-symmetric stiffness equations in the finite element analysis.

In this research, the soil material is assumed to be constant in volume after yielding. Thus the dilatancy angle is equal to zero ($\psi = 0$).

Due to the fact that soil can resist a small amount of tension, the plasticity state is also defined by tension stress values. From a definition for the equivalent stress,

$$\overline{\sigma} = \sqrt{\sigma_1^2 + \sigma_2^2 + \sigma_3^2} \tag{3-14}$$

where σ_1, σ_1, and σ_1 are the first, second and third principle stress levels, respectively. Each of these is only incorporated if it is a tension stress. This model now reads

$$\overline{\sigma} - \sigma_y = 0 \tag{3-15}$$

The plastic surface limits the allowed tension stress, and in this simulation model the limited tension stress of the soil is equal to zero ($\sigma_y = 0$).

The tension limiting plasticity model, combined with the Drucker-Prager model, is used to simulate the soil properties. The combination of the plasticity surfaces of both models defines the total plasticity surface of the soil material.

Elongation elements

In order to allow the shield machine to move forward, elongation elements are applied at the interface of the shield and the segment. They are defined to be the elastic transverse isotropic materials that are stiff in the radial direction, but weak in the longitudinal direction. Thus, the elongation elements are lengthened according to shield movements while the back lining elements are fixed in space.

Interface elements

Interface elements are employed to model the interface soil between the skin plate and the surrounding soil. The interface elements can slide in the longitudinal direction without causing

much distortion to the surrounding elements. They are modeled by Mohr-Coulomb's elasto-plastic yield criterion with transverse isotropic properties. The properties of the interface elements are defined as follows:

$$E, \phi_{\text{interface-radius}} = E, \phi_{\text{soil}}$$

$$E_{\text{interface-longitudinal}} = E_{\text{soil}} / n$$

$$\phi_{\text{interface-longitudinal}} = \phi_{\text{soil}} / n \tag{3-16}$$

where n is defined as the reduction factor that is greater than one. The reduction factor (n) expresses the proportion of the properties of the interface and the excavated elements to the ordinary soil elements. It depends on the ground conditions, the shield type and the construction procedure. The reduction factor is used to determine the ground properties, i.e., the internal friction angle and the elastic modulus.

Failure of the interface elements takes place if the magnitude of shear stress (τ) at the failure plane is equal to the value given by the following relationship:

$$|\tau| = \sigma_n \tan\phi_0 + c_0 \tag{3-17}$$

in which $|\ |$ denotes the absolute value, σ_n is the normal stress on the failure plane, and ϕ_0 and c_0 are the material constants of the shield-soil interface material. In the case of sandy and gravelly grounds, the adhesion is set at zero ($c_0 = 0$). **Equation 3-16** can be written in the form of yield function (F) as

$$F = |\tau| + \sigma_n \tan\phi_0 \tag{3-18}$$

When the state of the material is elastic, transverse isotropic properties are applied. Stress-strain relation matrix D is defined as

$$D = \begin{bmatrix} E_s & 0 & 0 & 0 & 0 & 0 \\ 0 & E_s & 0 & 0 & 0 & 0 \\ 0 & 0 & E_n & 0 & 0 & 0 \\ 0 & 0 & 0 & G_n & 0 & 0 \\ 0 & 0 & 0 & 0 & G_s & 0 \\ 0 & 0 & 0 & 0 & 0 & G_s \end{bmatrix} \tag{3-19}$$

where E_n and G_n are Young's modulus and the shear stiffness for the normal direction, and E_s and G_s are the corresponding parameters in the shear direction.

When material is sheared to the yield surface and the non-associated flow rule is adopted, the rates for plastic normal strain $d\varepsilon_n^p$ and shear strain γ^p are given by

$$\begin{bmatrix} d\varepsilon_n^p \\ d\gamma^p \end{bmatrix} = \Lambda \begin{bmatrix} \tan\phi_0 \\ 1 \end{bmatrix} \tag{3-20}$$

which implies

$$\frac{d\varepsilon_n^p}{d\gamma^p} = \tan\phi_0 \tag{3-21}$$

Each increment in shear displacement along the plane is accompanied by an increment in the normal displacement. The dilation will go unbounded under the yield. To avoid this unfavorable behavior, the flow rule for the shield-soil interface should be non-associated. Following **Equation 3-4**, a plastic potential function can be written by introducing dilatancy angle ψ. Thus,

$$Q = |\tau| + \sigma_n \tan\psi \tag{3-22}$$

In this study, no dilatation is assumed for the shield-soil interface ($\psi = 0$).

After the yield and the plastic potential function are established, a general formulation as in **Equation 3-13** is used for the elasto-plastic stress-strain relation matrix.

Excavated elements

Shield tunneling causes an extreme disturbance to the soil adjacent to the cutting head during excavation. Excavated elements are defined in front of the cutting head as the proposed method of representing the area of the ground being disturbed by the excavation (Akagi and Komiya, 1993). The thickness of the excavated elements is assumed to be equal to the length of the cutter bits or the rippers. Since these elements are greatly disturbed, they are assumed to be weak elastic materials. Slurry pressure or retaining pressure is applied uniformly as nodal forces at the soil elements go beyond the excavated elements. The Young's modulus of each element is defined as follows:

$$E_{excavated} = E_{soil} / n \tag{3-23}$$

where n is the reduction factor that has the same value as that mentioned in **Equation 3.16**.

Shield machine and tunnel lining

The shield machine is modeled by a group of rigid boundary nodes, which are forced to move along the designated route. The weight of the machine is uniformly distributed to the adjacent soil in the lower half of the shield nodes. After each small step of advancement, forces acting on all shield nodes are calculated. The driving force used to control the machine at each step is determined by summing up all the nodal forces. Multiplying the nodal forces by the distance from the center point of the machine and by totaling all the nodal moments, the required driving moments can be determined.

The tunnel lining is defined as a stiff elastic material or a nearly rigid body. There is no clearance between the ground and the lining. Back-filling pressure behind the shield tail is not considered.

3.2.3 Remeshing techniques

To simulate the excavation procedure, the finite element mesh is rearranged after a shield movement of about half the thickness of the excavated element. **Figure 3.3** depicts the sequential behavior of the finite element model as the excavation is carried out by the cutting head and the tunneling machine advances. The shaded elements in front of the shield machine in **Figure 3.3** represent the excavated elements. The initial step of the calculation starts at reference time t in **Figure 3.3**(a). Then, shield boundary nodes are forced to move forward in a curve in a curve

according to the designated route. The excavated elements and the other elements within the elements adjacent to the shield machine deform simultaneously along time period *dt*, as shown in **Figure 3.3**(b). After computing the displacements and the stress levels in the deformed mesh, shown in **Figure 3.3**(b), the finite element mesh is rearranged as shown in **Figure 3.3**(c), with the correct stress fields. This forces the equilibrium to bring the geometric shape and size back to what they were originally, as shown in **Figure 3.3**(a). The nodal coordinates of the rearranged mesh change according to the distance of the shield movement. The stress levels for all nodes in the deformed mesh are stored and used for calculating the nodal stress levels of the newly rearranged mesh. Then, the calculation is started again using the new nodal coordinates and stress values as the initial stage of the next moving step. The remesh procedure is done repeatedly by the methods described above along the entire excavation route.

After the original mesh is deformed, following a step of shield movement, the mesh is rearranged to take the same shape and size it originally had. The nodal coordinates of the rearranged mesh are calculated from the moving distance and the direction of the shield machine. Then, the deformed elements, which include the rearranged nodal points are identified. For the sake of simplicity, the method for calculating the stress values in the rearranged mesh is described as an example of a quadrilateral element, as shown in **Figure 3.4**. The figure shows deformed element α enclosed by nodes n_1, n_2, n_3, and n_4 and remeshed element αR enclosed by nodes nR_1, nR_2, nR_3, and nR_4. In this figure, deformed element α includes nodal point nR_1 of remeshed element αR. The updated stress levels of node nR_1 can be calculated by the following procedure.

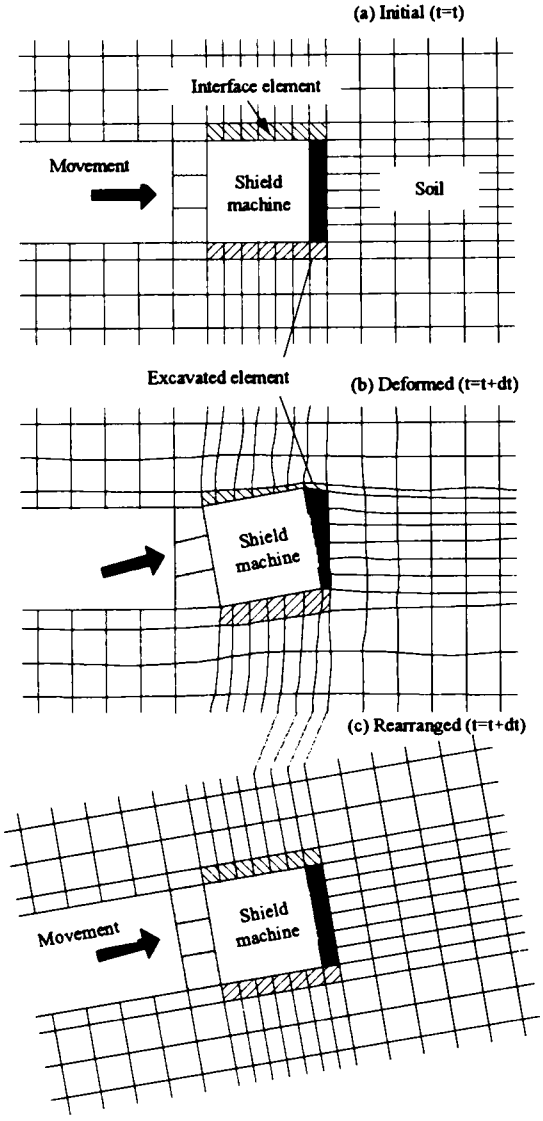

Figure 3.3 Advancement of the shield machine simulated by the remesh method

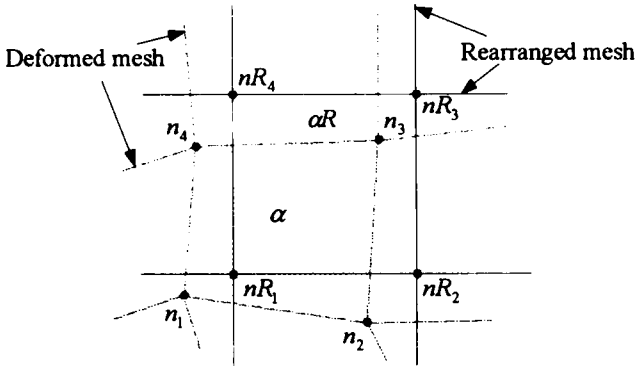

Figure 3.4 Rearrangment of the finite element

Calculating the stress levels of the deformed mesh

The broken lines in **Figure 3.4** represent the deformed geometry of the finite element mesh due to the shield movement, as shown in **Figure 3.3**(b), at reference time t = t + dt. The initial stress of four-node isotropic finite element α is assumed to be $\{\sigma^{\alpha}\}_t$ at reference time t = t. Stress change $\{\delta\sigma^{\alpha}\}$ of element α, associated with nodal point displacement vector $\{\delta u^{\alpha}\}$ due to the shield movement during time step dt, as shown in **Figures 3.3**(a) and **3.3**(b), is given by the following equation:

$$\{\delta\sigma^{\alpha}\} = \int_V [D_{ep}][B^{\alpha}]\{\delta u^{\alpha}\}dV \tag{3-24}$$

where $[D_{ep}]$ is the elasto-plastic stress-strain relation matrix and $[B^{\alpha}]$ is the strain-displacement matrix. Accordingly, stress $\{\sigma^{\alpha}\}_{t+dt}$ at time t = t + dt is described as follows:

$$\{\sigma^{\alpha}\}_{t+dt} = \{\sigma^{\alpha}\}_t + \{\delta\sigma^{\alpha}\} \tag{3-25}$$

Updating the stress levels of the rearranged mesh

The deformed finite element mesh, which is indicated by the broken lines, is then rearranged into a regular rectangular finite element mesh represented by the solid lines in **Figure 3.4**. The coordinates of all the nodes in the remeshed elements are determined according to the moving direction and the distance of the machine. Considering remeshed element αR and node nR_1, that lie within deformed element α, stress values at node nR_1 can be interpolated from all the nodal stress levels of element α obtained from **Equation 3-26**, as follows:

$$\{\sigma_{nR_1}^{\alpha R}\} = \sum_{j=1}^{m} [N_j^{\alpha}]\{\sigma_j^{\alpha}\}|_{t+dt} \tag{3-26}$$

where $[N_j^{\alpha}]$ are the element interpolation function values at particular points in element α, $\{\sigma_j^{\alpha}\}$ is the nodal stress vector of element α, and m is the number of nodal points constituting a single finite element α.

Computing the residual forces

After updating the stress levels, the overall equilibrium of the rearranged mesh system is checked. The errors produced from **Equation 3-27** are defined as the residual forces. The residual forces of the rearranged nodal forces, $\{\delta\Psi_R\}$, are computed using the following equation:

$$\{\delta\Psi_R\} = \int_V [B]^T \{\sigma\}_{t+dt}\, dV - \int_V [B]^T \{\sigma\}_t\, dV \qquad (3\text{-}27)$$

where $\int_V [B]^T \{\sigma\}_t\, dV$ means the external forces of the overall system at time t.

In this simulation, the residual forces computed at the rearranged nodal points are simply added to the loading forces of the subsequent incremental step.

3.3 Simulations of the shield excavation processes

In this section, the experimental problems of a shield excavation in a sandy ground are analyzed to investigate the effects of the excavation depth, the soil properties, and the radius of the moving curve on the required driving forces, driving moments, and acting load on the machine. The geometry and the boundary conditions of the analysis mesh are shown in **Figure 3.5**. The simulated shield machine is a cylindrical slurry type that is 6 m in external diameter and 6 m in length. The material parameters for each soil type are shown in **Table 3.2** (Das, 1994).

Table 3.2 Parameters of rounded uniform sand (Das, 1994)

Material parameters of the soil	Loose sand	Medium sand	Dense sand
Unit weight (γ_d) (kN/m^3)	14.0	16.0	18.0
Young's modulus (E) ($\times 10^6\ kN/m^2$)	15.5	31.0	62.0
Poisson's ratio (ν)	0.20	0.33	0.40
Frictional angle (ϕ)	28	33	37
Cohesion strength (c)	0	0	0
Coefficient of lateral earth pressure ($K_0 = 1 - \sin\phi$)	0.53	0.46	0.40

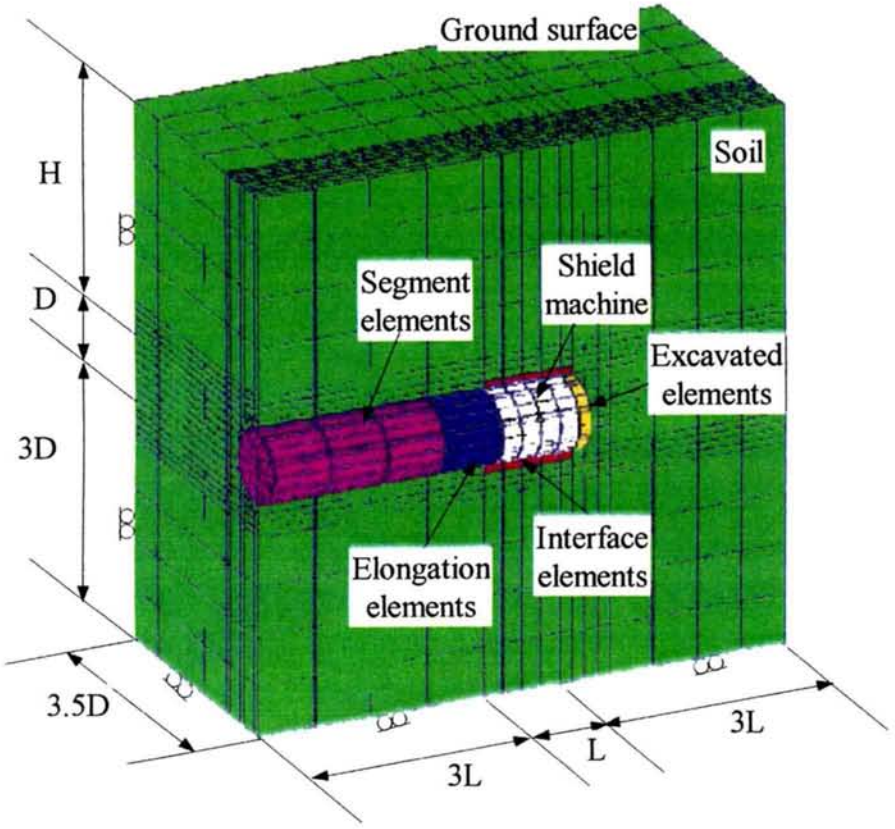

Figure 3.5 Geometry of the analysis mesh

3.3.1 Parametric studies

Firstly, the effects of the reduction factor, the n value in **Equations 3-16** and **3-23**, on the resistance forces acting on the machine during the excavation, are investigated. In order to determine these effects, an analysis of the shield tunneling at a depth of 18 m (3D, D is the external diameter of the shield machine) in medium dense sand is carried out. The analysis is conducted by moving the shield machine in a straight direction for 4 m. In this study, the reduction factor (n) is used to determine the properties of the excavated and the interface elements, and is defined as a function of the surrounding soil parameters, as shown in **Equations 3.16** and **3.23**. Using reduction factor n as 10, 30, 50, 60, 80, and 100, the resistance forces acting on the shield machine are calculated. Plots for the resisting forces acting on the shield machine during the shield movement are shown in **Figures 3.6**(a)~(c). A plot of the resistance forces versus reduction factor n is shown in **Figure 3.7**. The resistance forces acting on the machine are divided into two parts, namely, skin friction and earth pressure at the tunnel face. From **Figures 3.6** and **3.7**, it is obvious that the resistance forces decrease when the

factor increases. A greater value for the reduction factor means a lower level of stiffness for the excavated and the interface elements. A decrease in stiffness for both elements leads to a decrease in the resistance forces acting on the shield machine. The skin friction decreases considerably when the reduction factor increases. However, the earth pressure at the shield face does not show any significant changes when the reduction factor changes.

Based on the general method (JSCE, 1995), the resistance forces acting on the shield machine during the excavation in a cohesionless ground can be calculated by the following equations:

$$F_{skin} = \mu \cdot (\pi D_0 L P_m + W)$$
$$F_{face} = P_f \frac{\pi}{4} D_0^2 \qquad (3\text{-}28)$$

where F_{skin} is the frictional force between the skin plate and the ground, F_{face} is the earth pressure at the tunnel face, μ is the coefficient of friction between the skin plate (steel) and the natural ground, D_0 is the outer diameter of the shield machine, L is the length of the shield machine, W is the self-weight of the shield machine, P_m is the average earth pressure load on the shield skin, and P_f is the slurry pressure for a slurry shield or the earth pressure at the shield face for an earth pressure balance shield.

Using the **Equation 3-28**, the resistance forces of the above problem are F_{skin} = 19,000 kN, F_{face} = 4,370 kN, and $F_{total} = F_{skin} + F_{face}$ = 23,370 kN. These agree well with the numerical results in which the reduction factor equals 50, as shown in **Figure 3.7**, F_{skin} = 19,550 kN, F_{face} = 4,740 kN, and F_{total} = 2,4290 kN. Therefore, it can be concluded that the appropriate value for the reduction factor in this case is 50; this value is further used for analyzing in the next sections. It should be noted that in the next sections, the properties of the interface and the excavated elements are defined as follows:

$$E_{excavated} = E_{interface\text{-}longitudinal} = E_{ground} / 50$$
$$\phi_{interface\text{-}longitudinal} = \phi_{ground} / 50 \qquad (3\text{-}29)$$

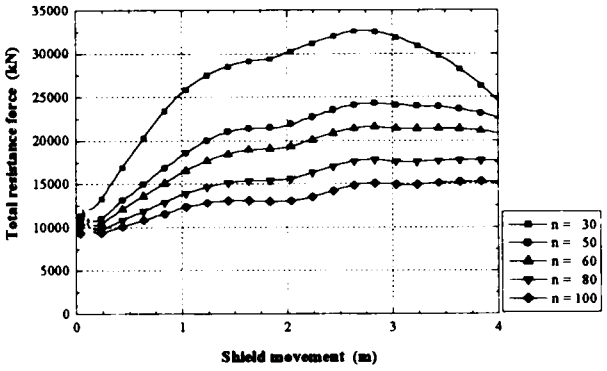

(a) Total resistance force

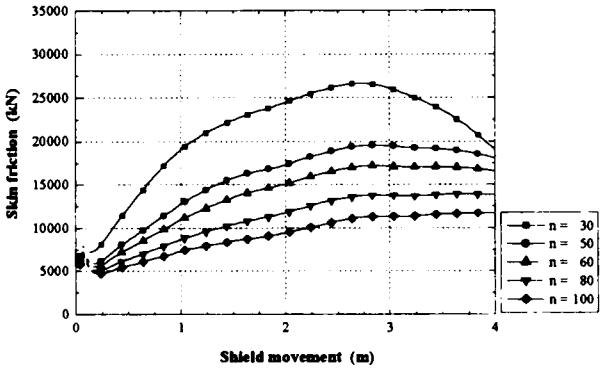

(b) Frictional force at skin plate

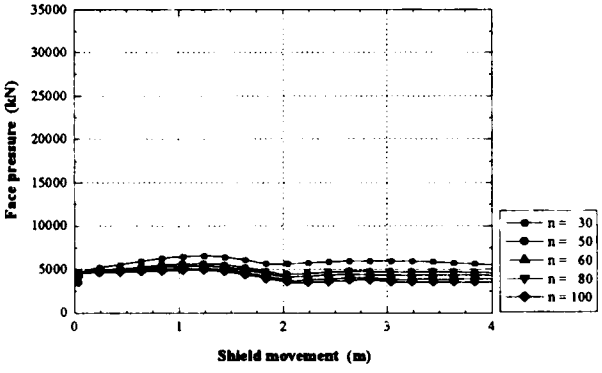

(c) Earth pressure at shield face

Figure 3.6 Resistance forces of the parametric studies

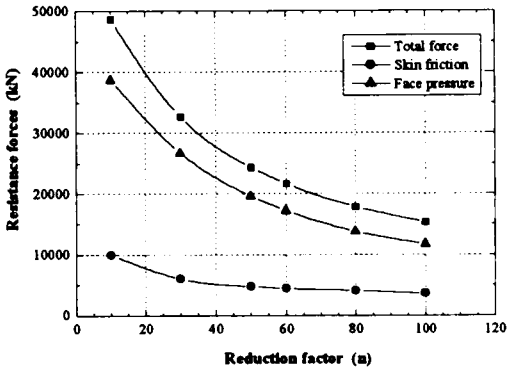

Figure 3.7 Variation in resistanc forces against the reduction factor

3.3.2 Analysis of the shield excavation along a straight alignment

In this section, simulations of the shield excavation along a straight alignment are carried out. By varying the soil type and the excavation depth, the skin friction and the average earth pressure at the shield face are calculated. The soil types used in this analysis are loose, medium, and dense rounded uniform sand, without underground water. The material parameters of each soil type are shown in **Table 3.2**. The excavation depths, measured from the ground surface to the top crown of the machine, are 1D, 3D, and 5D where D is the outer diameter of the shield machine, as shown in **Figure 3.8**(a)~(c). The external diameter and the length of the shield machine are both 6 m.

(a) Excavation depeth = 1D

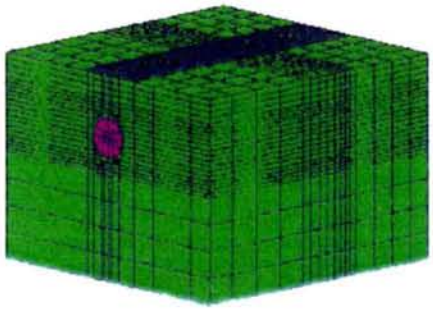

(b) Excavation depeth = 3D

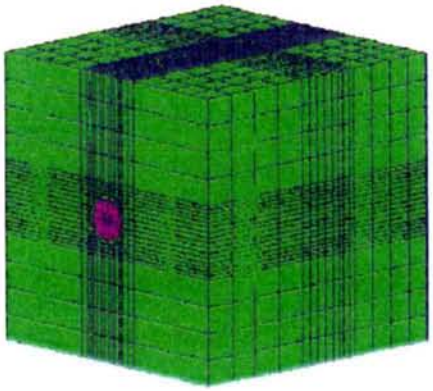

(c) Excavation depeth = 5D

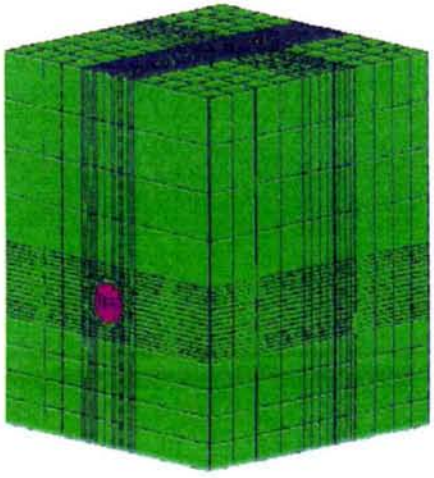

Figure 3.8 Finite element meshes in the analyses

The calculation results for the resistance forces acting on the shield machine along the moving distance for all cases are shown in **Figures 3.9** through **3.11**. The results show that the frictional force along the skin plate is the main proportion of the total force acting on the shield compared with the earth pressure at the cutting face. The earth pressure is nearly constant along the excavation, while the skin friction and the total force gradually increase and tend to be constant by the end of the calculation. These results may be caused by the effects of the interface elements surrounding the skin plate. When the shield moves, the stress levels in the interface elements increase such that cause the nodal resistance forces increase. The resistance forces increase until all the elements yield and then they become constant. The resistance forces trend to converge after excavating for a distance that varies depending on each excavation condition. In some cases, the resistance forces do not increase continuously, which may be caused by the excessive distortion in some elements while the shield is moving. This can be corrected by remeshing the analysis mesh more frequently.

Comparisons of the total resisting force along the excavation distance at each excavation depth and for each soil type are shown in **Figures 3.12** and **3.13**, respectively. They clearly demonstrate that a deeper excavation depth and a stiffer soil type result in the need for larger jack forces in order for the shield to advance. Plots for the acting forces against the excavation depth are shown in **Figure 3.14**. Plots for the skin friction and the earth pressure as the percentage of the total resistance forces against the excavation depth are summarized in **Figure 3.15**. This figure shows that the skin friction acting on the skin plate makes up the main portion of the total resistance force, an average of 79%, while the earth pressure acting on the shield face makes up only about 21%. The gap in this proportion narrows when the excavation depth is deeper or the surrounding soil is looser.

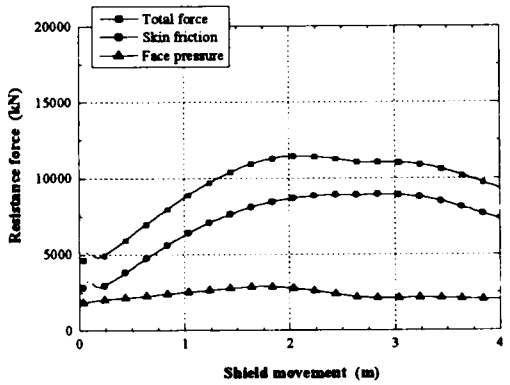

(a) Loose sand

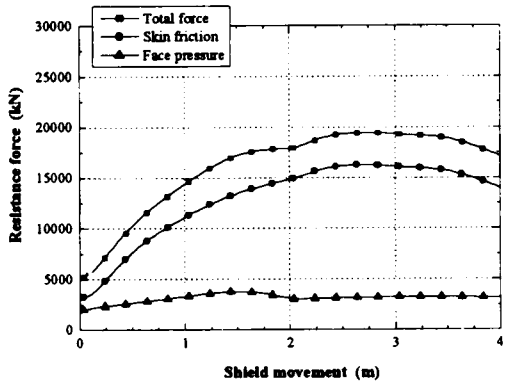

(c) Medium dense sand

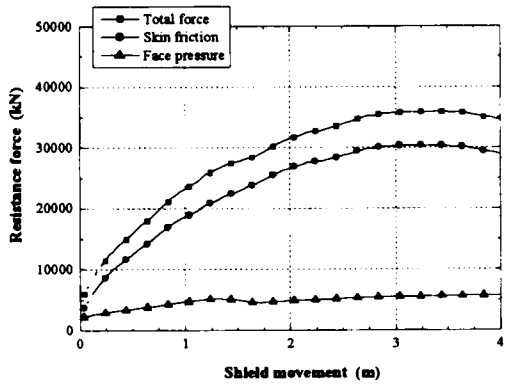

(d) Dense sand

Figure 3.9 Resistance forces for excavation depth = 1D

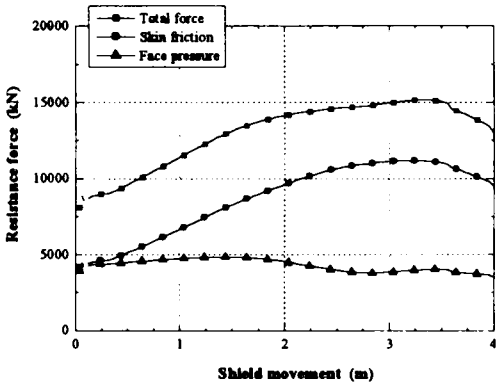

(a) Loose sand

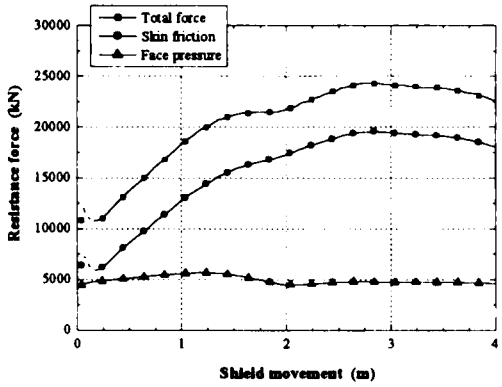

(b) Medium dense sand

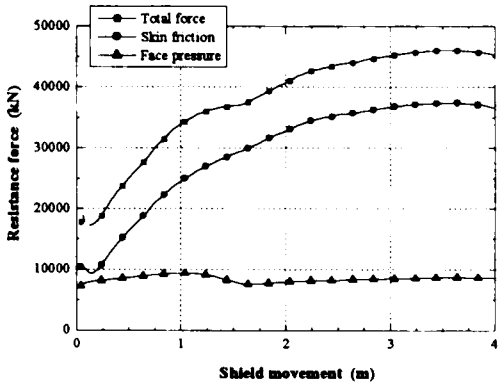

(c) Dense sand

Figure 3.10 Resistance forces for excavation depth = 3D

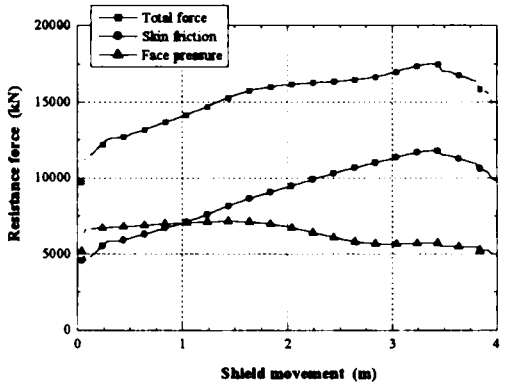

(a) Loose sand

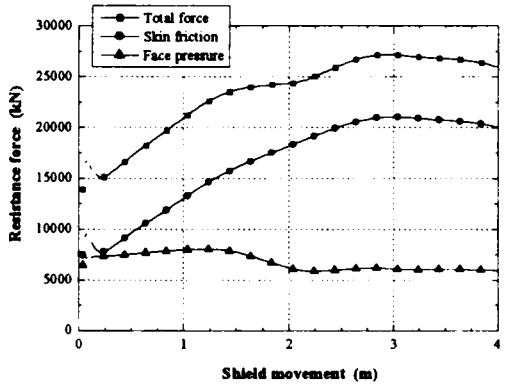

(b) Medium dense sand

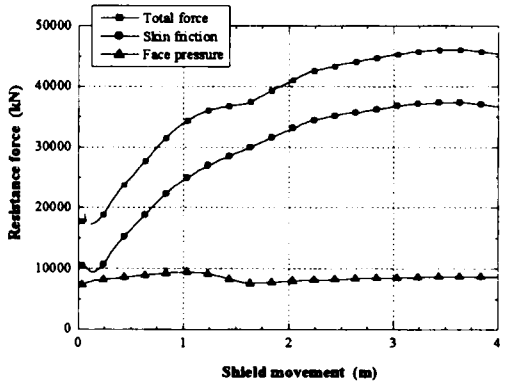

(c) Dense sand

Figure 3.11 Resistance forces for excavation depth = 5D

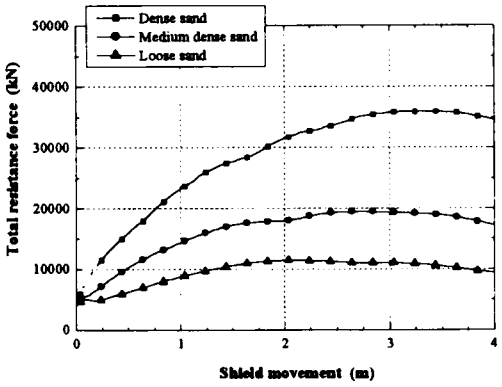

(a) Excavation depth = 1D

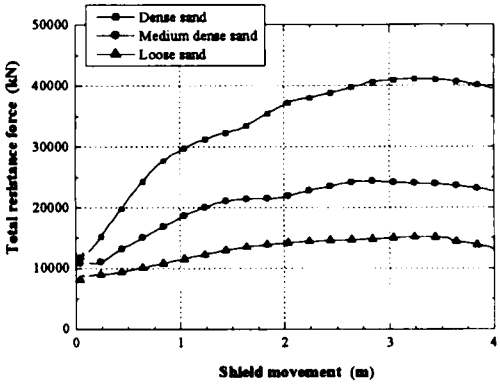

(b) Excavation depth = 3D

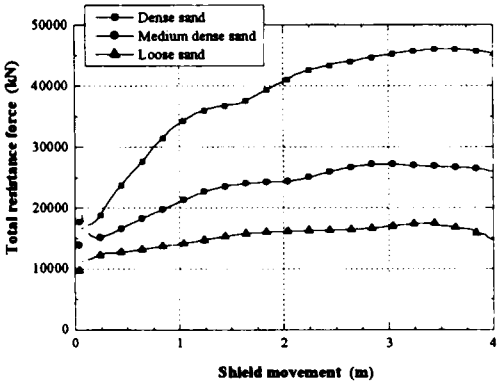

(c) Excavation depth = 5D

Figure 3.12 Total resistance forces for each excavation depth

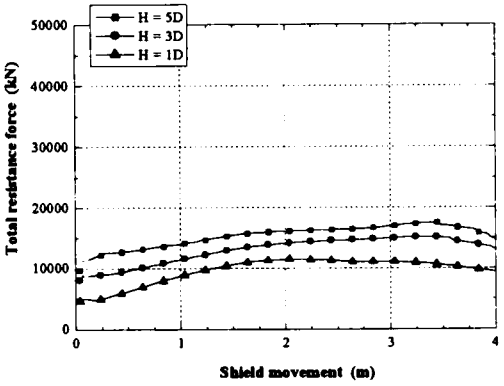

(a) Loose sand

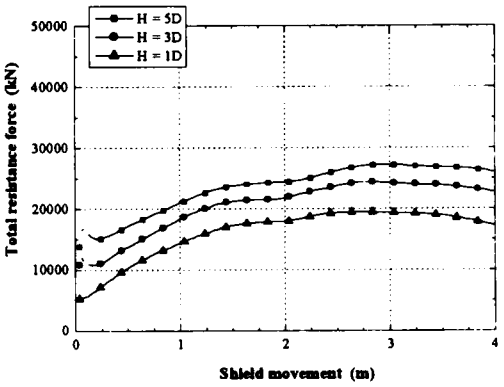

(b) Medium dense sand

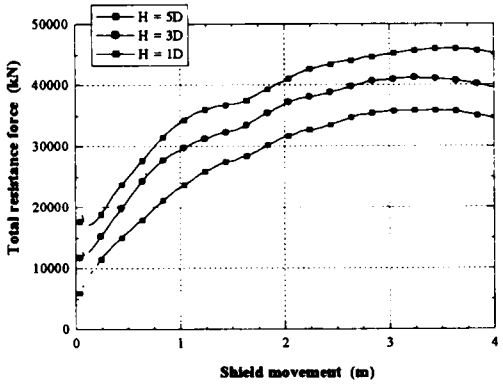

(c) Dense sand

Figure 3.13 Total resistance forces for each soil type

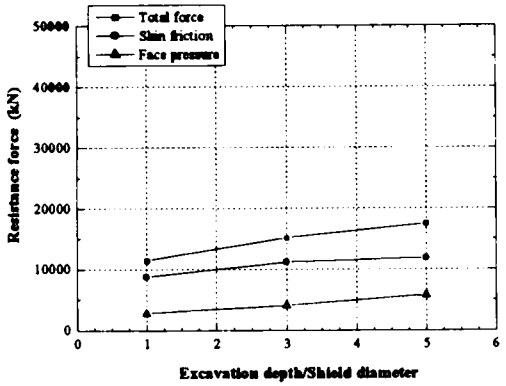

(a) Loose sand

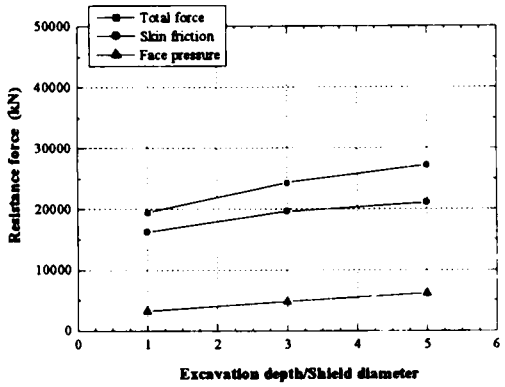

(b) Medium dense sand

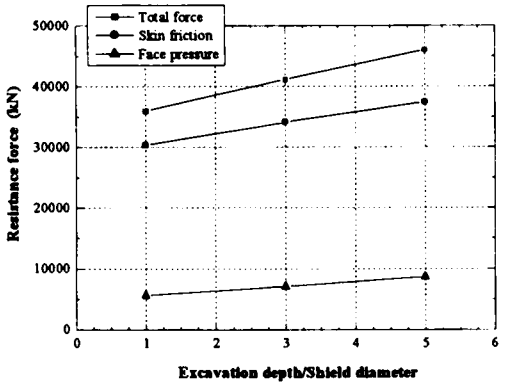

(c) Dense sand

Figure 3.14 Variation of resistances forces against excavation depth

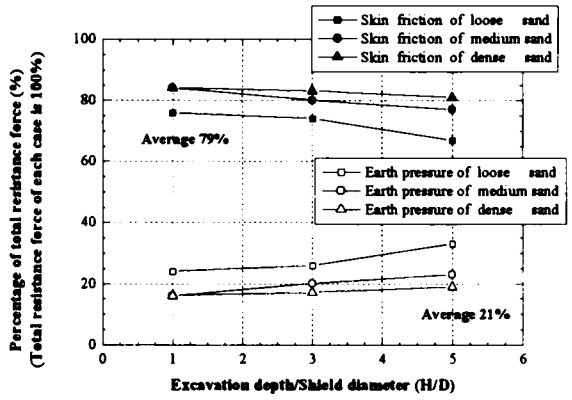

Figure 3.15 Percentage of resistance forces against the excavation depth

3.3.3 Analysis of the shield excavation along a curved alignment

The required driving forces and driving moments during the movement along a curved alignment are investigated by moving the shield machine forward at curves of 50R, 100R and 200R. Note that curves at 50R, 100R, and 200R mean the radii of the moving curves are equal to 50 m, 100 m, and 200 m, respectively. After each step of shield movement, the forces acting on each shield node are summed to obtain the total acting force and moment. They imply the driving force and the driving moment which should be generated at each construction step in order to control the machine to move precisely along the designated curved alignment.

Thrust moments for driving the shield machine

Plots for the required thrust moments while excavating at 4 m curves for each cases are shown in **Figure 3.16** through **3.18**. Some extremely high results occur with the starting movement (about 0.1~0.2 m). However, the values decrease sharply and then increase gradually to become constant by the end of the calculation. This occurrence shows that when a shield is changing from a static stable to a moving state, the acting forces are extremely high. For the above reason, precise calculation results can only be obtained through a long distance analysis. The results show that at a sharper curved movement or a smaller radius, larger driving moments are required. Next, the thrust moments for moving a shield along a 50R curve at each excavation depth and for each soil type are summarized in **Figures 3.19** and **3.20**. They demonstrate that the driving

moment depends considerably on the soil type. In dense sand, a more driving moment is required than in loose sand along the same moving route. On the contrary, there is little change in the driving moment when the excavation depth is varied, especially at the first step of movement.

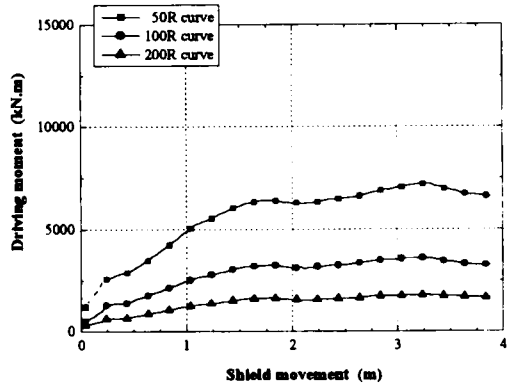

(a) Loose sand

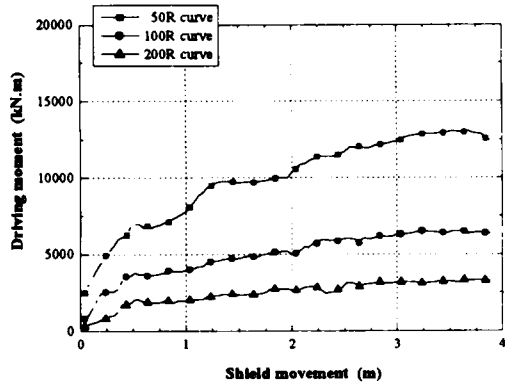

(b) Medium dense sand

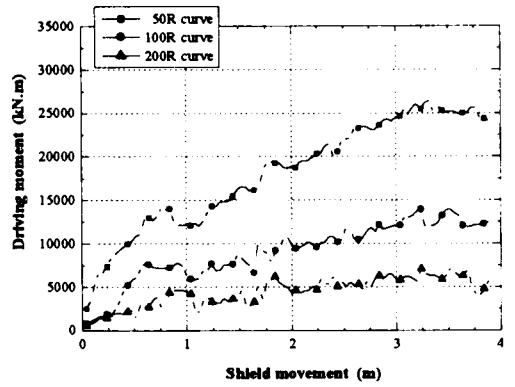

(c) Dense sand

Figure 3.16 Driving moments for excavation depth = 1D

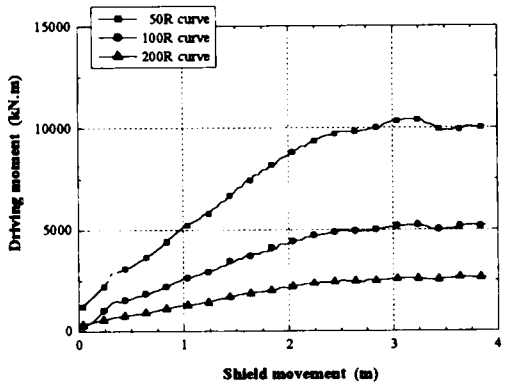

(a) Loose sand

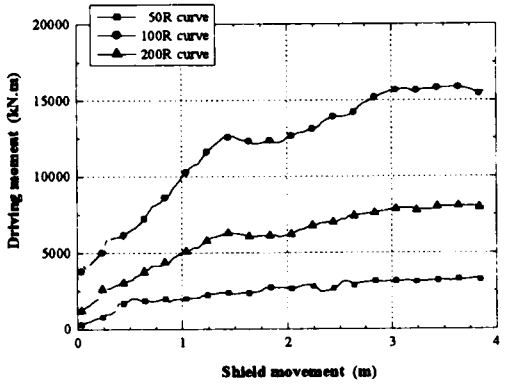

(b) Medium dense sand

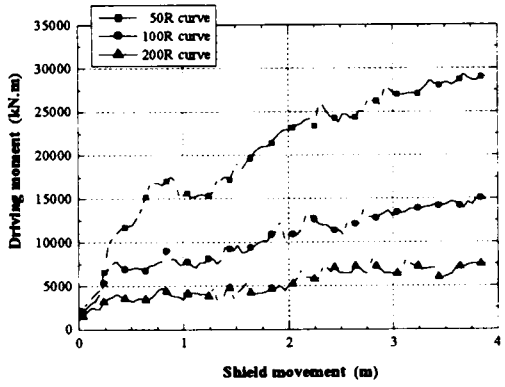

(c) Dense sand

Figure 3.17 Driving moments for excavation depth = 3D

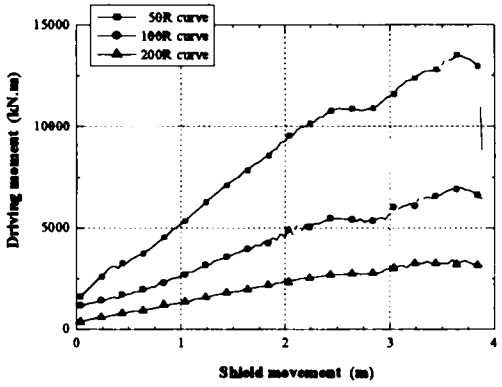

(a) Loose sand

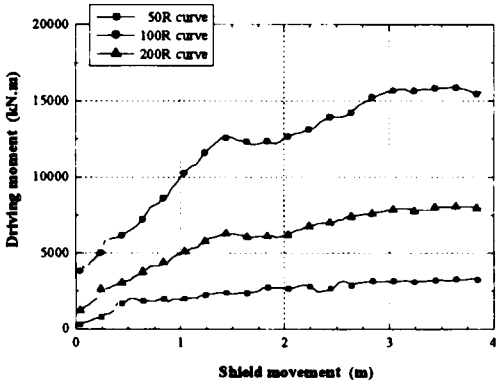

(b) Medium dense sand

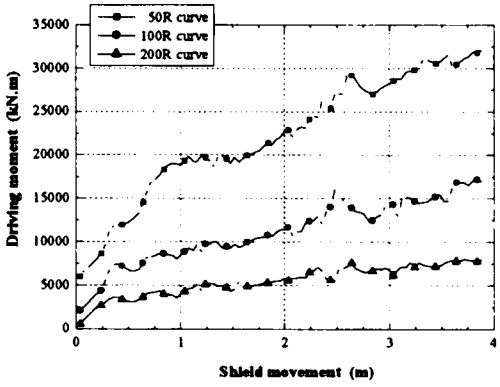

(c) Dense sand

Figure 3.18 Driving moments for excavation depth = 5D

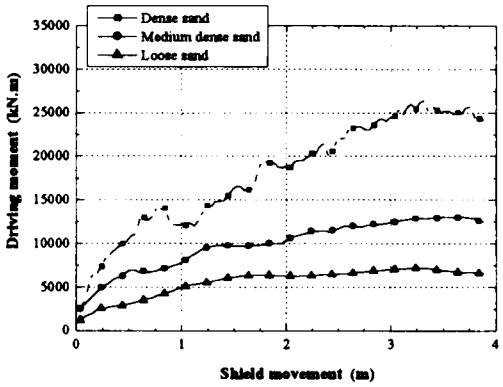

(a) Excavation depth = 1D

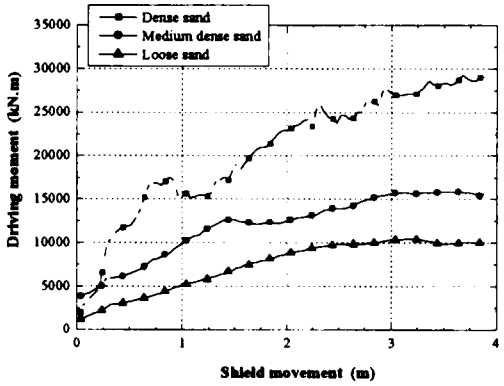

(b) Excavation depth = 3D

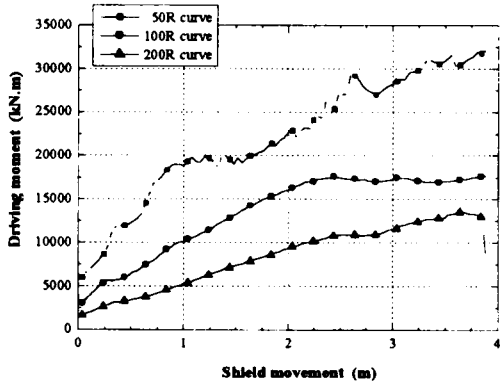

(c) Excavation depth = 5D

Figure 3.19 Driving moments for each excavation depth at 50R curve

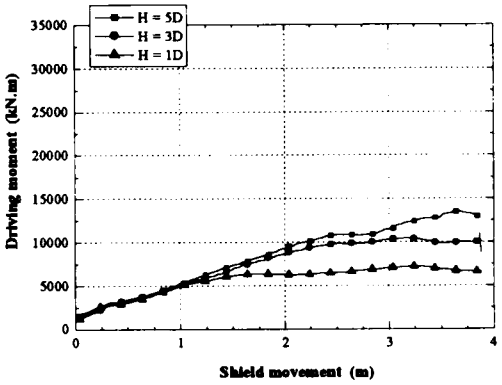

(a) Loose sand

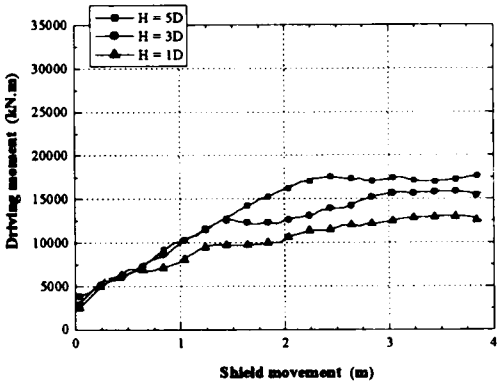

(b) Medium dense sand

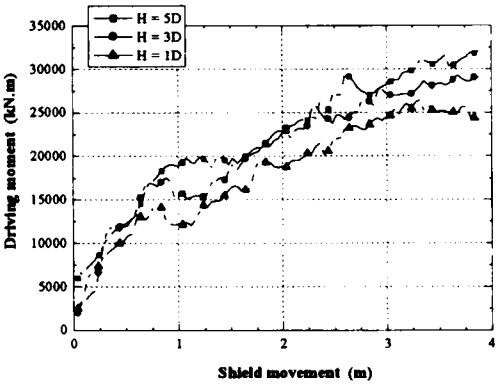

(c) Dense sand

Figure 3.20 Driving moments for each soil type at 50R curve

Earth pressure acting on the shield machine during excavation

The stress acting on the skin plate of a shield machine excavating in medium dense sand at the depth of 3D is discussed. The lateral stress levels occurring at the shield plate in a transverse direction along the excavation distance are calculated. The results of 50R, 100R and 200R curves are plotted in **Figures 3.21** through **3.23**. The plots for the stress levels of the skin plate after moving forward 4 m are shown in **Figure 3.24**. The results show that when the point moves into the soil, the lateral stress increases according to the moving distance. On the other hand, when the point moves off the soil, and thus, it is detached from the soil, the acting stress decreases to zero. At the front and the rear cross sections of the shield, the maximum pressure acting on the skin plate occurs. The results also show that with a more sharply curved alignment, the machine acts due to the greater earth pressure. The stress distribution at the face of the shield machine for all moving cases are plotted in **Figure 3.25**. They show that the maximum lateral pressure acting on the shield machine, when it moves forward at curves of 50R, 100R, and 200R, are about 1.78, 1.60, and 1.44 times the initial stress, respectively.

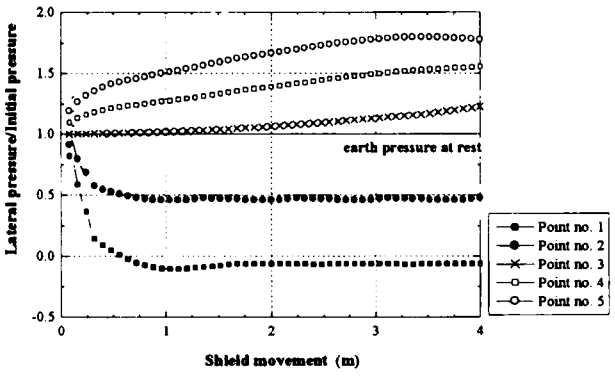

(a) Outside-curve points

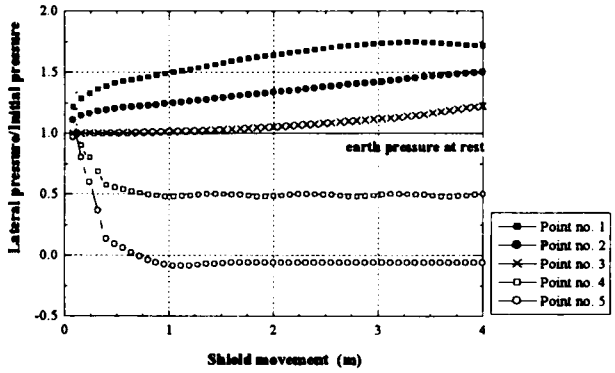

(b) Inside-curve points

Figure 3.21 Lateral pressure acting on the skin plate at 50R curve (medium dense sand, depth = 3D)

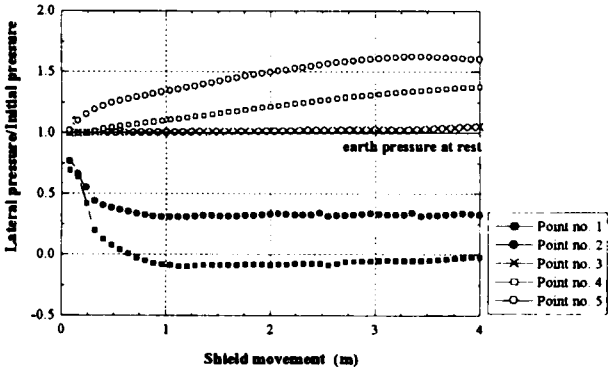

(a) Outside-curve points

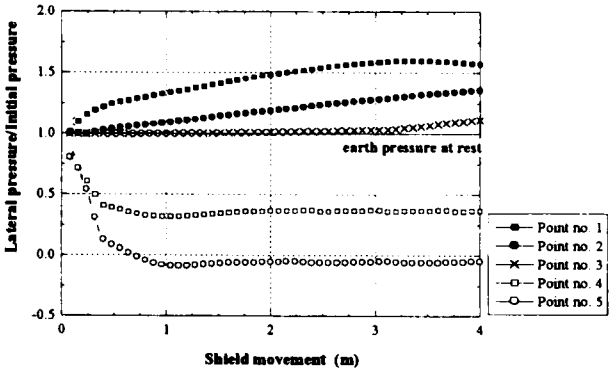

(b) Inside-curve points

Figure 3.22 Lateral pressure acting on the skin plate at 100R curve (medium dense sand, depth = 3D)

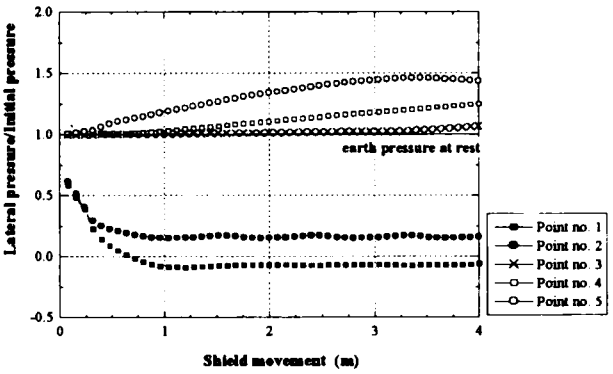

(a) Outside-curve points

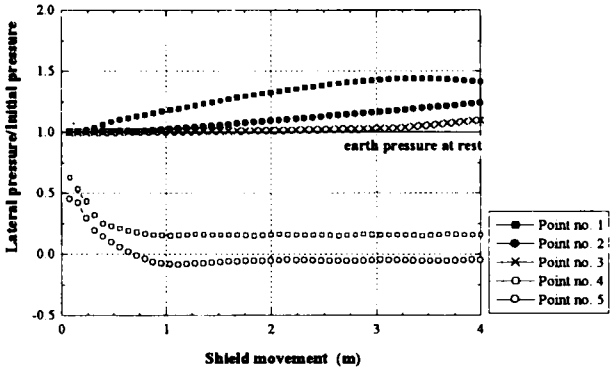

(b) Inside-curve points

Figure 3.23 Lateral pressure acting on the skin plate at 200R curve (medium dense sand, depth = 3D)

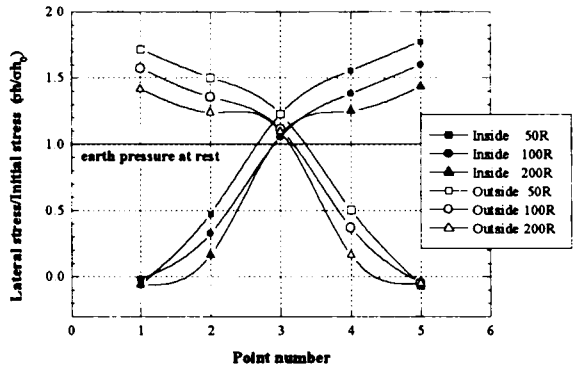

Figure 3.24 Lateral pressure acting on the skin plate (medium dense sand, depth = 3D)

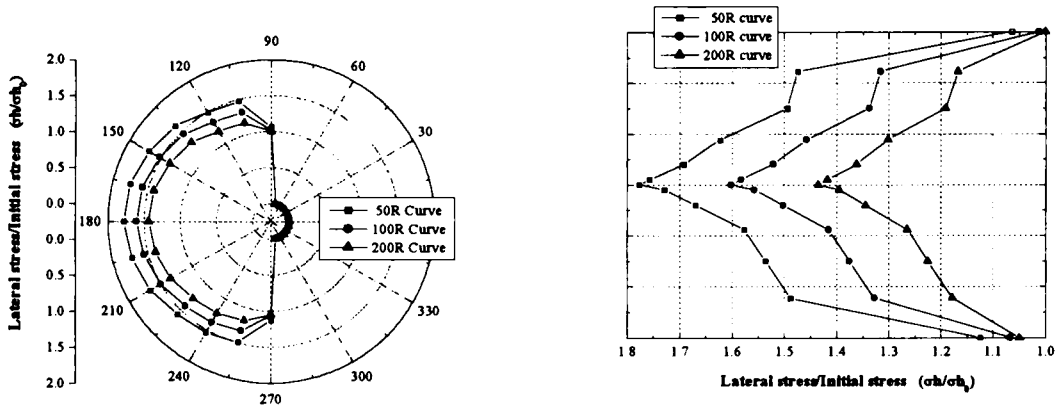

Figure 3.25 Lateral pressure acting on the face of a shield machine

The results show that during an excavation along a curved alignment, the shield machine acts due to the additional earth pressure depending on the curved radii. It can be thought that, when the machine moves along a curve, the parts which press against the ground act due to the passive pressure, while the parts which are detached from the ground act due to the active pressure. Predictions of the additional pressure are necessary for the design processes of shield machines. In addition, the thickness of the skin plate must be designed to support the additional forces which occur as the machine moves along a curved alignment.

3.3.4 Analysis of the shield excavating effects on underground structures

In this section, the capability of this analysis method to investigate the effects of shield movement on nearby underground structures is introduced. Since shield tunneling is widely used in urban areas, it is usually thought that the shield machine has to pass through areas where underground structures already exist. As shown in **Figure 3.26**, when a machine excavates close to a pile group foundation, the surrounding ground becomes stiffer and causes additional lateral force to the pile group. If the shield machine moves too close, failure of the nearby structures may occur. The effects of both shield movement and the distance between the shield and the nearby structures are investigated using the procedure shown in **Figure 3.27**. The spaces between the modeled wall and the shield machine used in this analysis are 0.5D, 1.0D and 1.5D. The geometry of the finite element mesh applied in this analysis is shown in **Figure 3.28**.

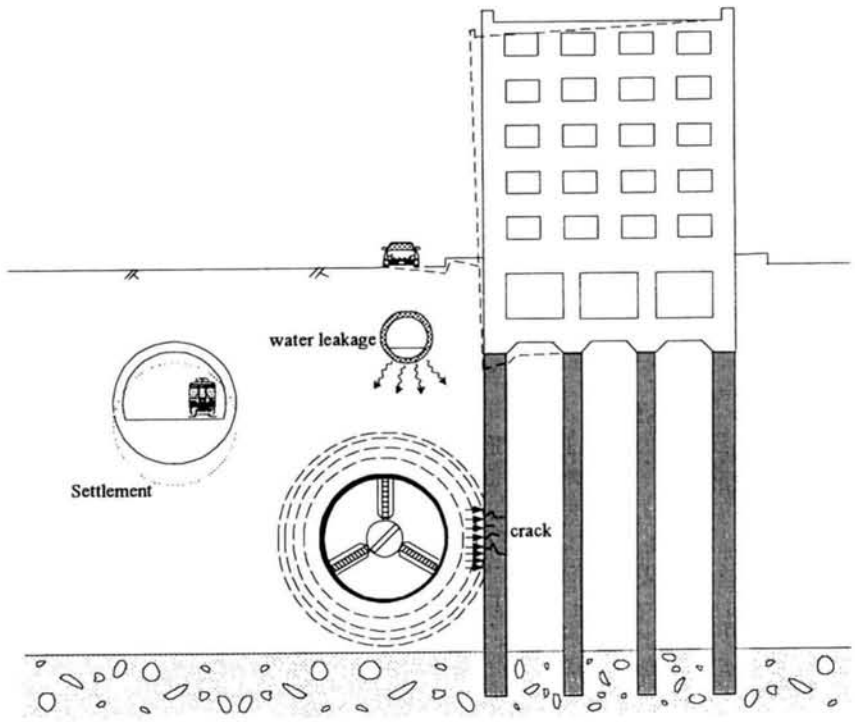

Figure 3.26 Image of the effects of shield excavation on surrounding structures

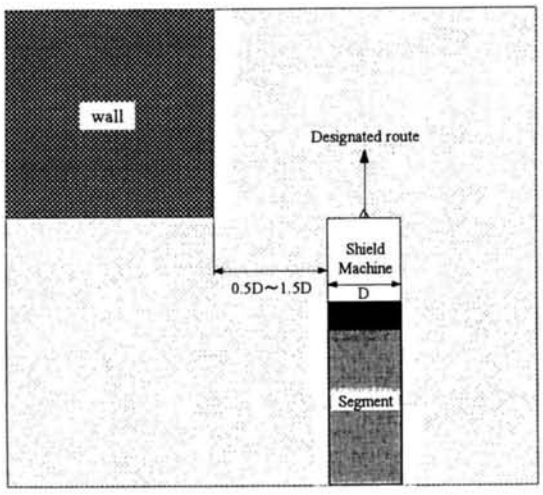

Figure 3.27 Analysis model of the effects of shield excavation on underground station

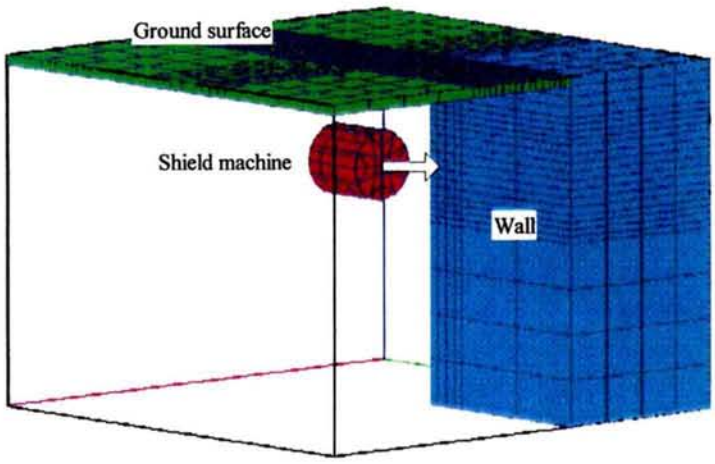

Figure 3.28 Geometry of finite element mesh for analyzing the effects of shield excavation on underground station

The stress distributions of every point on the wall face at the level of the center shield are shown in **Figures 3.29** and **3.30**. They show that there are few changes between a shield-wall gap of 1.0D and one of 1.5D. When the distance is reduced to 0.5D, however, the significantly large excess stress occurs. Thus, to prevent too large of an occurrence of stress, the distance between the shield and the structure should be kept at larger than 0.5D. While the shield machine moves forward, it causes the soil between the shield and the wall to become stiffer. The soil at the points on the shield face are stiffer than others, and that causes the stress at the points far away from the edge of the wall to be larger than these near the edge. **Figure 3.31** shows the stress distribution along the vertical line at the edge and at half the moving distance. It can be seen that the maximum forces act at the center of the shield level and the gradually decrease to both sides of the top and the bottom levels.

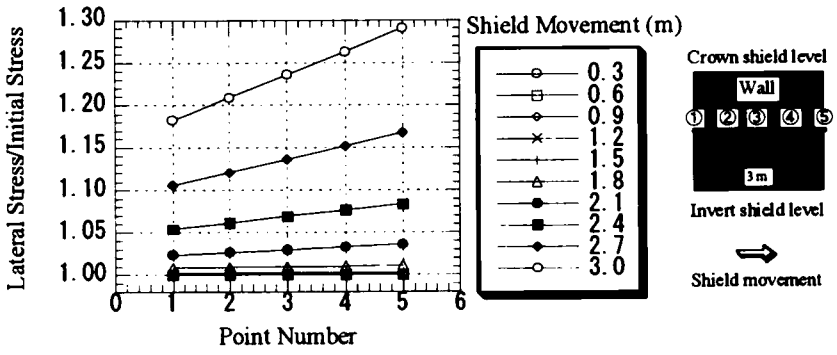

(a) Distance between shield and wall = 0.5D

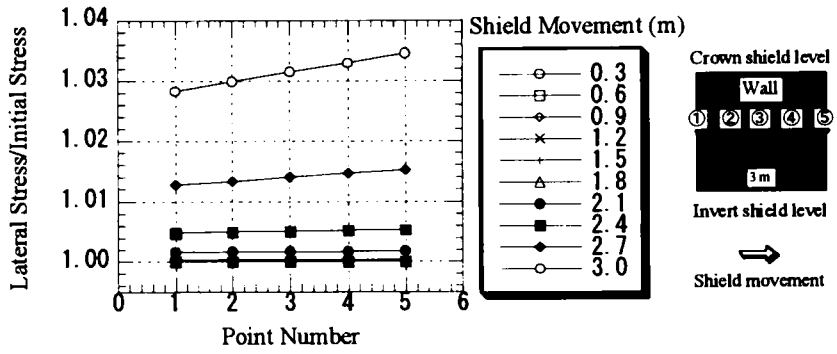

(b) Distance between shield and wall = 1.0D

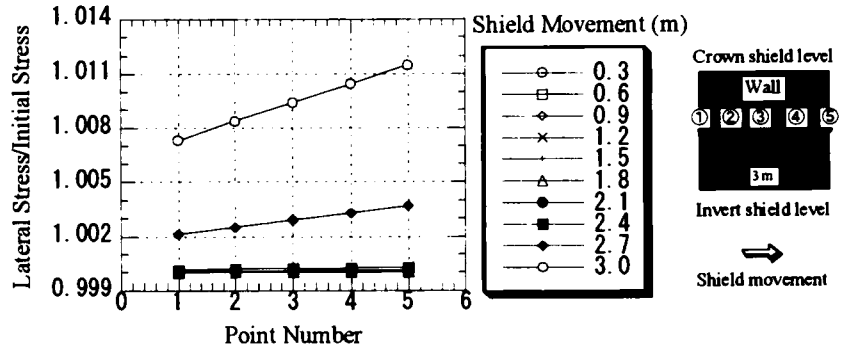

(c) Distance between shield and wall = 1.5D

Figure 3.29 Lateral stress of wall face at the level of center shield

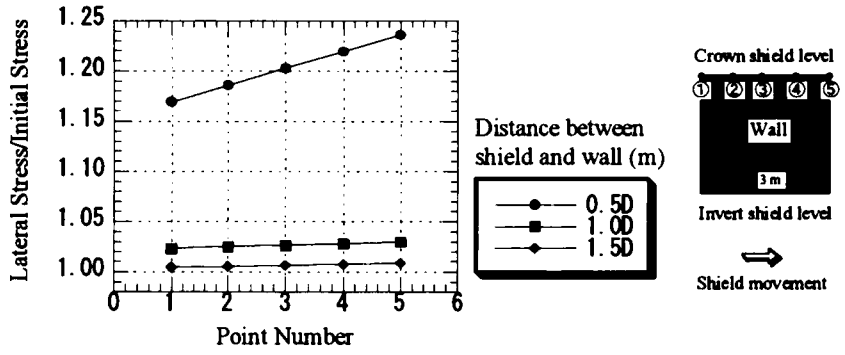

(a) At the level of the crown of a shield machine

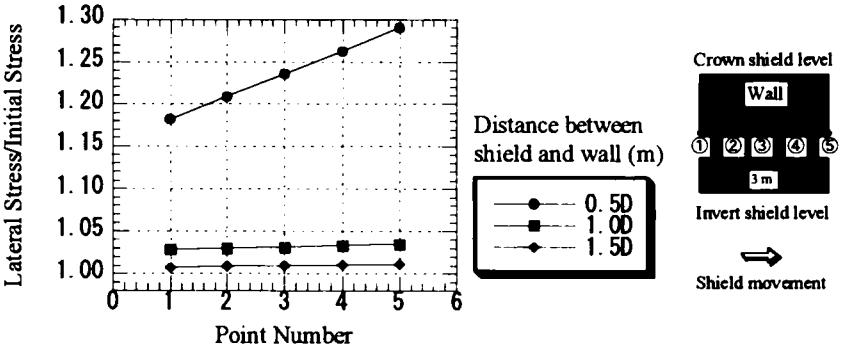

(b) At the level of the center of a shield machine

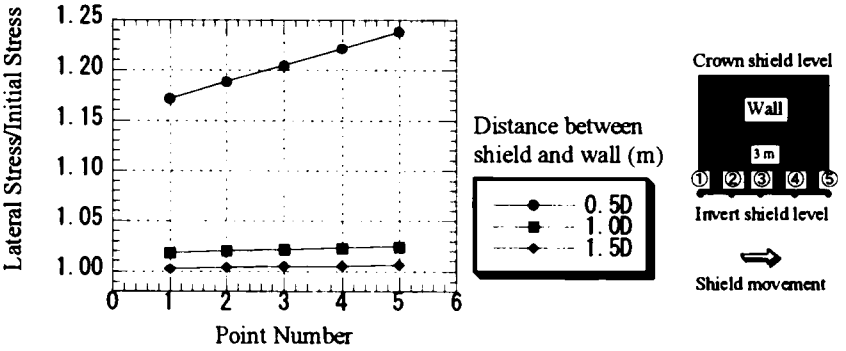

(c) At the level of the invert of a shield machine

Figure 3.30 Lateral stress of wall face at each level

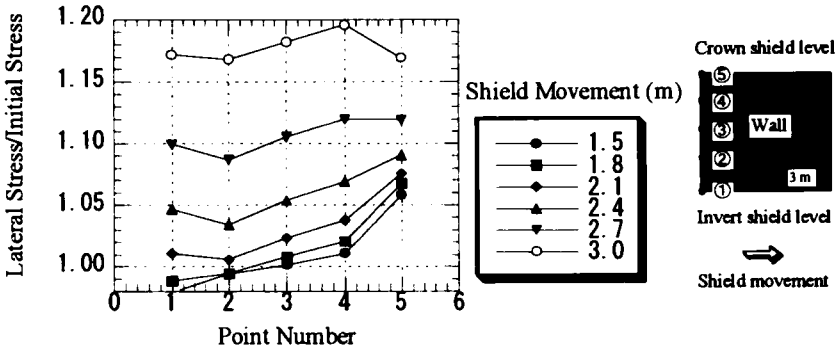

(a) At the edge of the wall

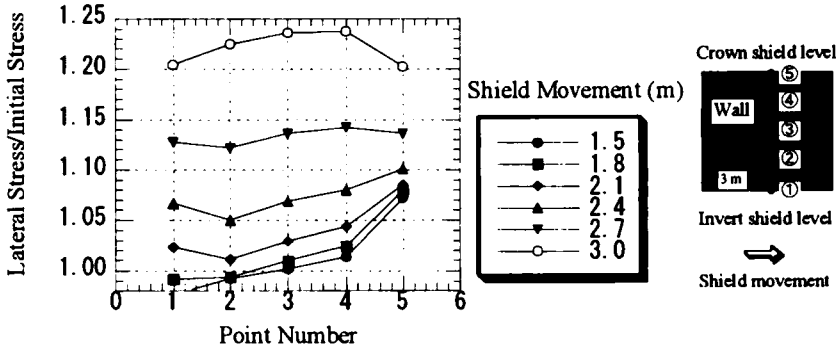

(b) At the half length of the shield movement distance

Figure 3.31 Lateral stress of wall face at the distance between shield and wall = 0.5D

3.4 Driving control of shield machines

In this chapter, the methods for applying the developed finite element program to the driving control of shield machines are introduced. The proposed methods are applied to an analysis of shield tunneling work in Kyoto City. Finally, comparisons between the calculated results and the measured data are demonstrated and discussed.

3.4.1 Application of the analysis techniques to the driving control of shield machines

The term "automatic driving control method" refers to a method that can determine the required driving forces and driving moments for moving a shield machine along a designated route in real time during construction. According to the simulation method described above, a flowchart of the calculation procedure for calculating the thrust forces and moments is shown in **Figure 3.32**.

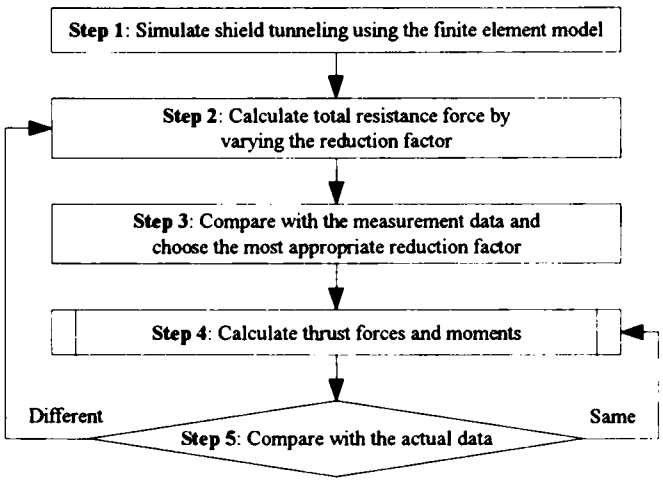

Figure 3.32 Flowchart of the driving control method for shield machines

Simulate the shield tunneling using a three-dimensional finite element model with the following remesh procedure.

① Calculate the total resistance force in the first step of excavation by varying the reduction factor of the interface and the excavated elements.

② Compare the calculated total resistance force with the measured total jack force. Then, choose a reduction factor that gives the results according to the measurement data from the excavation sites.

③ Use the chosen parameters as the input parameters for the finite element program to calculate the required driving forces and driving moments of the shield machine at the next step of excavation along the designated route.

④ Compare the calculated results with the measured data after each step of shield machine movement. Then, check the value of the reduction factor to see whether or not it must be changed. If the reduction factors must be changed, repeat Step ②. If the results still coincide with the measurement data, continue Step ④.

For cases in which the shield machine passes through different ground types, the finite element mesh and the properties of the ground elements must be changed. For any particular ground material, the input material parameters should be changed according to the values obtained from the soil tests. Then, the back-analysis procedure must be carried out again from Step ① to determine the reduction factor of the new soil stratum. However, the process of re-estimating the value of the reduction factor can be eliminated by correlating it with the type of ground and the type of machine. Such correlations can be determined by collecting the data from various construction projects. The correlations between the reduction factor and the type of soil and the reduction factor and the shield machine are scheduled for investigation in a future study.

3.4.2 Application of the analysis techniques to a the shield tunneling project

To verify the reliability of this simulation model, a tunneling project excavated by a slurry shield in a gravel ground is simulated. The details of the shield machine, the excavation conditions, and the ground properties of the project are shown in **Table 3.3**. **Figure 3.33** presents an outline of the excavation site and soil strata. The analysis mesh is shown in **Figure 3.34**. The variation in total resistance force against the reduction factor (n) is shown in **Figure 3.35**. The average jack force from the measured data at the first 4 m of the straight excavation is 7,140 kN. Compared with the calculated values, the result obtained using a reduction value of 80, is the closest at 8,600 kN. This result is used again to analyze the required driving forces and driving moments along a distance of 8 m at a curved alignment of 200R.

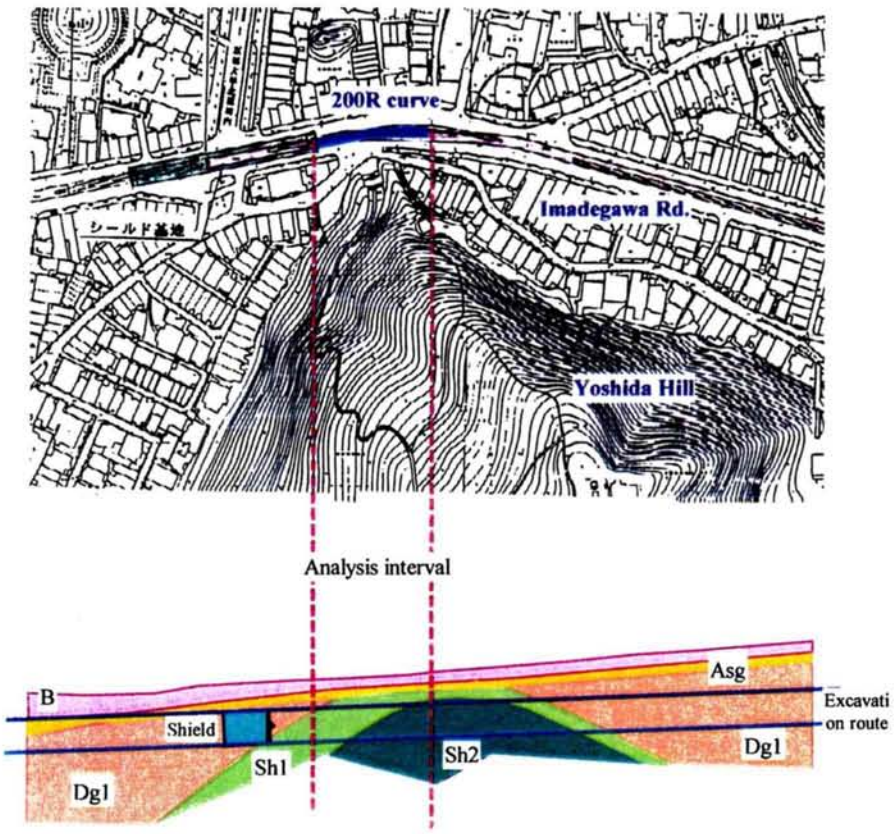

Figure 3.33 Excavation route and soil profile of the shield tunneling project in Kyoto City

Table 3.3 Ground properties used for simulating the shield tunneling project

Soil type	Top soil (B)	Gravel + sand (Asg)	Gravel (Dg1)	Shale rock (Sh1)	Shale rock (Sh2)
SPT N value	9	36	55	45	over 60
Specific gravity γ_d (kN/m^3)	19	19	20	20	20
Young modulus E (kN/m^2)	3,600	14,400	33,780	100,000	100,000
Poisson ratio ν	0.30	0.35	0.40	0.45	0.45
Cohesion strength c (tf/m^2)	0	0	0	0	0
Frictional angle ϕ	27	38	44	15	15

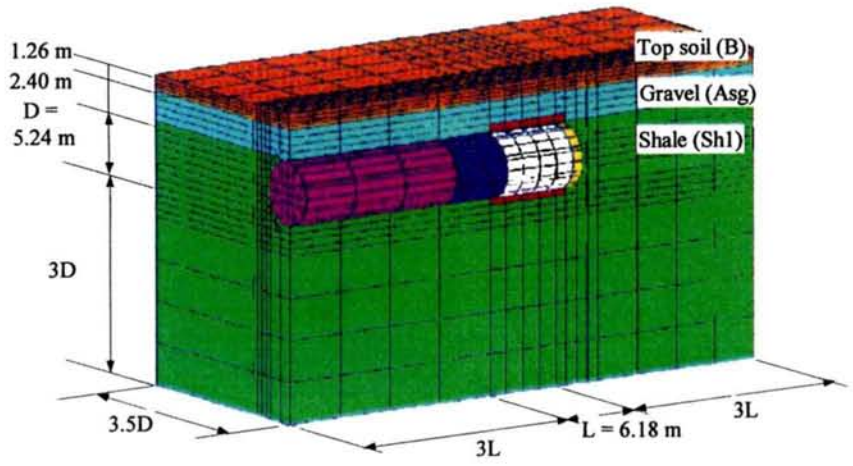

Figure 3.34 Simulation mesh of the tunneling project

The distribution of resistance forces, namely, skin friction, earth pressure, and total resistance, are plotted in **Figure 3.36**. The total resistance force, skin friction, and earth pressure are about 8,710 kN, 7,480 kN (86%) and 1,230 kN (14%), respectively. A comparison of the thrust forces from the calculation and those from the measurements are shown in **Figure 3.37**. The average measurement jack force is 8,040 kN and the data scatter is about 40~70% from the average value. The calculated data is greater than the average value of the measured data by about 670 kN or 8.3%. A comparison of the thrust moments is also shown in **Figure 3.38**. The calculated results increase and become constant at 1,180 kN.m after moving about 6 m. The field data increase in the same way until 7 m, and then they decrease sharply to 5,750 kN.m. These comparisons express the fact that the calculated results are slightly higher than the field data for both driving forces and driving moments. This may be caused by the effects of the overcutter and/or the articulated jacks that were employed in the real excavation. Applying an overcutter and articulated jacks reduces the amount of acting forces on the machine. Thus, the actually required driving forces and driving moments tend to be lower than the calculated results which model the shield machine as a rigid cylinder.

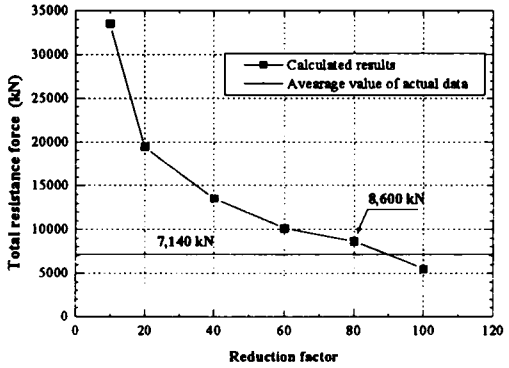

Figure 3.35 Estimation of the reduction factor in the tunneling simulation

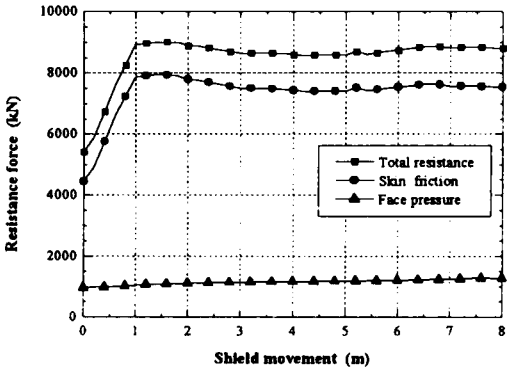

Figure 3.36 Calculated results of the resistance forces acting on the shield machine

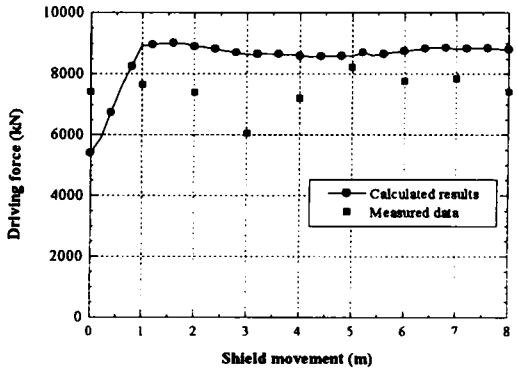

Figure 3.37 Comparisons between calculated results and measured data of the driving force

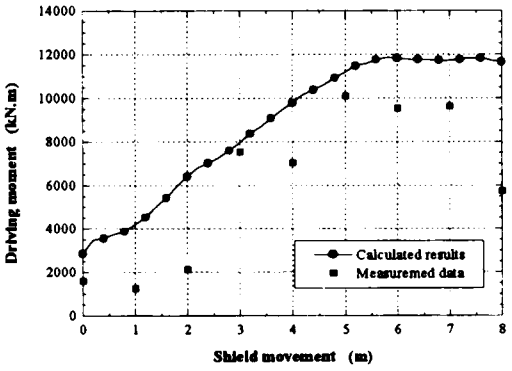

Figure 3.38 Comparison between calculated results and measured data of the horizontal driving moments

3.5 Conclusion

From this study, it has been shown that the excavation processes of a shield machine can be simulated by remeshing the finite element mesh at every small advancement of the shield. The specially defined elements, namely, the excavated, the interface, and the elongation elements, can be used to model the shield-soil interaction behavior. The properties of the excavated and the interface elements can be simply assumed as the proportion of Young's modulus to the internal friction angle of the surrounding soil. The reduction factor is used to express this relation. A reduction factor can be evaluated by a back analysis from the measurement data in the first step of the excavation.

The thrust forces that should be generated to drive the machine can be calculated by totaling the acting forces on the shield nodes. The thrust moments which program the machine to move along the designated curve can be calculated by summing the products of the nodal forces and the distance from the central point of the machine. From the calculation results of the experimental problems, it is clarified that the skin friction is a large portion of the total resistance force compared with the earth pressure at the face. Larger driving forces and driving moments are required along curved alignments to control the machine to move along sharper curves. When considering the earth pressure acting on the skin plate of the shield machine, the pressure increases according to its moving distance into the soil.

This analysis program can also be applied to investigate the effects of shield excavating on nearby underground structures. The excessive earth pressure acting on underground structures can be controlled by limiting the distance between the machine and the structure.

The idea of an automatic driving control method for shield machines has been introduced by utilizing the proposed simulation model of the shield excavation processes. In addition to ground properties, the reduction factor should be evaluated carefully in order to obtain accurate results. The reduction factor is thought to correlate to the ground and the machine types. Continuous research will be conducted in order to realize the idea of automatic control systems for shield machines.

Comparisons between the calculated and the measured data show that the required driving forces and the driving moments calculated from the proposed method are slightly greater than those of the actual data from the excavation field. Therefore, it can be thought that simulations of the overcutter and the articulated jacks are necessary for obtaining more accurate results.

Chapter 4

EXPERIMENTAL STUDY ON FLAT-SHAPED SEGMENTAL LININGS IN THE SHIELD TUNNELING METHOD

4.1 Introduction

In this chapter, the mechanical behavior of nonuniform flat-shaped linings is investigated with two sets of experimental model tests. The first are the model loading tests under 1g and the second are the second is two-way loading tests.

4.2 Model loading tests

The mechanical behavior of nonuniform flat-shaped linings is investigated in this section. A small-scale device for loading the model linings under plane-strain conditions has been developed. Model tests on model linings under gravity loads are carried out. Three types of tunnel shapes, namely, circular, elliptical and horseshoe are addressed in this study. The effects of thickness patterns are investigated by testing the nonuniform-thickness lining for each type of elliptical and horseshoe-shaped tunnel.

The strain generated at each loading step is measured and the member forces, the axial forces, and the bending moments are calculated. The mechanical behavior and the stability of the tunnel linings are compared and evaluated with these three values, namely, strain, axial force, and bending moment.

In this chapter, two groups of tests on tunnel linings are reported. The first group of tests is done on the circular and the elliptical tunnels. The effects of the tunnel shape, the elliptic ratio, and the thickness pattern are demonstrated and discussed. The second group of tests is done on the horseshoe-shaped tunnels. As will be presented in this chapter, the efficiency of increasing the stability of the tunnel linings by varying the lining thickness is demonstrated and discussed.

4.2.1 Experimental apparatus, testing procedure, and model lining

The laboratory testing apparatus used in this study is shown in **Figure 4.1**. The soil chamber is made of steel, but a glass plate is installed in the front.

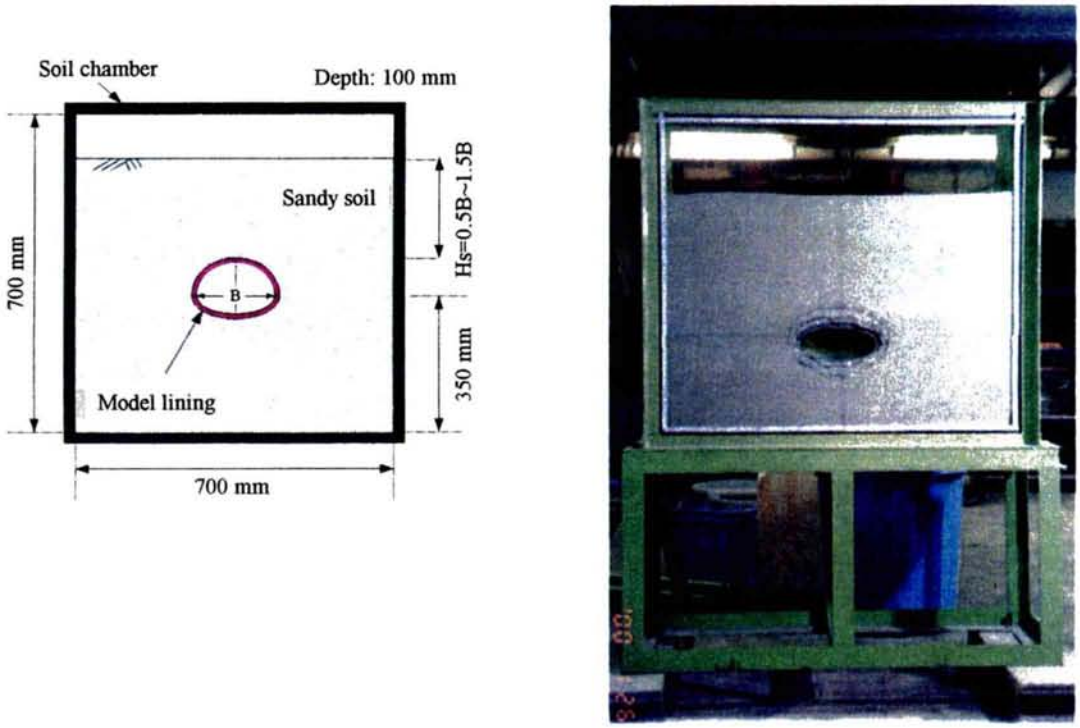

Figure 4.1 Laboratory testing apparatus for the model loading tests

Table 4.1 Properties of the sand and the model ground used in the model loading tests

Material name	No. 6 silica sand
Specific weight	2.63
Maximum void ratio	1.03
Minimum void ratio	0.64
D_{60}	310 μ m
D_{10}	120 μ m
Uniformity	2.58
Density	1,467 kg/m^3
Relative density	59.6%
Frictional angle	36°

Table 4.2 Properties of the Styrofoam and the model lining used in the model loading tests

Material name	Polystyrene foam
Density	30 kg/m^3
Compressive strength	0.273 MPa
Elastic modulus	15.240 MPa
Poisson's ratio	0.01

The model lining is set at the position shown in the **Figure 4.1**. After that, the soil chamber is filled up with dry silica sand. For these tests, No. 6 silica sand is used to produce the experimental ground material and the model lining is made from polystyrene foam (Styrofoam), whose trade name is Kanelite foam type FIII (Kaneka Corporation). The properties of the sand and the Styrofoam are shown in **Tables 4.1** and **4.2**, respectively.

The tests are carried out on four types of tunnel shape, namely, circular, elliptical (with elliptic ratio of 75% and 50%), and horseshoe. The size and the shape of the model linings are shown in **Figure 4.2** and **4.3**. As shown in the figures, the inner shape and the area of the tunnel lining for each tunnel type are the same. Only the outer shape is changed for investigating the effects of the thickness pattern. This is based on the concept that ordinarily the inner shape of a tunnel is determined by such architectural conditions as the number of road lanes, the lane width, the ventilation equipment, etc. The same inner shape means the same utilization capacity of the tunnel and the same tunnel area means the same cost for constructing the tunnel lining.

To measure the member forces generated on the tunnel lining after loading, a total of sixteen strain gauges are symmetrically attached at the following positions: 0° (crown), 45°, 90° (spring line), 135°, and 180° (invert), on both outer and inner sides of the lining surface, as shown in **Figure 4.4**.

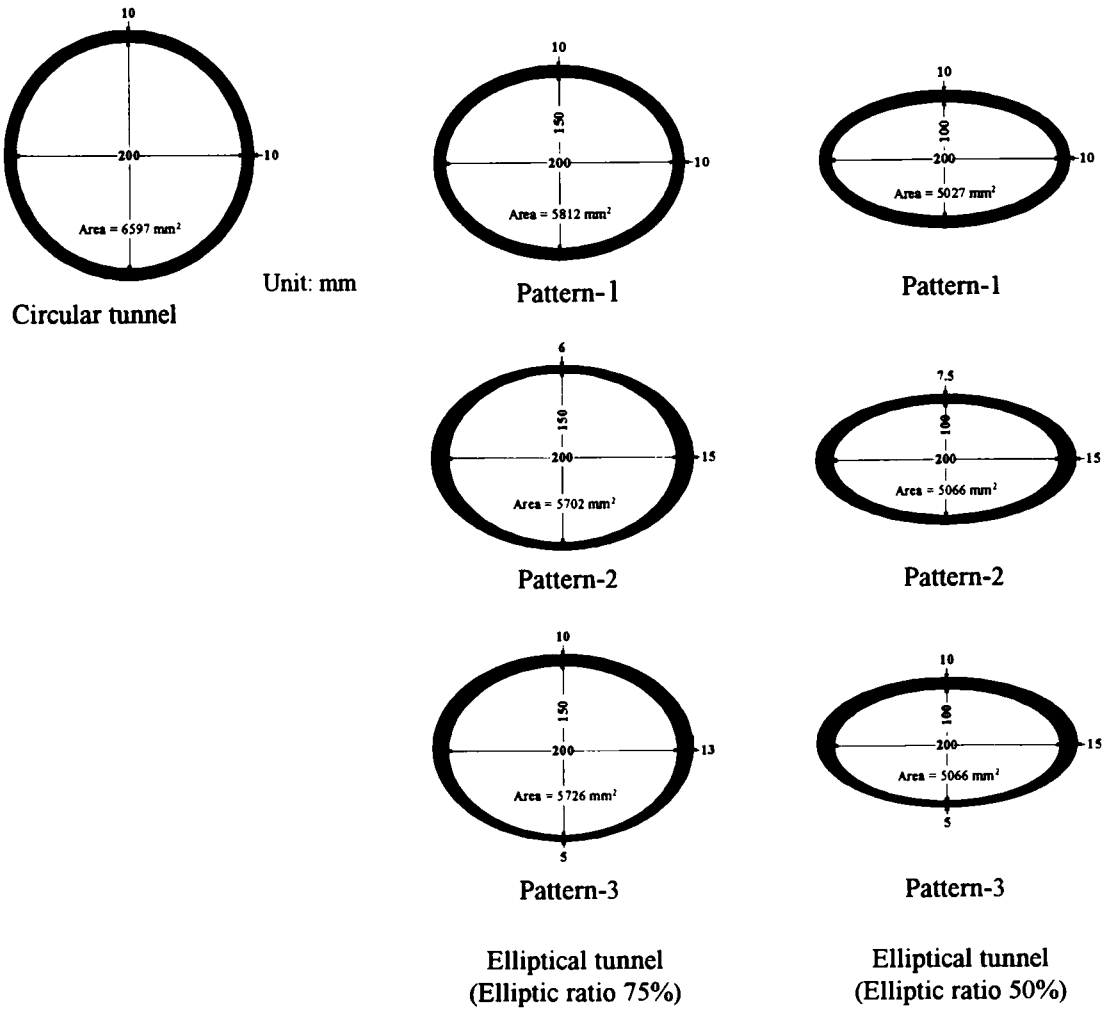

Figure 4.2 Model lining of the circular and the elliptical tunnels in the model loading tests

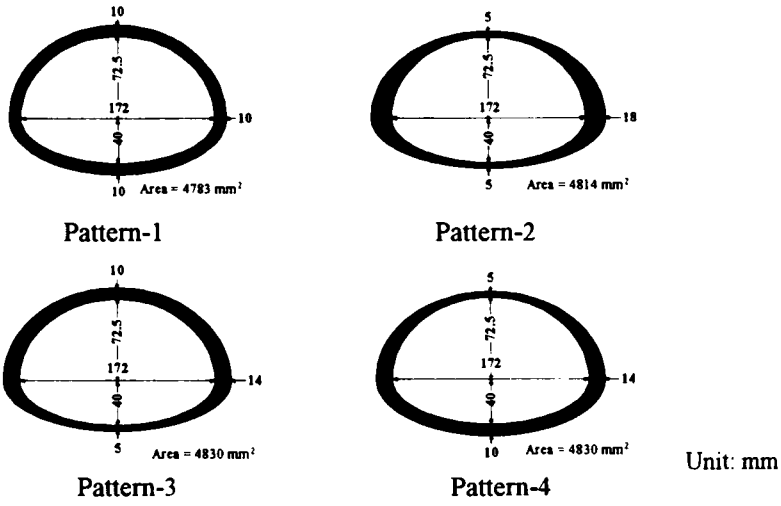

Figure 4.3 Model lining of the horseshoe-shaped tunnel in the model loading tests

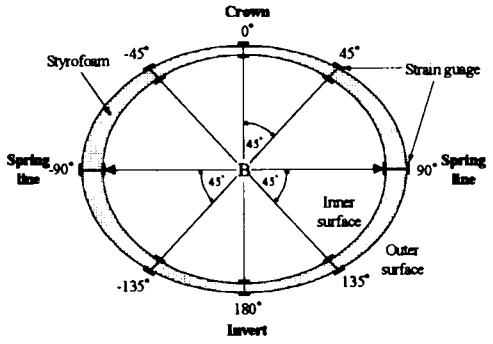

Figure 4.4 Positions of the strain gauges in the model loading tests

The sand is filled up to the designated heights, namely, 0.50B, 0.75B, and 1.0B above the tunnel crown, where B is the inner width of the tunnel model, and the soil surface is leveled. Then, the circumferential strain levels generated at the lining surface are measured. The axial force and the bending moment of each lining section are calculated from the following equations:

$$N = EA\frac{(\varepsilon_i + \varepsilon_o)}{2} \tag{4-1}$$

$$M = 2\frac{EI}{t}\frac{(\varepsilon_i - \varepsilon_o)}{2} \tag{4-2}$$

where N = the axial force, M = the bending moment, E = the elastic modulus, A = the cross-sectional area, I = the moment of inertia, t = the tunnel thickness, ε_i = the strain generated at the inner surface (inner strain), and ε_o = the strain generated at the outer surface (outer strain). Note that the minus sign in the strain means compressive strain.

4.2.2 Material testing

Styrofoam is used as the lining material in this study because it can be simply and manually cut to any shape. However, it has never been used in any model tests before; therefore, the tests to determine its properties, namely, Young's modulus and the compressive strength, are required. Unconfined compression tests are carried out on the cylindrical Styrofoam specimen, which is 50 mm in diameter and 100 mm in length. The results are summarized in **Table 4.2** and demonstrated in **Figures 4.5**(a) and (b). These figures show that the strain levels from the strain gauges are different from the actual strain levels calculated from the displacement of the

specimens. From **Figure 4.5**(b), it is seen that the actual strain levels can be approximated by multiplying the values from the strain gauge by 2.61. This method is further used to calculate the actual strain levels generated on the surface of the tunnel lining in the next section.

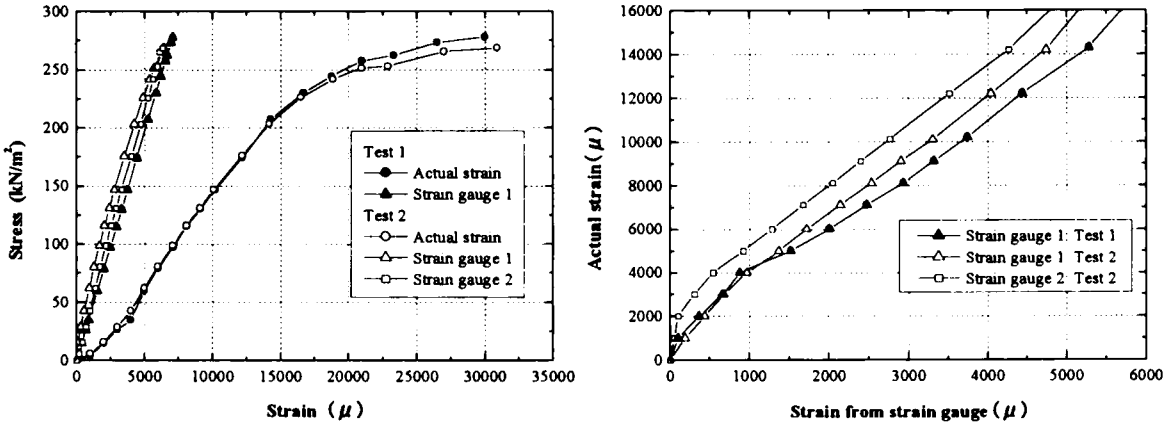

(a) Stress-strain results

(b) Relations between the actual strain and the results from the strain gauges

Figure 4.5 Results of compression tests on the Styrofoam

4.2.3 Results of tests on the elliptical tunnels

In this section, the test results of the circular and the elliptical model linings are presented and discussed. As shown in **Figure 4.2**, three tunnel shapes with elliptic ratio of 50%, 75%, and 100% (circle) are used, where the elliptic ratio is the ratio of the width to the height of the tunnel. The width for all the tunnel shapes is the same, in other words, 200 mm, to express the same utilizable capacity of the tunnel. Moreover, in order to investigate the effects of varying the lining thickness on the lining stability, three patterns of thickness are used for the tunnels with elliptic ratios of 50% and 75%. For each tunnel shape, the area of the tunnel lining for all patterns is set to be the same. The tests are carried out on seven patterns of model linings at cover to width ratios (H_s/B) of 0.5, 0.75, and 1.0.

Effects of the tunnel shape

The results of Pattern-1, the uniform thickness, of the tunnel with elliptic ratios of 50%, 75%, and 100% at an H_s/B of 1.0 are shown in **Figures 4.6**(a)~(d). The results show that when the tunnel shape becomes flat, the axial force decreases as the bending moment increases. Thus, it

can be concluded that for the circular tunnel, the axial force dominantly supports the earth pressure acting on the tunnel. In the case of the elliptical tunnels, the bending moment dominantly supports the tunnel. From the results of the circumferential strain generated at the lining surface, the strain increases when the tunnel becomes flat. For the circular tunnel, no remarkable tensile strain is generated, while in the case of the elliptical tunnels, tensile strain is remarkably generated particularly at the inner side of the crown, the invert, and the outside of the spring line.

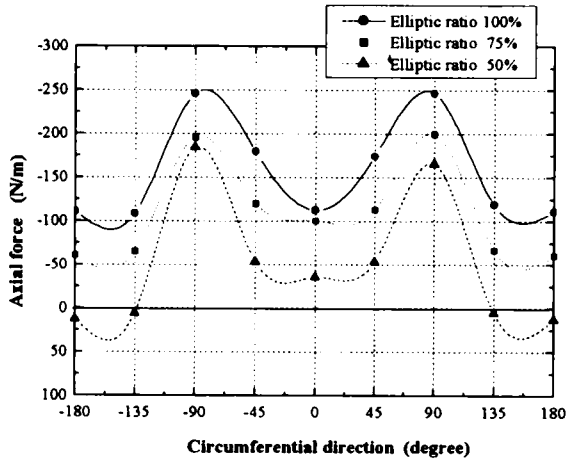

(a) Axial force

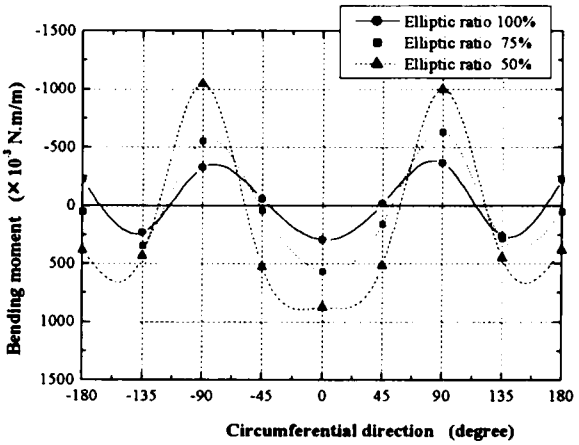

(b) Bending moment

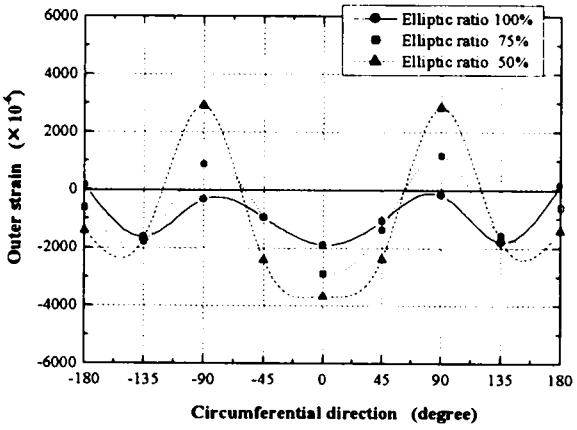

(c) Outer strain

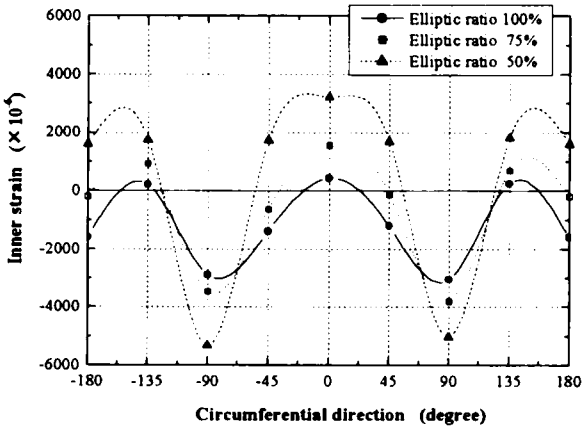

(d) Inner strain

Figure 4.6 Test results of the uniform thickness patterns of the circular and the elliptical tunnels at $H_s/B = 1.0$

From the above results, there is no doubt that, the circular tunnel is the most stable shape in the case of a lining with uniform thickness. For the elliptical tunnels, the flatter the tunnel is, the less stable the tunnel becomes.

Effects of the thickness pattern

Figures 4.7(a)~(d) and **Figures 4.8**(a)~(d) show the comparison results among three thickness patterns for tunnels with elliptic ratios of 75% and 50%, at a cover to depth ratio of 1.0, respectively. For both tunnel shapes, the compressive axial forces generated on Pattern-1 are the smallest values compared with the other patterns. On the other hand, the maximum bending moments generated on Pattern-2 are the smallest values. Pattern-3 is obviously the least stable pattern in view of both section forces. From the results of the tensile strain, the strain levels generated at the lining surface of Pattern-2 are the smallest values, particularly at the inner surface of the tunnel crown and the outer surface of the spring line for both tunnel shapes.

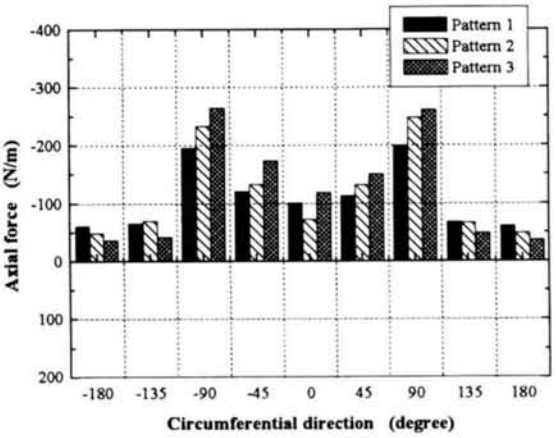

(a) Axial force

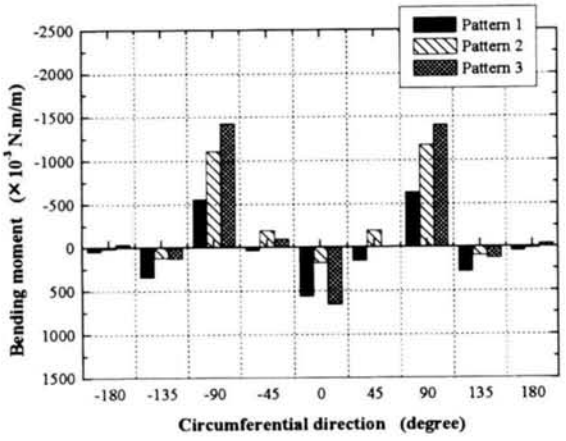

(b) Bending moment

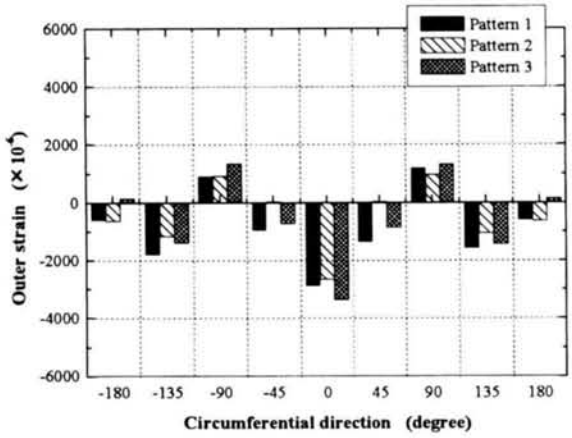

(c) Outer strain

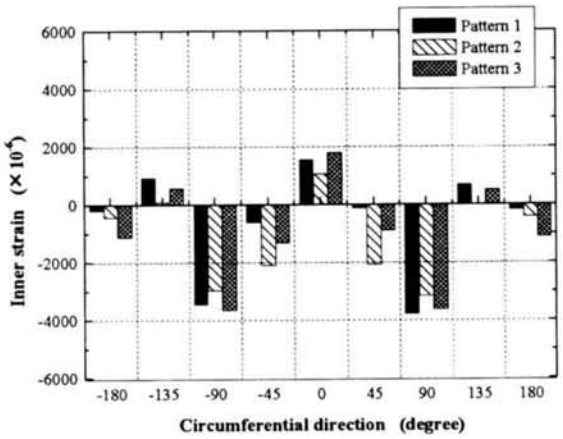

(d) Inner strain

Figure 4.7 Test results for the tunnel with the elliptic ratio of 75% at $H_s/B = 1.0$

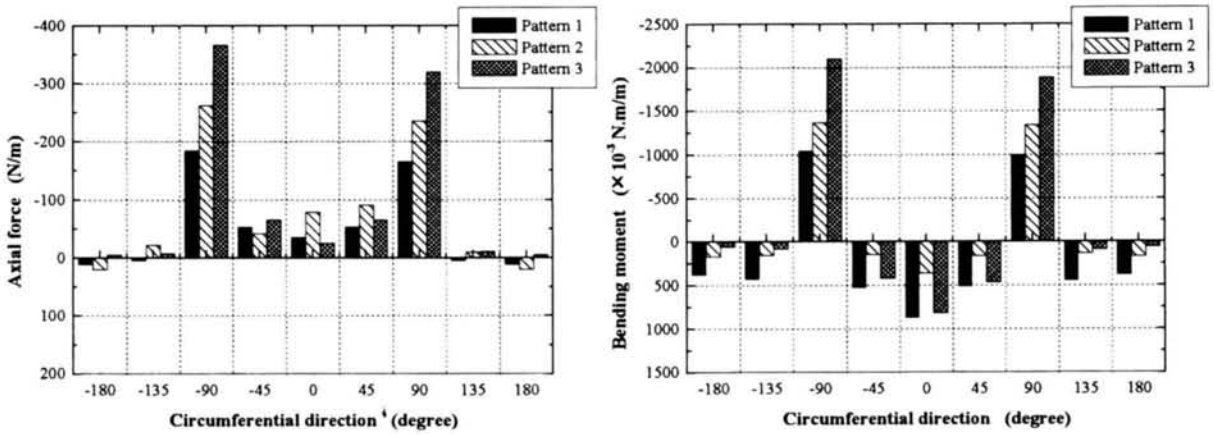

(a) Axial force

(b) Bending moment

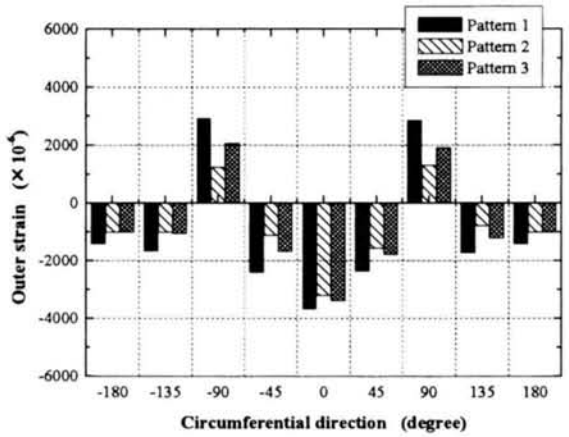

(c) Outer strain

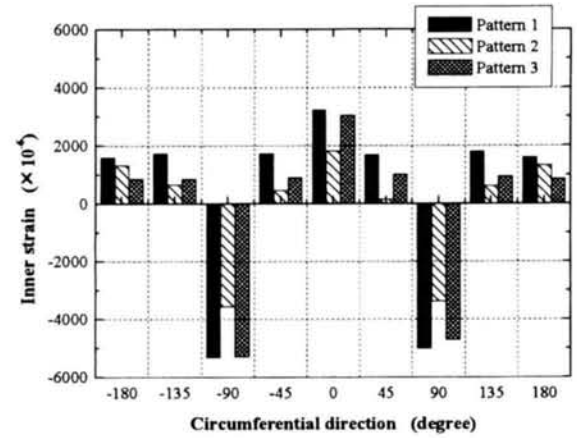

(d) Inner strain

Figure 4.8 Test results for the tunnel with the elliptic ratio of 50% at $H_s/B = 1.0$

In most cases, the segmental lining of shield tunnels is made of reinforced concrete. This is because concrete structure can withstand a small level of tensile stress compared with compressive stress. Tensile strain, generated on the surface of the tunnel lining, expresses the level of tensile stress in the same way. A local crack at the surface of the concrete lining, generated by tensile stress, can cause severe damage to the overall structure. Moreover, in the design process of the tunnel lining, the axial force, and the bending moment at each tunnel section are combined to calculate the stress level at the tunnel surface. The stress level at the lining surface is used to determine the tunnel section and the amount of reinforced steel. For these reasons, the stability is evaluated in this study by the stress level or the strain level at the lining surface. Thus, the most stable thickness pattern should be the thickness pattern which causes a minimum level of tensile strain.

Figures 4.9(a) and (b) show that the tensile strain occurring at the tunnel crown is larger than that of the spring line for all thickness patterns and tunnel depths. In the case of the elliptical tunnels, it is seen from these results that the stress occurring at the tunnel crown is the most serious value. Comparing the tensile strain at the tunnel crown for all thickness patterns, the tensile strain levels of the thickness Pattern-2 are significantly lower than those of the other two patterns, except for the case in which the elliptic ratio is 75% at the cover to width ratio of 0.5.

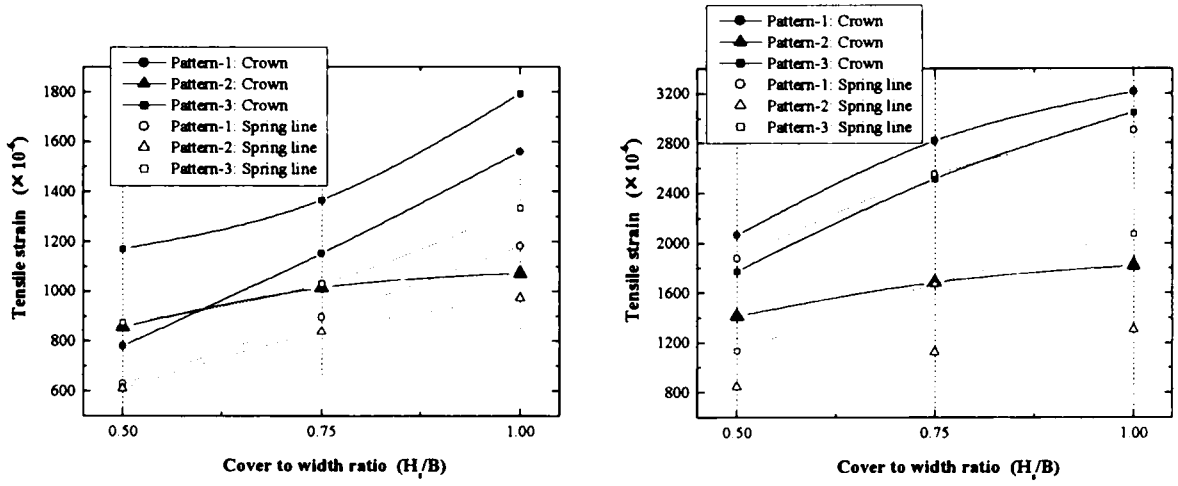

(a) Elliptic ratio of 75%

(b) Elliptic ratio of 50%

Figure 4.9 Plots between the tensile strain and the cover to width ratio of the elliptical tunnels

From the above results, Pattern-2, which is thicker at the spring line but thinner at the crown and the invert compared with the uniform-thickness pattern, is considered to be the most stable pattern among the elliptical tunnels.

4.2.4 Results of tests on the horseshoe-shaped tunnels

In this section, the test results for the horseshoe-shaped tunnels, shown in **Figure 4.3**, are demonstrated and discussed. The horseshoe shape is created from two ellipses that have the same width. Four thickness patterns are used in this test. All of them have the same inner-sectional shape and lining area. The variation in the thickness pattern is designed to increase the thickness at the spring line. Since the total area of the lining must be constant, the thickness at the crown or the invert is reduced. The tests are carried out at cover to width ratios (H_s/B) of 0.5, 1.0, and 1.5.

The results of the member forces and the strain, at a cover to depth ratio of 1.0, are shown in **Figures 4.10**(a)~(d). Pattern-1 (uniform thickness) causes minimum axial forces. At the invert,

however, the tensile axial force is generated. For the maximum bending moment, Pattern-1 shows the smallest value. However, in view of the tensile strain, Patterns-2 and -4 cause minimum strain levels at the lining surface for both inner and outer sides.

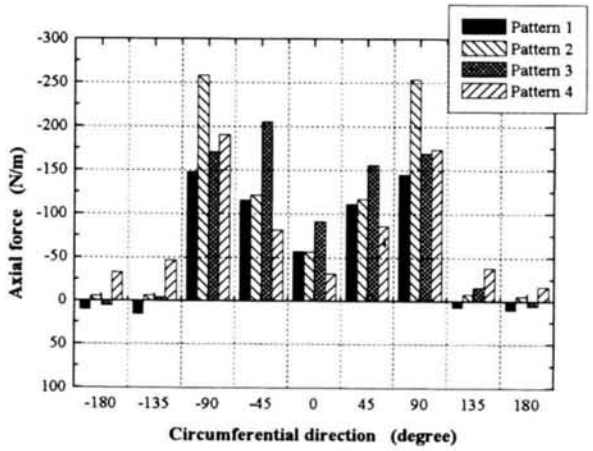

(a) Axial force

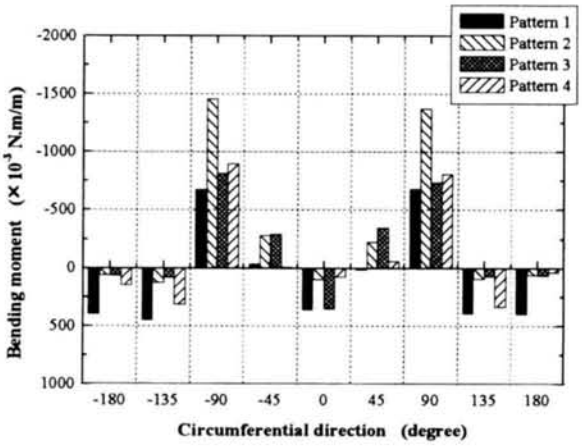

(b) Bending moment

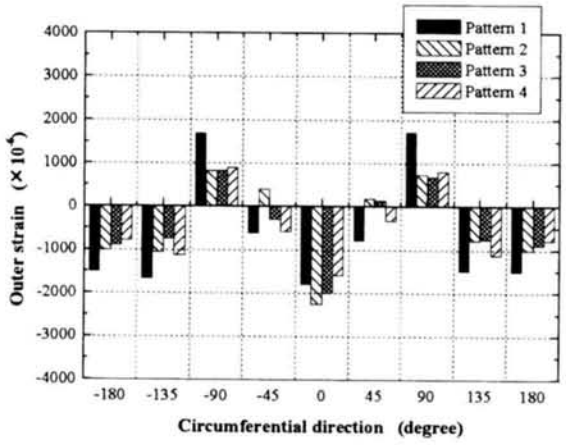

(c) Outer strain

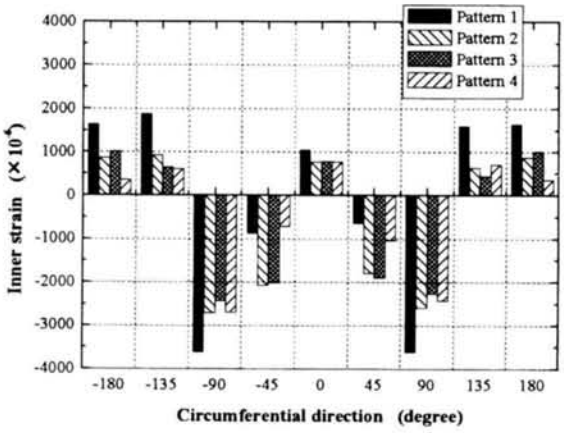

(d) Inner strain

Figure 4.10 Results of the tests on the horseshoe-shaped tunnel at $H_s/B = 1.0$

From the plots of the tensile strain and the cover to width ratios (H_s/B) of all patterns in **Figures 4.11**(a)~(d), it is obvious that the tensile strain increases with an increase in the over to depth ratio. The tensile strain level at the spring line are the maximum values for Patterns-1 and -4 while the tensile strain levels at invert are the maximum values for Patterns-2 and -3. For thickness Pattern-2, the tensile strain levels at all positions, namely, the crown, the invert, and the spring line are nearly the same. It shows that the tensile stress level of Pattern-2 is the most uniform in comparison to other patterns.

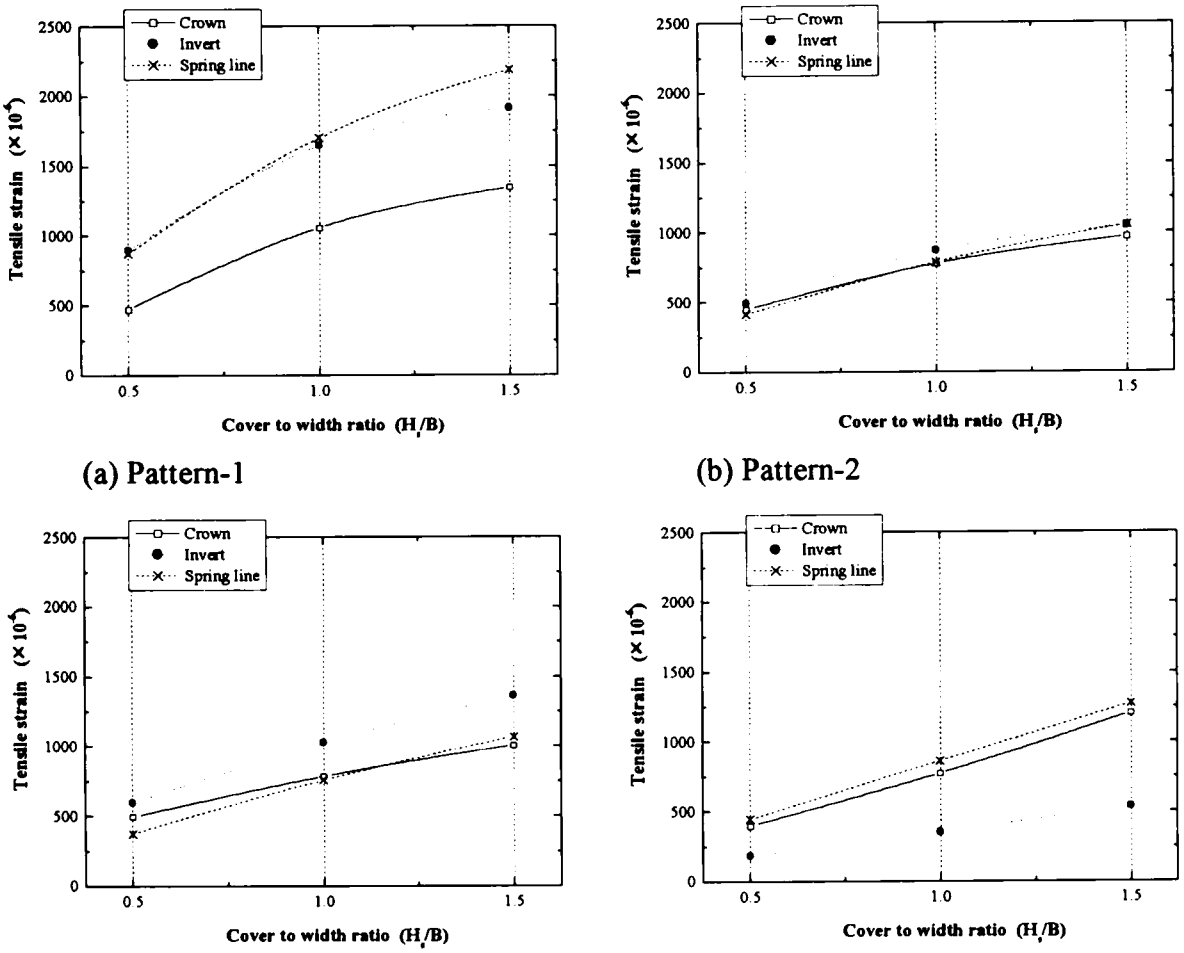

Figure 4.11 Plots between the tensile strain and the cover to width ratio of the horseshoe-shaped tunnel

Figure 4.12 shows that there is no remarkable difference between Patterns-2 and -4 until H_s/B = 1.0, however, when $H_s/B \geq 1.5$, Pattern-2 becomes superior. In this figure, the letters above the bars stand for the position where the maximum tensile strain took place, in order words, I = invert, S = spring line. They show that when the tunnel depth is shallow, the invert is at the severest point, but when the tunnel depth deepens, the spring line becomes the critical point instead.

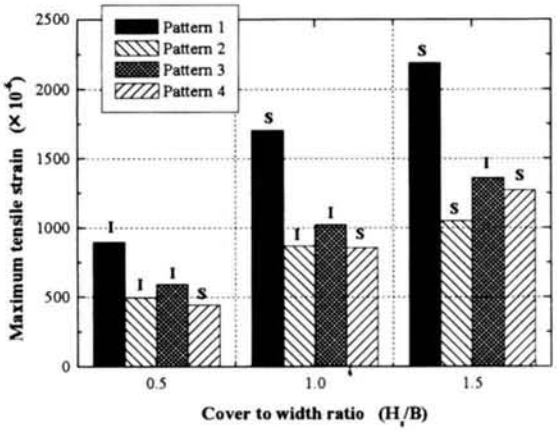

Figure 4.12: Plots between the maximum strain and the cover to width ratio

From the view of tensile strain, therefore, Patterns-2 and -4, which are thicker at the spring line, but thinner at the crown compared with the uniform-thickness pattern, are the most stable thickness patterns.

4.2.5 Conclusion

The results of the model loading tests show that the member forces of a tunnel lining increase when the overburden depth increases. At the same overburden depth, the member forces, namely, the axial force and the bending moment, generated in the tunnel lining, increase as the tunnel shape becomes flatter, i.e., smaller in elliptic ratio. For the circular tunnel, the axial force is the main supporting force against the acting earth pressure. On the contrary, the flat-shaped tunnels are mainly supported by the bending moment at the spring line. In the case of a uniform lining, the intensity of the member forces, namely, the axial force and the bending moment, can be used effectively to evaluate the stability of the tunnel lining. However, for a nonuniform tunnel, where the thickness of the tunnel lining is not constant, the intensity of the axial force and the bending moment can not express the stability of the tunnel lining clearly. Thus, the intensity of the stress or the strain generated at the lining surface is directly used to evaluate the stability instead. In this research, the stability of tunnel linings is evaluated by the intensity of the tensile stress at the surface of the tunnel lining. A lower tensile stress means a more stabile tunnel lining. The tensile stress and strain normally occur at the inner surface of the tunnel crown, the invert, and the outer surface of the spring line. For deep overburden depths, the tensile stress at the spring

line is dominant. For the same tunnel shape, changes in the thickness pattern cause the stability of the tunnel lining to change. The thickness pattern for which the thickness is thicker at the spring line and thinner at the tunnel crown and the invert, is the most stable pattern. This shows that the stability of a tunnel lining can be improved by varying the thickness pattern and not increasing the overall lining area.

4.3 Two-way loading tests

As proved in the previous section from the results of model loading tests that the stability of flat-shaped tunnels can be improved by varying the thickness pattern of the tunnel linings. However, there have been several discussions about the reliability of the model loading tests which use Styrofoam as the lining material. The stiffness level of Styrofoam is lower than the surrounding sand. This differs from a real construction in that the stiffness of a concrete lining is very high compared with the surrounding ground. Moreover, the properties of Styrofoam, for which that has Poisson's ratio is nearly zero, cause many comments in regards to the testing results.

In order to investigate the mechanical behavior of a nonuniform tunnel lining more accurately, a two-way loading model testing device under plane strain conditions has been developed. The two-way loading testing device is used to investigate the mechanical behavior of the tunnel linings under several loading patterns. Two-way loading means loading in the directions of the tunnel crown and the spring line, which will herein be referred to as the vertical and the horizontal directions, respectively. The variation in the ratio of horizontal load to vertical load expresses the coefficient of earth pressure at rest (K_0) of the ground. For the model lining, plaster is used as the lining material because it has nearly the same properties as the concrete that will be further described in the next section.

The strain generated at each loading step is measured, and the member forces, namely, the axial force, and the bending moments are calculated. The laser displacement gauge is also installed and used to measure the displacement of the tunnel crown and the spring line. The mechanical behavior and the stability of the tunnel lining are compared and evaluated from the standpoint of the four values, namely, strain, axial force, bending moment , and displacement.

In this chapter, two types of tunnel lining tests are reported. The first group is done on the circular and the elliptical tunnels. The effects of the tunnel shape, the elliptical ratio, and the thickness pattern are demonstrated and discussed. The second group is done on the horseshoe-shaped tunnels. As will be demonstrated in this chapter, the efficiency of increasing the stability of the tunnel lining by varying the lining thickness will be demonstrated and discussed.

4.3.1 Experimental apparatus, testing procedure, and model lining

Experimental apparatuns and testing procedure

The two-way loading model testing device is shown in **Figure 4.13**. The soil chamber is mainly made of steel, but an acrylic plate is used but for the cover plate, to reduce the surface friction force. Four air pressure cylinders are installed to load the surrounding soil through the movable loading plates. The pressure levels loaded at the tunnel crown and the invert are the same values which are called the vertical direction. The level of pressure loaded at the left and the right spring lines have the same values are called the horizontal direction. In these tests, the ratio of the horizontal pressure to the vertical pressure is thought of as the load step. Sponge plates are installed between the loading plates and the sand to make the pressure distribution to sand uniform. Four load cells are installed to measure the amount of loading, strain gauges are used to measure the strains generated at the lining surface and two laser displacement gauges are installed to measure the displacement of the tunnel crown and the spring line.

The model lining is first set at the center of the soil chamber, as shown in **Figure 4.14**(a). Then, the soil chamber is filled to the top with sand, as seen in **Figure 4.14**(b). After leveling the sand surface, the cover plate is placed on the top, as shown in **Fig. 4.14**(c). Finally, the soil and the model lining are loaded by four cylinders, and the strain and the displacement of the model lining are measured at each loading step.

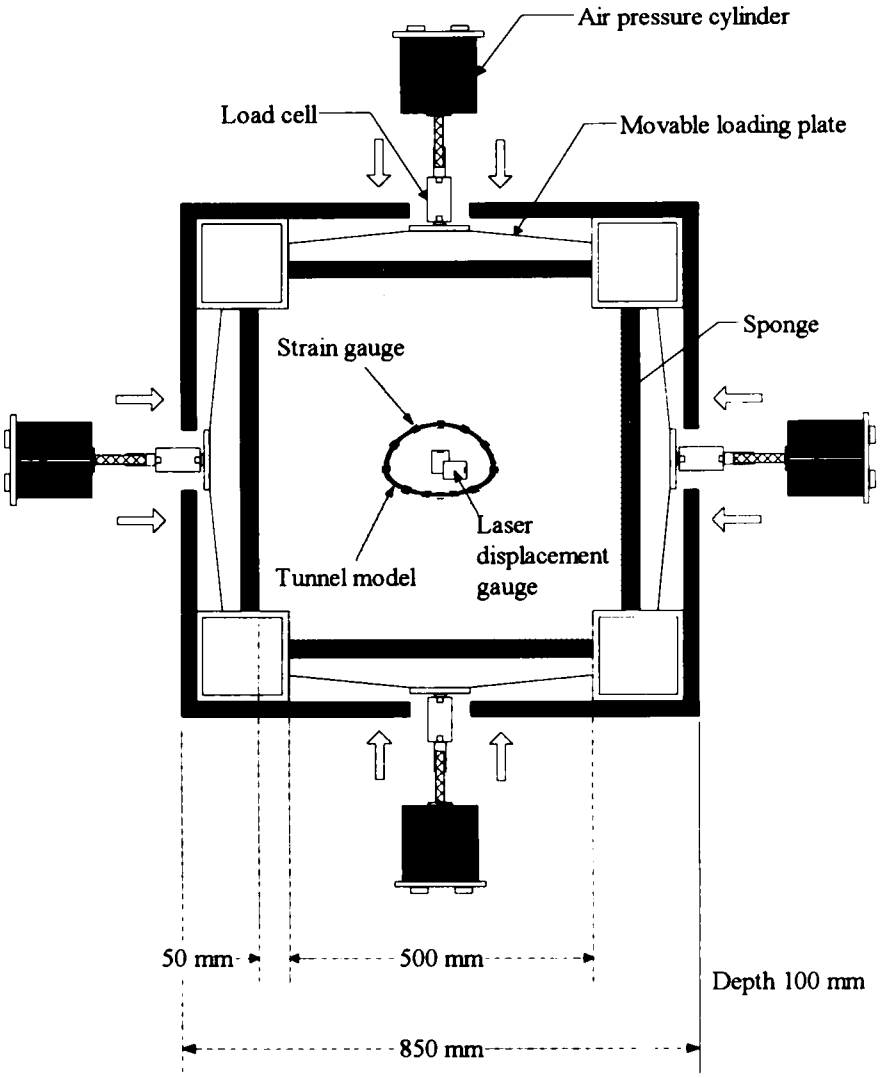

Figure 4.13 Two-way loading model testing device

At first, the soil is loaded in both of the vertical and the horizontal directions until 12 kPa to minimize the void ration and to compact the sand to dense conditions. From the pilot tests, the results show that the pressure does not transfer to the model lining if the load is lower than 12 kPa. After reaching a confined pressure of 12 kPa, all data are reset at zero. Then, the pressure increases gradually from zero to 60 kPa for the vertical direction and 18 kPa for the horizontal direction whose the lateral pressure ratio equals 0.3. This pressure level is the starting point of the measuring. Next, only the horizontal pressure increases gradually and the measuring is done when the increasing step equals 6 kPa. The measurement is done until the horizontal pressure reaches 90 kPa which the lateral pressure ratio equals 1.5. It can be simply summarized that the tests are carried out from a lateral pressure ratio 0.3 to 1.5.

(a) Setting all equipment and the tunnel model

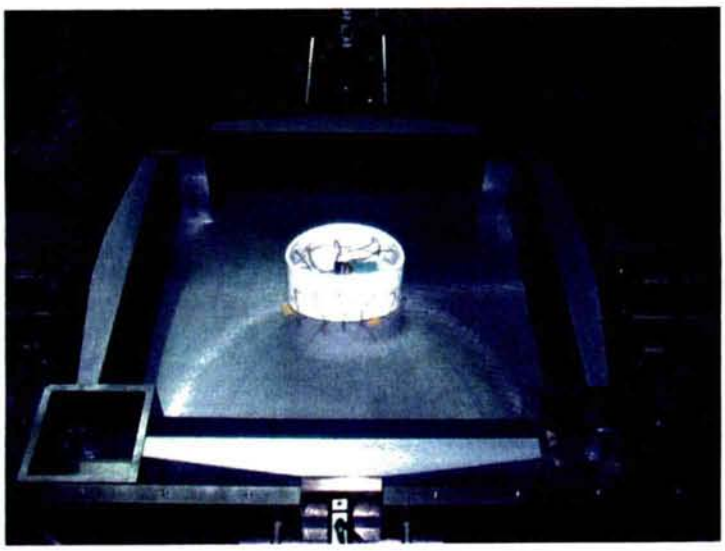

(b) Filling sand

(c) Placing the cover plate and then loading

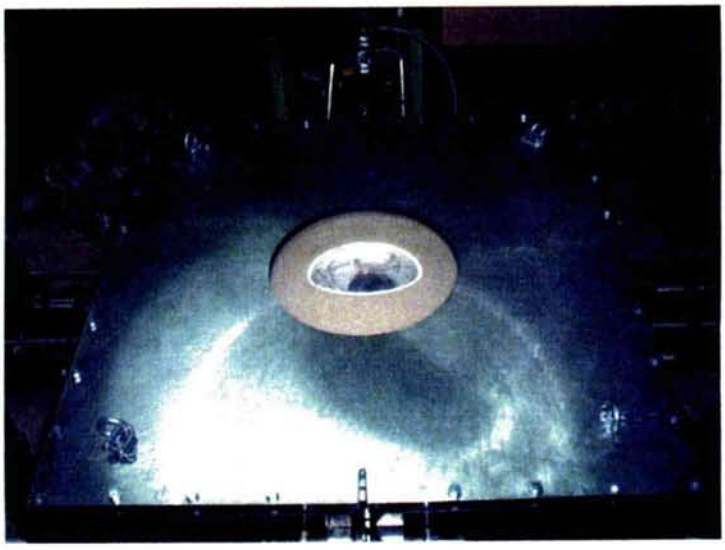

Figure 4.14 Testing procedure of the two-way loading tests

In this test, Toyoura sand is used to produce the experimental ground and the model lining is made from a mixture of plaster and water. The properties of the Toyoura sand and the mixing plaster are summarized in **Tables 4.3** and **4.4**, respectively.

Table 4.3 Properties of the sand and the model ground in the two-way loading tests

Material name	Toyoura sand
Specific weight	2.64
Average void ratio	0.67
Maximum void ratio	0.98
Minimum void ratio	0.61
D_{50}	180μm
Uniformity	1.52
Density	1,580 kg/m^3
Relative density	84.8%
Frictional angle	38.5°

Table 4.4 Properties of the model lining in the two-way loading tests

Material name	Plaster
Density	802.63 kg/m^3
Unconfined compressive strength	2.65 MPa
Young's modulus	1,933 MPa
Poisson's ratio	0.218

Model lining

The tests are carried out on four types of tunnel shapes, namely, circular, elliptical (with elliptic ratios of 75% and 50%), and horseshoe. The size and the shape of the model linings are shown in **Figures 4.15** and **4.16**. As shown in the figures, the inner shape and the area of tunnel lining for each tunnel type are the same. Only the outer shape is changed in order to investigate the effects of the thickness pattern. This is based on the concept that ordinarily the inner shape of a tunnel is determined by the architectural conditions. The same inner shape means the same utilization capacity of the tunnel, and the same tunnel area means the same cost for constructing the tunnel lining.

In this model test, the model lining is simulated as the 1/100 of the real tunnel size; thus, it so it can be said that this test tries to investigate the behavior of the elliptical tunnel 20 m in width and the horseshoe-shaped tunnel 17.2 m in width. The thickness of the uniform tunnel is 6 mm. It is determined by the similitude law for tunnel structures as described in Appendix A, to model a concrete lining 1.0 m in width. The nonuniform thickness patterns are determined from the optimal shape obtained from the numerical analysis, as will be further described in Chapter 5.

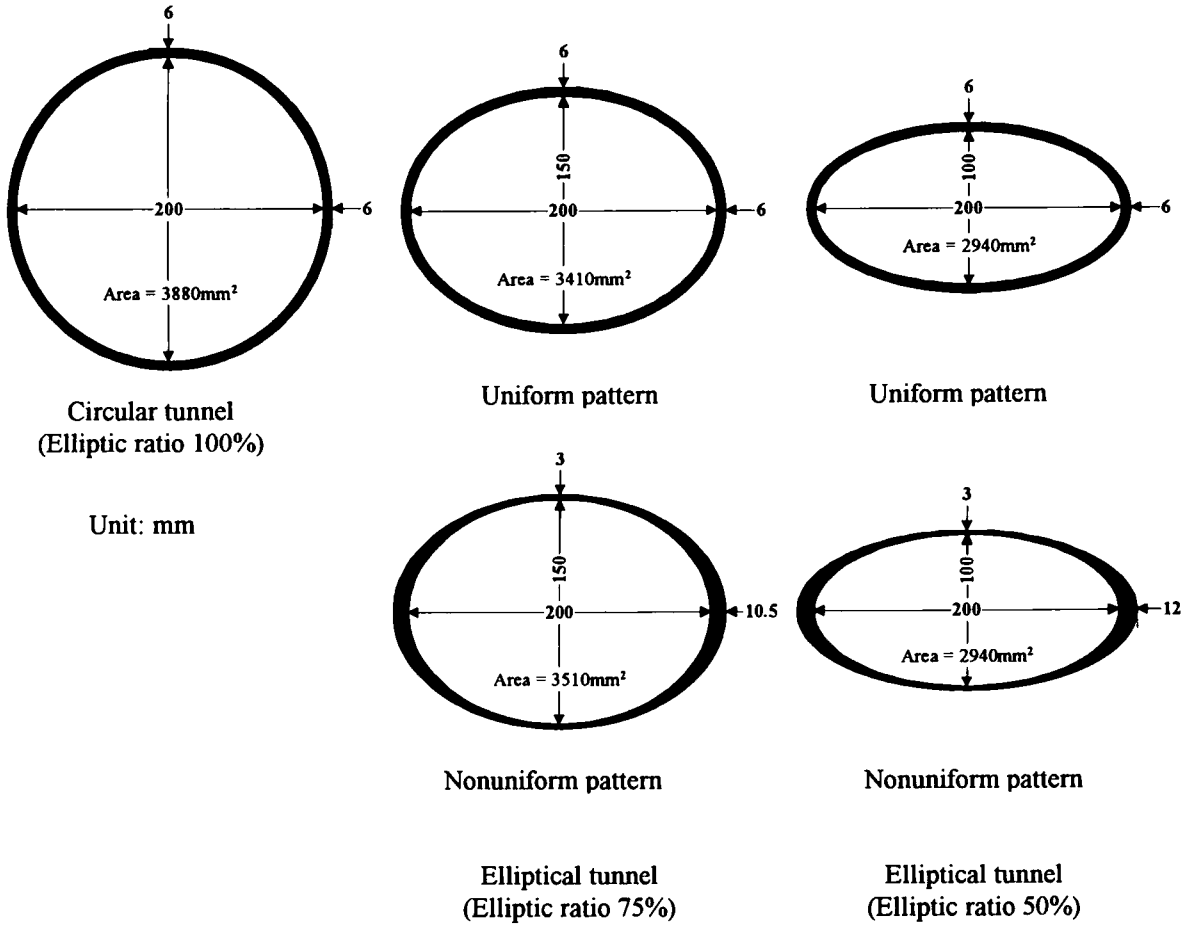

Figure 4.15 Model lining of the circular and the elliptical tunnels in the two-way loading tests

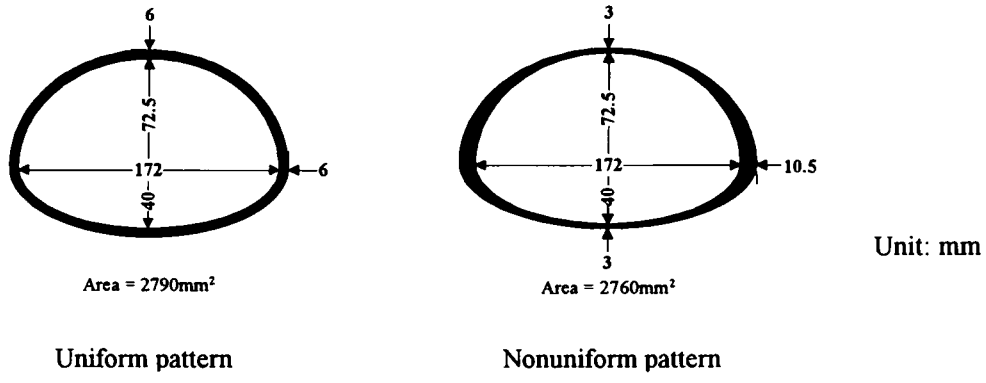

Figure 4.16 Model lining of the horseshoe-shaped tunnel in the two-way loading tests

Figure 4.16 Model lining of the horseshoe-shaped tunnel in the two-way loading tests

To measure the member forces generated on the tunnel lining after loading, twenty-four strain gauges are symmetrically attached at the following positions: 0° (crown), 30° , 60° , 90° (spring line), 120° , 150° , and 180° (invert), on both outer and inner sides of the lining surface, as shown in **Figure 4.17**. For each loading step, the circumferential strain levels generated at the lining surface and the displacements of the tunnel crown and the spring line are measured. The axial force and the bending moment of each lining section are calculated from the **Equations 4-1** and **4-2**.

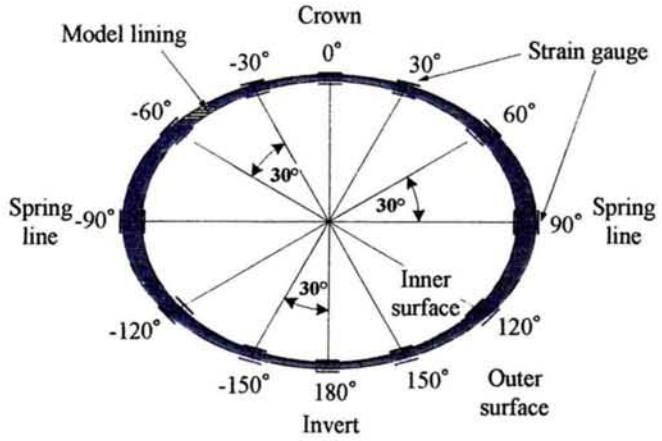

Figure 4.17 Positions of the strain gauges in the two-way loading tests

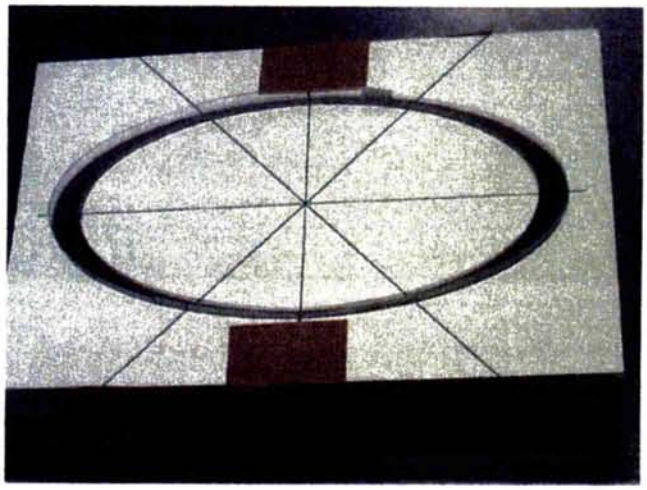

Figure 4.18 Styrofoam mold of the model lining

4.3.2 Material testing

The model lining is made by mixing plaster material with water at a ratio of 1.0:1.1 for plaster : water. The mixed plaster is poured into the Styrofoam mold, as shown **Figure 4.18**. Then, the water is completely dehydrated from the plaster over forty-eight hours. The unconfined compression tests are carried out to determine the properties of the mixing plaster. The results of eight cylindrical specimens, 100 mm in length and 50 mm in diameter, are shown in **Figures 4.19**(a) and (b). The testing results are summarized again in **Table 3.5**. The average results are further used to calculate the member forces in the lining section after loading.

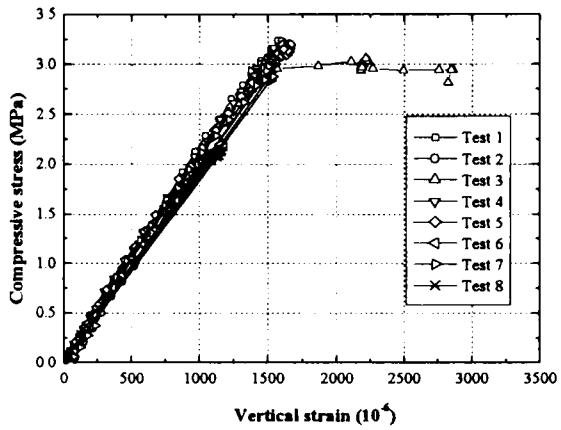

(a) Relations between compressive stress and vertical strain

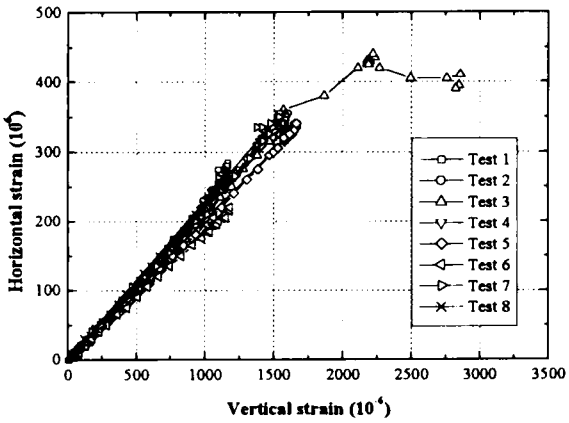

(b) Relations between vertical and horizontal strain

Figure 4.19 Compression test results for the mixed plaster material

Table 4.5 Compression test results of the mixed plaster material

Specimen	Compressive strength (Mpa)	Elastic modulus (Mpa)	Poisson's ratio
1	1.97	1774	0.241
2	3.03	2009	0.224
3	3.00	1950	0.215
4	3.09	2029	0.226
5	3.11	1901	0.201
6	2.06	1960	0.188
7	2.91	1950	0.223
8	2.08	1891	0.224
Average	2.65	1933	0.218

4.3.3 Results of tests on the elliptical tunnels

In this section, the results of tests on the circular and the elliptical model linings are presented and discussed. As shown in **Figure 4.15**, three tunnel shapes, namely, elliptical tunnels with elliptic ratios of 50%, 75%, and 100% (circle) are tested. For the tunnels with elliptic ratios of 50% and 75%, two thickness, uniform and nonuniform, are considered. Two laser displacement gauges are installed to measure the displacement of the tunnel crown and the spring line for the circular tunnel and for the elliptical tunnel with the elliptic ratio of 75% tunnels. Due to the limitation of installing space, only one laser displacement gauge is installed to measure the tunnel crown movement for the tunnel with the elliptic ratio of 50%. The data are collected from the lateral pressure ratio of 0.3 to 1.5.

Effects of the tunnel shape

The results of the uniform patterns for the elliptical tunnels with elliptic ratios of 50%, 75%, and 100%, when the lateral pressure ratio (P_H/P_V) equals 0.5, are shown in **Figures 4.20**(a)~(d). The bending moment, especially at the spring line, becomes dominant when the tunnel becomes flatter, while the axial forces decrease when the elliptic ratio decreases. It is obvious that the bending moment plays the main role in supporting the acting earth pressure in the case of flat-shaped tunnels. Considering the circumferential strain generated along the lining surface, the tensile strain levels at the inner surface of the tunnel crown and at the outer surface of the spring line become significantly higher as the tunnel becomes flatter. The distributions of strain for the circular tunnel are the most uniform. This means that the stress level along the tunnel section is nearly uniform. There is no doubt that the circular shape is the most stable shape and that the stability of the tunnel lining decreases as the tunnel lining becomes flatter.

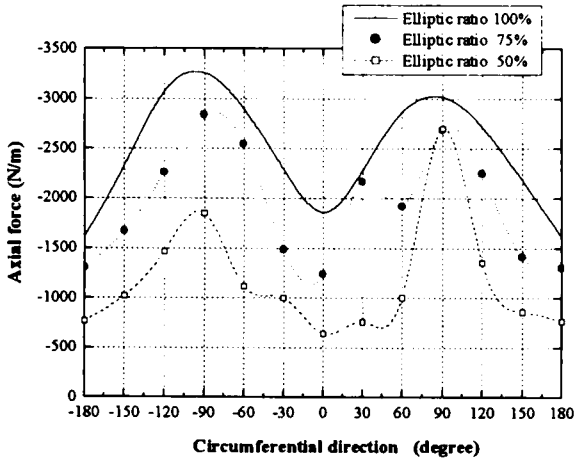

(a) Axial force

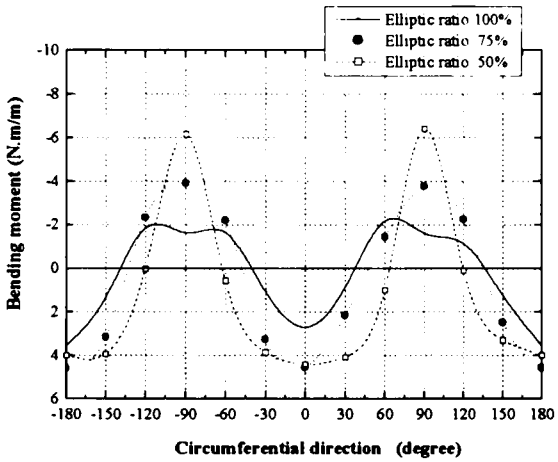

(b) Bending moment

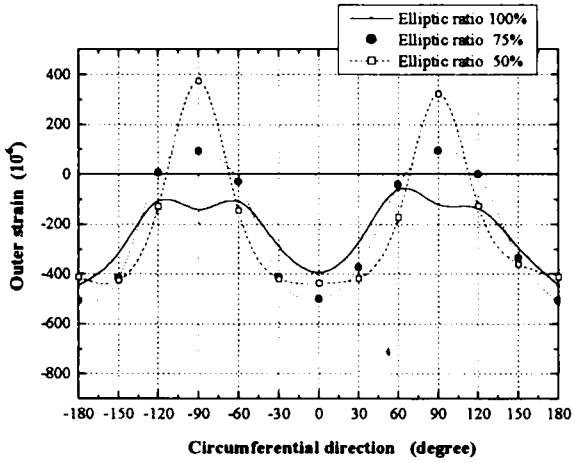

(c) Outer strain

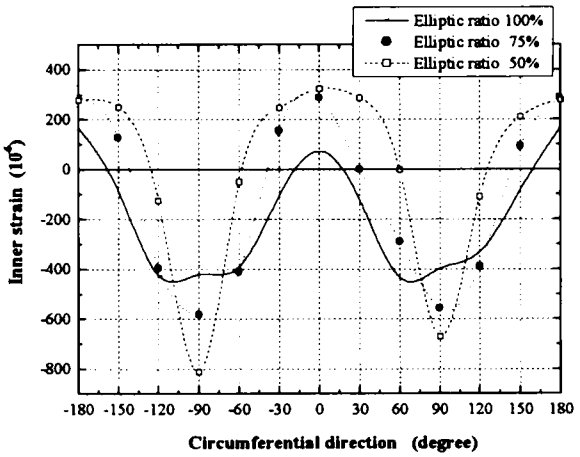

(d) Inner strain

Figure 4.20 Test results for the uniform thickness patterns of the circular and the elliptical tunnels at $P_H/P_V = 0.5$

Effects of the thickness patterns

Figures 4.21(a)~(d) and **Figures 4.22**(a)~(d) show the comparison results between the uniform and the nonuniform thickness patterns for tunnel with elliptic ratios of 75% and 50% at a P_H/P_V of 0.5, respectively. For the tunnel with the elliptic ratio of 75%, the axial force of the nonuniform tunnel is remarkably smaller than the uniform one. The maximum bending moment of the uniform pattern occurred at the tunnel crown, while the nonuniform pattern, the bending moment, becomes the largest at the spring line. From the view point of circumferential strain, there is no significant difference for the outer strain. However, when considering the inner strain, the strain levels of the nonuniform tunnel are lower than, those of the uniform tunnel at all sections. In the case of the tunnel with the elliptic ratio of 50%, the axial forces occurring in both patterns do not significantly differ. For the bending moment, the positions where the maximum moment occurred are the same as for the tunnel with the elliptic ratio of 75%. It can be concluded that for the nonuniform tunnel, the moment at the spring line is dominant part in supporting the tunnel. From the strain results, the nonuniform pattern shows remarkable efficiency in reducing the amount of strain, of both the outer and the inner surfaces.

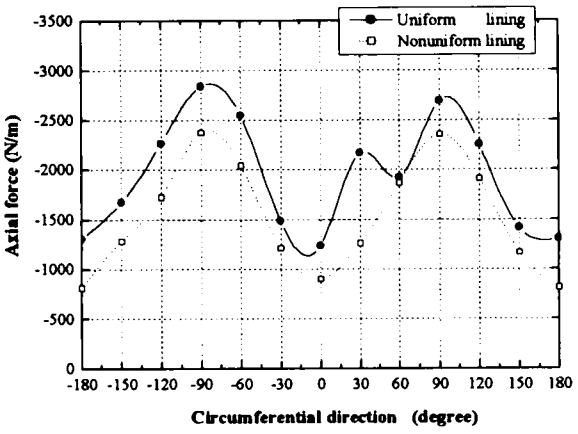

(a) Axial force

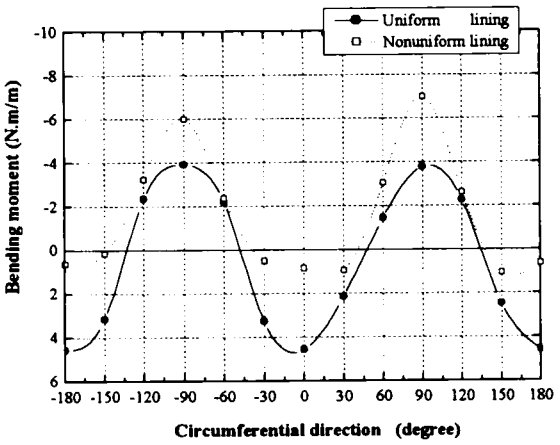

(b) Bending moment

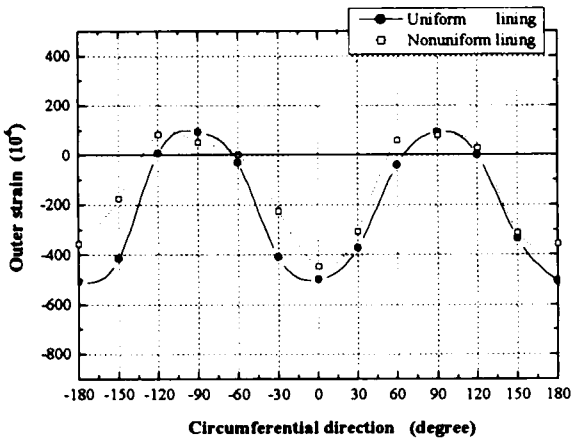

(c) Outer strain

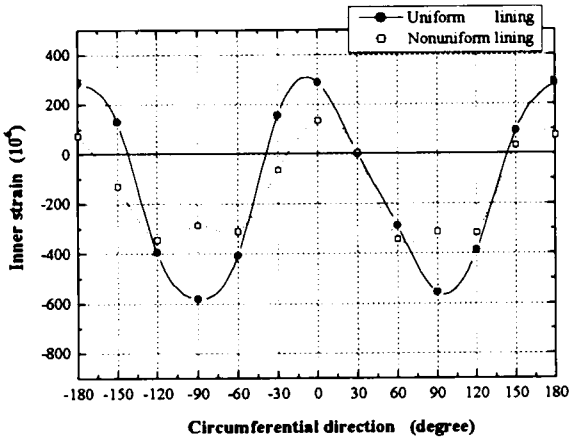

(d) Inner strain

Figure 4.21 Test results for the tunnel with the elliptic ratio of 75% at $P_H/P_V = 0.5$

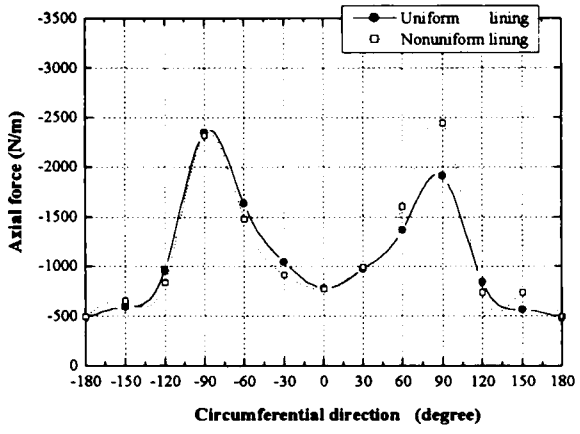

(a) Axial force

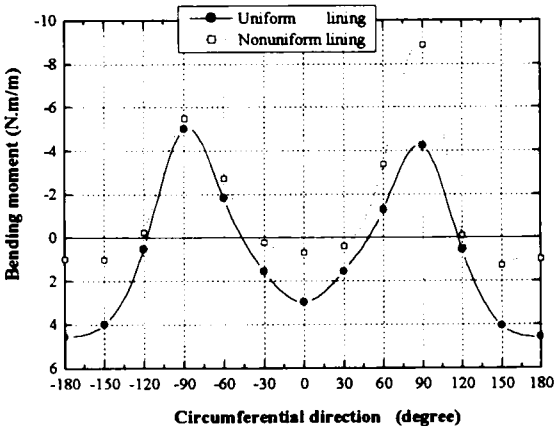

(b) Bending moment

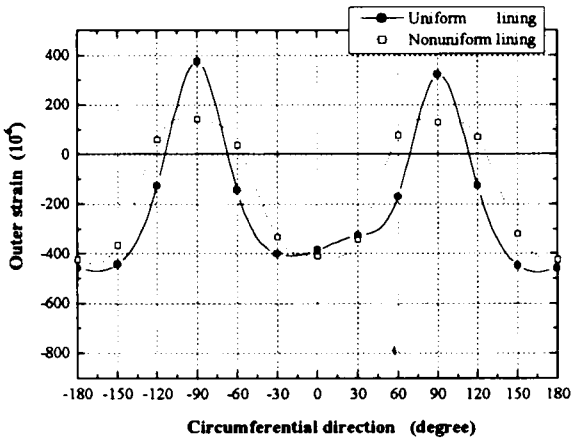

(c) Outer strain

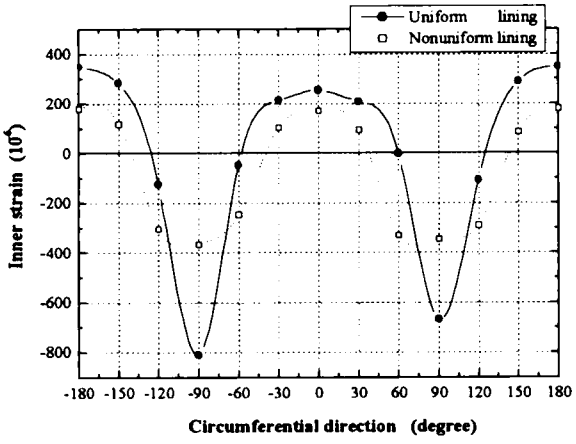

(d) Inner strain

Figure 4.22 Test results for the tunnel with the elliptic ratio of 50% at $P_H/P_V = 0.5$

As mentioned in the previous section, it is difficult to compare the stability of uniform and nonuniform linings by the member forces, namely, axial force and the bending moment. It is simpler and more practical to evaluate the stability directly from the measured circumferential strain levels. For a concrete structure, the occurrence of tensile strain is severe and can develop into a local crack. Based on this concept, the nonuniform pattern shows remarkable efficiency in improving the stability of the tunnel lining.

The plots between the tensile strain and the lateral pressure ratio (P_H/P_V) of the elliptical tunnels are shown in **Figures 4.23**(a)~(b). They show that when the lateral pressure ratio increases, the tensile strain decreases. It can be concluded that the horizontal pressure has the important role of supporting the tunnel. Thus there is no doubt that the tunnel lining becomes more stable when the horizontal pressure increases. For the tunnel with the elliptic ratio of 75%, the tensile strain levels occurring at the tunnel crown are the maximum values, while the tunnel with the elliptic ratio of 50% shows the most severe positions at the spring line. The tensile strain levels at the outer surface of the spring line grow larger and more severe as the tunnel becomes flatter. For all cases of the lateral pressure ratio, the tensile strain levels occurring in the nonuniform lining are smaller than those in the uniform one. The results prove that the nonuniform lining, i.e., the optimal shape, has the efficiency to improve the stability of the tunnel lining in all lateral pressure ratio cases.

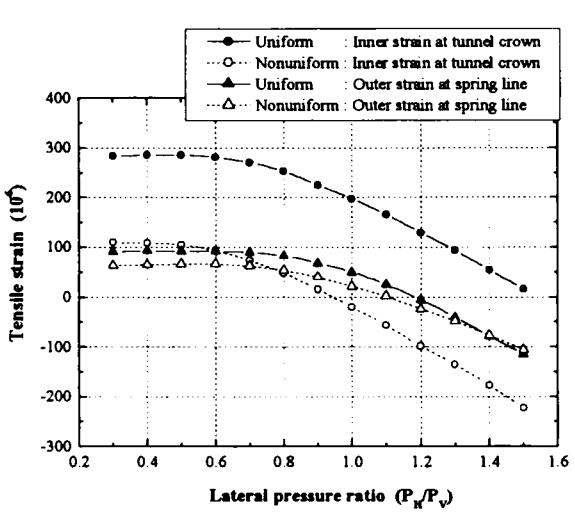

(a) Elliptic ratio 75%

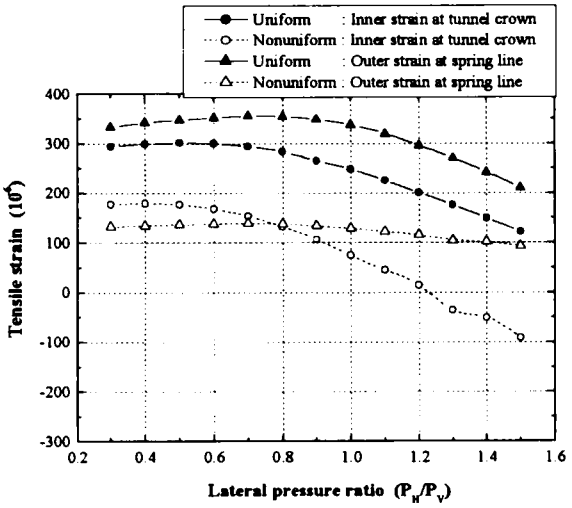

(b) Elliptic ratio 50%

Figure 4.23 Plots between the tensile strain and the lateral pressure ratio of the elliptical tunnels

From the plots of displacement in **Figure 4.24**, it is obvious that the displacement increases as the tunnel becomes flatter. When the lateral pressure ratio increases, the displacement decreases. These results support all the conclusions mentioned in the previous sections. The crown displacements of the nonuniform pattern are generally smaller than those of the uniform pattern. From **Figure 4.25**, in the case of the tunnel with the elliptic ratio 75%, both the crown and the spring line displacements can be reduced using the nonuniform lining. Thus, it can be concluded from the above results that the stability of the nonuniform lining has the efficiency to improve the stability of the tunnel lining. At the same pressure level, the nonuniform tunnel deformed on a smaller scale in comparison to the uniform one.

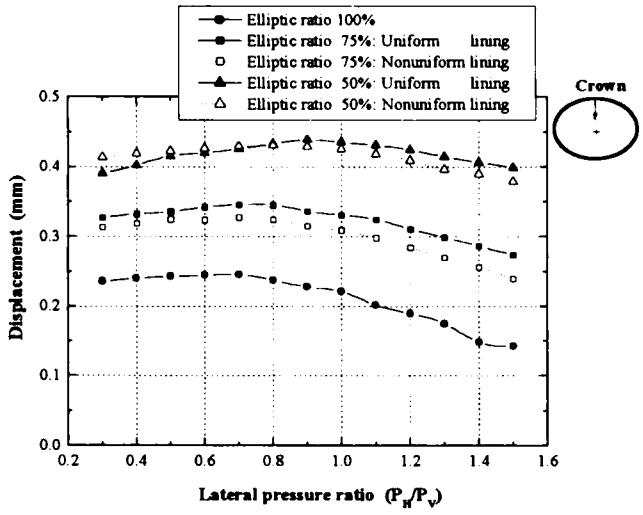

Figure 4.24 Displacement of the tunnel crown for the elliptical tunnels

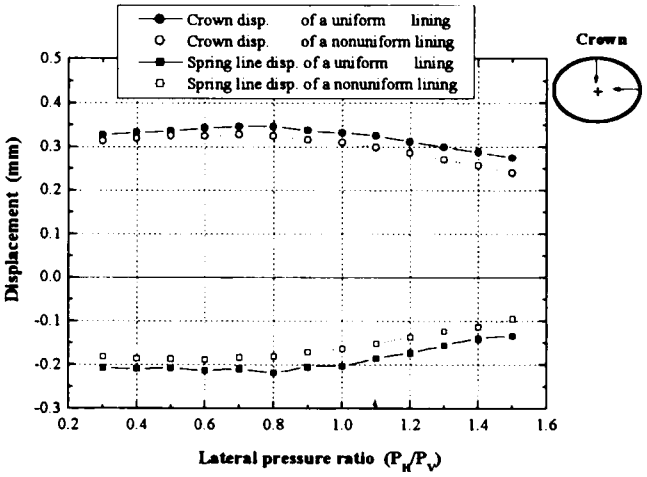

Figure 4.25 Displacement of the tunnel with the elliptic ratio of 75%

4.3.4 Results of tests on the horsehoe-shaped tunnel

In this part, the results of tests on the horseshoe-shaped tunnel, shown in **Figure 4.16**, are reported and discussed. In this study, the horseshoe shape is created from two ellipses, upper and lower parts, that have the same width. The inner size is designated to model the Hirakata tunnel (Sakayama et al., 2001) where the lining thickness is 1.0 m. The nonuniform thickness pattern is determined from the optimal shape at a lateral pressure ratio of 0.5 obtained from the numerical analysis in Chapter 5.

The results of the member forces and the strain levels when the lateral pressure ratio equals 0.5, are shown in **Figures 4.26**(a)~(d). The results of the axial forces for both patterns are not so different. For the bending moment, the moments at the tunnel crown and the invert of the nonuniform pattern are smaller than those of the uniform pattern, while the nonuniform pattern is larger at the spring line. From the results of strain levels, the tensile strain at the tunnel invert becomes the maximum value for both patterns. Considering only the tensile strain, the tensile strain levels generated in the nonuniform pattern are significantly smaller than those of the uniform pattern at all positions.

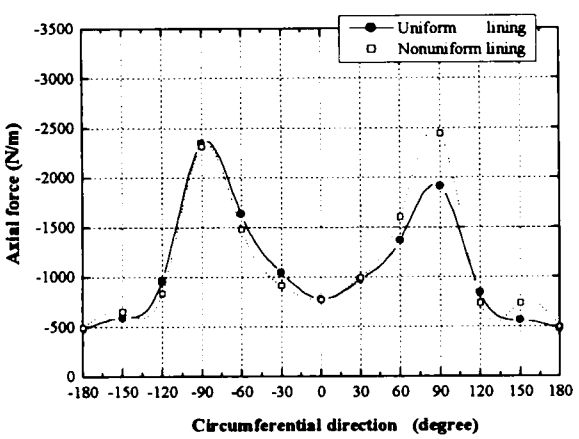

(a) Axial force

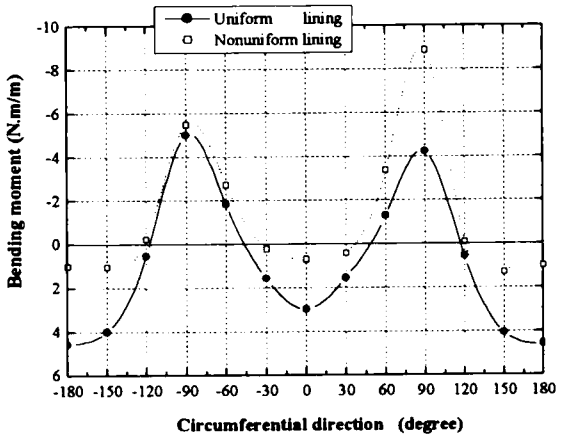

(b) Bending moment

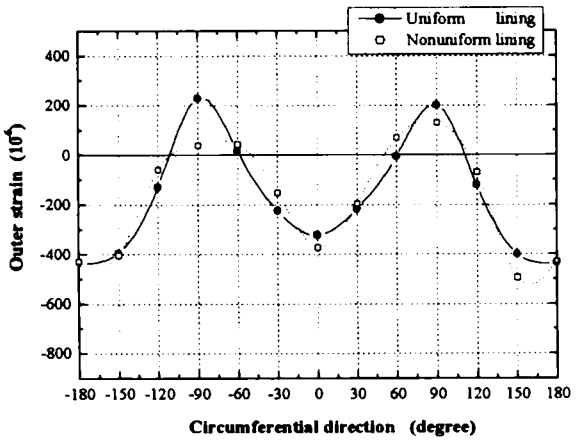

(c) Outer strain

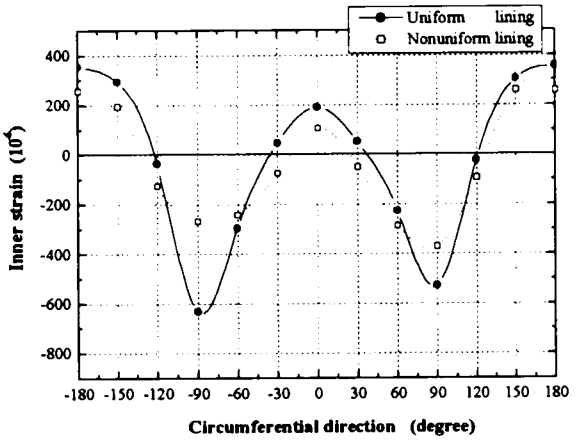

(d) Inner strain

Figure 4.26 Results of tests on the horseshoe-shaped tunnel at $P_H/P_V = 0.5$

From the plots between the tensile strain and the lateral pressure ratios in **Figure 4.27**, it is obvious that the tensile strain at all positions decreases while the lateral pressure ratio increases. That means the horizontal pressure has the important role of supporting the tunnel and increasing the tunnel stability. The largest tensile strain occurs at the tunnel invert and the smallest position is the tunnel crown. For all positions, namely, the tunnel crown, the invert and the spring line, the tensile strain levels occurring in the nonuniform pattern are smaller than those of the uniform pattern.

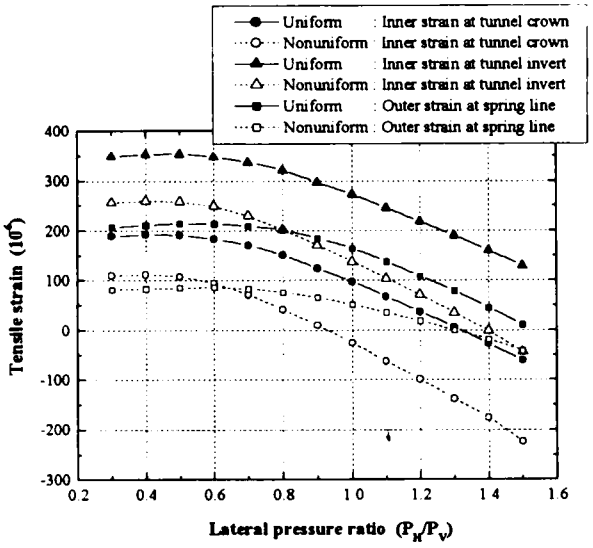

Figure 4.27 Plots between the tensile strain and the lateral pressure ratio of the horseshoe-shaped tunnel

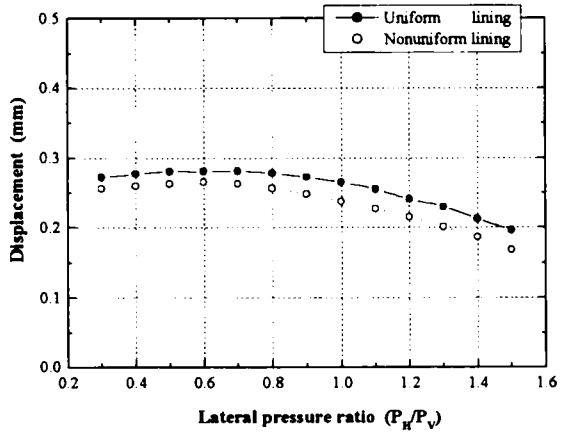

Figure 4.28 Displacement of the tunnel crown for the horseshoe-shaped tunnel

Furthermore, the plots for the tunnel crown displacement are shown in **Figure 4.28**. The results also show that the displacements decrease as the lateral pressure ratio increases. These results agree well with the results of tests on the elliptical tunnels. The results also show that the crown displacements of the nonuniform lining are smaller than those of the uniform lining at all loading steps.

The above results prove the nonuniform pattern, i.e., the optimal shape, is more stable than the uniform one. This is because the strain, especially the tensile strain, and the deformations are smaller than those of the uniform pattern at the same loading level.

4.3.5 Conclusion

The developed two-way loading device can be used to investigate the mechanical behavior of flat-shaped tunnels under the adjustable applied loads. The effects of the lateral pressure ratio, i.e., the ratio between the load in the spring line direction to the load in the crown and the invert direction, can also be investigated by this device. The increasing of the lateral pressure ratio or the load in the spring line direction supports the tunnel lining against vertical earth pressure. For the effects of the tunnel shape, the tendency of the experimental results is the same as those of the model loading tests. The circular tunnel is the most stable pattern and that the stability decreases as the elliptic ratio decreases. The efficiency of the nonuniform lining to improve the stability of the tunnel lining is demonstrated. Therefore, it can be concluded that the nonuniform lining, which is thicker at the spring line and thinner at the crown and the invert, has more potential to withstand external force than the uniform lining.

The nonuniform patterns are calculated from the optimal shapes determined when the lateral pressure ratio equals 0.5 by the optimization program described in Chapter 5. From the test results, the optimal shape also shows the excellent properties for all load cases. This study proves that the stability of the tunnel linings of flat-shaped, elliptical, and horseshoe tunnels, can be effectively improved only by varying the thickness patterns of the tunnel linings. This study also shows the reliability of the proposed analysis method in Chapter 5.

Chapter 5

OPTIMAL DESIGN FOR SEGMENTAL LININGS IN THE SHIELD TUNNELING METHOD

5.1 Introduction

In this chapter, the developed optimization program is first described. Then, an application of the optimization program for analyzing and determining the optimal shape of tunnel linings is demonstrated and discussed. Ordinarily, the inner shape of a road tunnel is controlled by such architectural conditions as the number of road lanes, the size of the ventilation systems, etc. It is necessary to construct the inner surface according to the utilization purposes. In this study, therefore, analyzing the optimal shape for tunnel linings means determining the shape of the outer tunnel surface which produces the maximum stability for the designated inner tunnel surface shape.

Section 5.3 will illustrate how the optimization program can be used to analyze tunnel problems. Analyses of two-way loading tests are carried out to prove the validity and the reliability of the optimization program. Comparisons between the numerical and the experimental results are shown and discussed.

The use of design optimization based on mathematical programming is illustrated in Section 5.3 for improving the design of tunnel linings in the shield tunneling method introduced in the preceding section. The objective is to reduce the tensile stress at the inner surface of the tunnel lining. Reducing the tensile stress means reducing the risk of local cracks at the lining surface in the same way, and at the same time, increasing the stability of the tunnel lining.

5.2 Optimization analysis based on the finite element method

Structural optimization has attracted attention since the days of Galileo. However, interest in structural optimization has increased greatly during the last decade due to the advent of reliable

general numerical analysis methods and the computer power necessary to use them efficiently. This has made it possible to develop general numerical systems for shape optimization. Several researchers (Botkin et al., 1986; Esping, 1984a; Rasmussen, 1990; Stanon, 1986) have published practical and successful applications of general optimization systems for analyzing mechanical and structural problems. The method of structural optimization can also be applied to geotechnical problems, for instance, the optimal shape of underground cavities (see e.g., Horikawa and Kawahara, 1999; Tamura, 2001).

However, the application of structural optimization to the soil-structure problems has not been successful. As mentioned in the previous chapters, varying the lining thickness can increase the stability of a tunnel lining. Thus, the development of a structural optimization program is necessary for obtaining the optimal shape of tunnel lining. Based on the theoretical idea of the optimization scheme proposed by Rasmussen (1991), a structural optimization program has been developed.

The methods and the techniques used in the optimization program, namely, parametric modeling, analysis capability, design sensitivity, a method of problem definition, a flowchart of programming, and program capability are described in this chapter.

5.2.1 Parametric modeling for the optimum design

This section is devoted to a general description of the parametric modeling facilities of the optimization program. Before the parametric modeling facilities are described, some basic concepts of structural design optimization are introduced.

Design variables

In order to introduce the possible design variables of the problem, it is beneficial to define the specifications necessary to perform an ordinary analysis using the finite element method. In general, such an analysis requires information about (Cook et al., 1989):

1. Geometry: the domain shape of the structure, its division into finite elements, and kinematic boundary conditions,

2. Actions: loads acting on the structure,

3. Constitution: physical properties of the materials and properties of the finite elements.

If a design sensitivity analysis and/or optimization is to be performed, a number of design variables must be defined. The design variables will be denoted by

$$a_i,\ i = 1, \ldots, I \tag{5-1}$$

and are assembled in vector **a**. In this analysis, the design variables are shape design variables. They govern the shape of the external boundaries and the surface, or the interior interfaces of the structure. Examples are the surface shape of a two dimensional component and the shapes of interfaces within a structural component made of different materials.

Introduction to the design model concept

Having defined the possible design variables for the structural design problem under consideration, a convenient way of linking them to the finite element analysis model must be available. In the case of sizing and material design variables, the design variables may be linked directly to the analysis model, but this approach is not suitable for shape design variables. Geometrically, shape optimization is much more difficult to handle than sizing optimization, because it involve successive changes in the shape of the model. The following description mainly relates to shape optimization. In the early days of structural shape design sensitivity analyses and optimizations, attempts were made to use the finite element model directly as a design model, i.e., to use nodal coordinates as design variables (see Zienkiewicz and Campbell, 1973). It turns out that this method has at least four serious drawbacks (see e.g., Ding, 1986; Rodrigues, 1988):

The number of design variables can become very large.

- It is difficult to ensure compatibility and slope continuity between boundary nodes.
- It is difficult to maintain an adequate finite element mesh during the domain shape updating process when shape optimization is performed.
- The structural shape design sensitivities might not be accurate unless high order finite element types are used.

Based on these experiences, most computer aided environments for interactive structural shape designs and optimizations are founded on an *important distinction* between the *design model* and the *analysis model,* as demonstrated by, e.g., Braibant and Fleury (1984), Esping (1984b), Rasmussen (1990), and Olhoff et al. (1991).

The design model is a variable description of the domain shape of the structure, but sizing variables can also be linked to the design model. It is very distinct from the finite element model that is used for the analysis.

The design model may consist of so-called design elements as presented by Braibant and Fleury (1984) and Bennett et al. (1985). The boundaries of the design elements can be curves of almost any character, namely, piecewise straight lines, arcs, b-splines with specified degrees of continuity. It is very simple, therefore, to generate relatively complicated geometries with a small number of design elements. The shapes of the boundaries are controlled by a number of control points, also often termed "master nodes". Then, shape design variables can be defined to control the positions of these master nodes, and possible sizing as well as material design variables can be linked to each design element.

Design model concept

The design model concept in this optimization system is based on a *hierarchical parametric design model*, a totally parametric modeling system in which data are initially divided into two categories or levels of increasing complexity, *Level0* and *Level1*.

Level0 is the "ground" level. This level contains geometrical entities, which are independent of other entities in the model. This would typically be points, vectors, and scalar numbers. The master nodes are the *Level0* entities. Other possible nodes that would be *Level0* entities are models of elasticity or thickness. *Level0 is characterized by the property that it is the only level containing real numbers.*

Level1 contains entities which depend only on Level0 information. Boundary curves and surfaces are typical examples. Their shapes are defined solely by the positions of the master nodes. Level1 could contain, for instance, lines, curves, spline lines, etc. The actual shapes of all entities in Level1 are defined by pointers to Level0 information. *Thus, Level1 consists only of the integer type information.*

Design variables and modifiers

The parametric nature of the design model comes automatically from the division of information into interdependent levels. We simply control the model by modifying the entities of Level0. Due to the hierarchical construction of the model, modifications of Level0 entities automatically lead to corresponding changes in Level1. In order to improve the possibility of defining the design space, *data in Level0 are controlled by the use of a so-called modifier*. In these systems, only one type of modifier, namely, translational transformations (also called move directions) are available.

In this framework, the move directions of the optimization systems are realized as translation modifiers coupled with design variables, which specify the magnitude of the translation. Each master node is Level0 information, and therefore, the entire design model changes with the relocation of the master nodes, as illustrated in **Figure 5.1**.

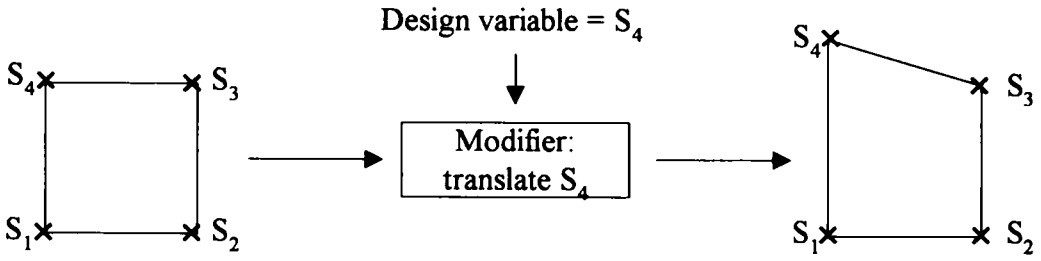

Figure 5.1 Example of translational modifier and design variables affecting the four points S_1, S_2, S_3, and S_4

Mesh generation

The implementation of good algorithms for mesh generation is very important in a structural shape optimization system. It must be possible to specify the desired element sizes within each design element, and the mesh must remain adequate during the updating process for the domain shape when a shape optimization is performed. It may be advantageous to include adaptive mesh generation in the shape optimization system.

Mapping mesh generation techniques are available in two dimensions, but in order to overcome the problem of having to divide the design model into quadrangular elements, as necessary for mapping mesh generation, the use of unstructured free meshing is allowed. A modified version of

an algorithm by George (1988) is implemented. This algorithm can subdivide an arbitrary planer domain into triangles, and in this research, the algorithm is extended to cover curved surfaces.

5.2.2 Analysis capabilities for structural optimization

In this section, a general description of the finite element module in the optimization program is given with focus on the types of analysis problems for which both an analysis and a design sensitivity analysis have been implemented. Furthermore, descriptions of the implemented finite elements are given.

Static stress analysis for structural optimization

The global equilibrium equation of a finite element discretized structural problem with linearly elastic response is given by

$$\mathbf{KD} = \mathbf{F} \tag{5-2}$$

where **K** is the global stiffness matrix, **D** is the nodal displacement vector and **F** is the consistent nodal force vector. These global matrices and vectors are, as is always the case with the finite element method, assembled from element matrices and vectors, i.e.,

$$\mathbf{K} = \sum_{n_e} \mathbf{k}, \quad \mathbf{D} = \sum_{n_e} \mathbf{d}, \quad \mathbf{F} = \sum_{n_e} \mathbf{f} \tag{5-3}$$

Here, **k** is the element stiffness matrix, D is the element nodal displacement vector, f is the consistent element nodal force vector, and n_e is the number of finite elements used to discretize the structure. In this optimization program, the solution for **Equation 5-3** is found by the Crout decomposition scheme described in Dhatt and Touzot (1984).

Finite element types implemented for structural optimization

Two different 2D solid isoparametric finite elements have been implemented in this optimization program as illustrated in **Figure 5.2**. They are all formulated in a unified way for plane stress, plane strain, and axisymmetric situations.

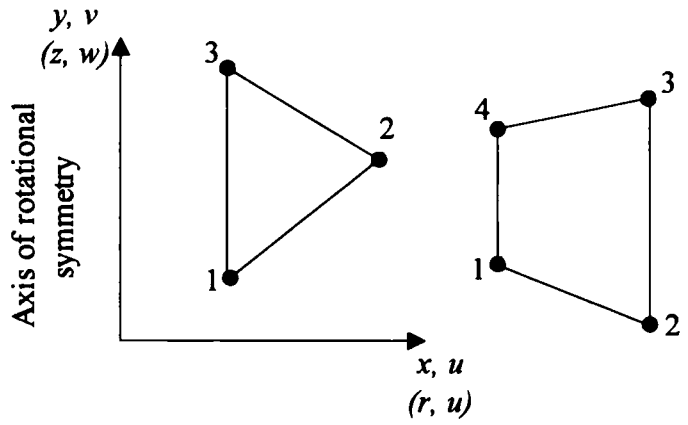

Figure 5.2 Triangular and quadrilateral 2D isoparametric finite elements

The standard approach for using a numerical integration has been chosen because the 2D solid isoparametric finite elements can be formulated in a unified way for both plane stress, plane strain, and axis symmetrical situations, as shown in Appendix B. The 2D solid finite elements are described in detail in Appendix B.

5.2.3 Design sensitivity analysis

In an interactive structural optimization program, a design sensitivity analysis is the basic enabling tool, and expressions for the design sensitivity analysis will be given in this section. The types of design variables for the structural design problems relate to shape, and they are denoted by a_i, $i = 1, \ldots, I$.

Design sensitivity analysis of displacements

In the finite element method based on displacement, the design sensitivity analysis for various criteria is based on sensitivities which are easily computed.

The global equilibrium equation of a finite element discretized structural design problem, with linearly elastic responses, is given by

$$\mathbf{KD} = \mathbf{F} \tag{5-4}$$

where **K** is the global stiffness matrix, **D** is the nodal displacement vector, and **F** is the consistent nodal force vector. The solution for **Equation 5-4** is found by a Gaussian elimination

reformulated in a two-phase process that does not require modifying **K** and **F** simultaneously. It is possible, therefore, to solve **Equation 5-4** for additional load cases, i.e., several right sides, without additional computational effort. The time consuming part of solving **Equation 5-4** is the factorization of global stiffness matrix **K**, in which this matrix is basically divided into product **LU**, where **L** is a lower triangular matrix (with elements only on the diagonal and below) and **U** is a upper triangular matrix. Varieties of this basic decomposition are, for example, the **LDU**, Crout, and Cholesky decomposition schemes (see e.g., Dhatt and Touzot, 1984). In this optimization program, the Crout decomposition scheme has been implemented.

When stiffness matrix **K** has been devided into product **LU**, **Equation 5-4** can be rewritten as

$$\mathbf{LUD} = \mathbf{F} \tag{5-5}$$

Using the broken down form of the stiffness matrix is only necessary when solving a triangular set of equations, which is quite trivial. First, vector **V** is found by a forward substitution, namely,

$$\mathbf{LV} = \mathbf{F} \tag{5-6}$$

Then, displacement vector **D** can be found by a back substitution, namely,

$$\mathbf{UD} = \mathbf{V} \tag{5-7}$$

Having determined displacement vector **D**, the design sensitivity analysis of displacements can now be considered.

The *direct approach* to obtaining design sensitivities of the displacement field *is based on an implicit differentiation of the global equilibrium equation*. If **Equation 5-4** is differentiated with respect to design variable a_i and the terms are rearranged, the following discrete version of the direct approach for displacement sensitivities $\partial \mathbf{D} / \partial a_i$ is obtained, in order words,

$$\mathbf{K(a)}\frac{\partial \mathbf{D}}{\partial a_i} = -\frac{\partial \mathbf{K(a)}}{\partial a_i}\mathbf{D} + \frac{\partial \mathbf{F}}{\partial a_i}, \quad i = 1, ..., I \tag{5-8}$$

Equation 5-8 is of the same form as **Equation 5-4**, so the factorized stiffness matrix **K** in the form **LU** can be reused, and only the new right hand side which is termed the *pseudo load vector*, needs to be calculated before sensitivities $\partial \mathbf{D} / \partial a_i$, for each design variable a_i can be found by

forward and back substitutions. It is seen that the pseudo load vector is the load that must be applied to the structure in order to produce the displacement sensitivity field due to changes in design variable a_i. Derivatives $\partial \mathbf{F} / \partial a_i$ of the force vector are easily calculated (zero for design independent loads), and then the determination of $\partial \mathbf{D} / \partial a_i$ in **Equation 5-8** only requires the calculation of design sensitivities $\partial \mathbf{K} / \partial a_i$ of the stiffness matrix. These derivatives are normally calculated at the element level, i.e.

$$\frac{\partial \mathbf{K}}{\partial a_i} = \sum_{n_e} \frac{\partial \mathbf{k}}{\partial a_i}, \quad i = 1,\ldots,I \tag{5-9}$$

where $\mathbf{k}$ is the element stiffness matrix and n_e is the number of finite elements.

If design sensitivities $\partial \mathbf{k}(\mathbf{a}) / \partial a_i$ are determined analytically before their numerical evaluation, the approach is called an *analytical design sensitivity analysis*. If they are determined by a numerical differentiation, the method is called a *semi-analytical (S-A) design sensitivity analysis*, cf. Zienkiewicz and Campbell (1973), Cheng and Liu (1987), and Haftka and Adleman (1989). In this optimization program, the well-known semi-analytical method described by Cheng and Liu (1987) is used. That is the derivatives of the element matrices are approximated by the first order forward finite difference in a semi-analytical design sensitivity analysis.

$$\frac{\partial \mathbf{k}(a)}{\partial a_i} \approx \frac{\Delta \mathbf{k}(a_1,\ldots,a_I)}{\Delta a_i}$$

$$= \frac{\mathbf{k}(a_1,\ldots,a_i + \Delta a_i,\ldots,a_I) - \mathbf{k}(a_1,\ldots,a_i,\ldots a_I)}{\Delta a_i} \tag{5-10}$$

It is much more attractive to use the method for a semi-analytical (S-A) design sensitivity analysis in this context, as it is easy to implement for many different kinds of shape design variables and finite element types. This is because simple and computationally inexpensive first order finite differences are used. Therefore, the method of the S-A sensitivity analysis is very popular and, in most cases, it is very efficient and reliable.

As a finite difference approximation is involved in this method, both truncation and condition errors may occur. Furthermore, for shape design variables, sufficiently small perturbation Δa_i

must be selected, so that the elements do not become distorted. A strongly distorted mesh may result in changing the accuracy of the solution, and thereby give the derivatives a spurious perturbation Δa_i of shape design variable a_i so that boundary nodes are perturbed less than 1/1000 of the smallest side length of the elements in the structure.

Design sensitivity analysis of stresses

When the displacement design sensitivities have been calculated, the calculation of the stress sensitivities is straightforward as will be shown in the following.

The finite element expression for element stress levels $\sigma(x,y,z) = \{\sigma_x\ \sigma_y\ \sigma_z\ \tau_{xy}\ \tau_{yz}\ \tau_{xz}\}^T$ may be written as

$$\boldsymbol{\sigma}(\mathbf{a}) = \mathbf{E}\boldsymbol{\varepsilon}(\mathbf{a}) = \mathbf{EB}(\mathbf{a})\mathbf{d}(\mathbf{a}) \tag{5-11}$$

where constitutive matrix **E** is independent of the design, **B** is the strain-displacement matrix, and **d** is the element nodal displacement vector.

In this optimization program, the way to calculate the stress design sensitivities is to use a first order forward finite difference approximation.

$$\frac{\partial \sigma}{\partial a_i} \approx \frac{\sigma(\mathbf{a} + \Delta a_i) - \sigma(\mathbf{a})}{\Delta a_i} \tag{5-12}$$

where

$$\sigma(\mathbf{a} + \Delta a_i) = \mathbf{E}\varepsilon(\mathbf{a} + \Delta a_i) = \mathbf{EB}(\mathbf{a} + \Delta a_i)\mathbf{d}(\mathbf{a} + \Delta a_i) \tag{5-13}$$

Perturbed strain-displacement matrix $\mathbf{B}(\mathbf{a} + \Delta a_i)$ is easily calculated and the element displacement vector for the perturbed design can be approximated by a first order Taylor series expansion

$$\mathbf{d}(\mathbf{a} + \Delta a_i) \approx \mathbf{d}(\mathbf{a}) + \frac{\partial \mathbf{d}(\mathbf{a})}{\partial a_i}\Delta a_i \tag{5-14}$$

where the element displacement sensitivities $\partial \mathbf{d} / \partial a_i$ are determined by the solution from **Equation 5-8**.

Simultaneous changes in design variables

The stress levels calculated by the analysis module are denoted by function f_j. If some or all of design variables a_i are changed simultaneously then the linear increment of function f_j can be found using first order Taylor series expansions, namely,

$$\Delta f_j = \nabla^T f_j \Delta \mathbf{a} \tag{5-15}$$

where ∇f_j denotes the gradient vector of f_j and $\Delta \mathbf{a}$ is the vector of changes in design variables a_i, in order words,

$$\nabla f_j = \left(\frac{\partial f_j}{\partial a_1}, \ldots, \frac{\partial f_j}{\partial a_I} \right), \quad \Delta \mathbf{a} = (\Delta a_1, \ldots, \Delta a_I) \tag{5-16}$$

Equation 5-15 is valid due to the differentiability of the above mentioned vector fields and function f_j with respect to the design variables.

These notations are useful for parametric studies of functions f_j as well as for the formulation of optimization problems.

5.2.4 Method of problem definition

This section describes the implementation of a method for formulating problems of mathematical programming in structural optimization systems. The mathematical formulation is based on the so-called bound formulation.

The problem of mathematical programming consists of determining optimum values for the design variables such that they *maximize* or *minimize* a specific function termed the *objective function*, while satisfying a set of geometrical and/or behavioral requirements called *constraint functions*.

The optimization concept of this optimization program is based on the formation and the solution of a sequence of explicit subproblems as opposed to systems that wok with line-search oriented

optimizers. From a theoretical point of view, the subproblem approach is known to be less stable than line-search algorithms: it is often difficult or impossible to prove convergence properties for the algorithm. However, from the system point of view, the subproblem approach is much easier to program and control because it is realized via a fixed sequence of calculations independent of the iteration history. The subproblem approach works reliably in most cases and this method has gained a significant popularity among developers of structural optimization systems.

In the formulation of problems of mathematical programming, only first order approximations are used, i.e., we do not require our analysis module to provide more than first order sensitivities because higher order derivatives are computationally very costly to compute. This does not prevent the use of, for instance, a quasi-Newton approach in which second order approximations are gradually formed based on first order information in several iterations. This optimization program contains the optimizer, namely, a *sequential linear programming algorithm (SIMPLEX).*

The usual mathematical programming formulation for a structural optimization problem is as follows:

Minimize
a

$$g_0(\mathbf{a}) \tag{5-17}$$

Subject to

$$g_j(\mathbf{a}) \le G_j, \qquad j = 1,\ldots,J$$

$$a_i^{min} \le a_i \le a_i^{max}, \qquad i = 1,\ldots,I$$

where I is the number of design variables a_i and J is the number of constraints other than side constraints. Maximization problems are easily included in this form by simply minimizing $g_0(\mathbf{a})$. We notice that non-differentiable functions occur very often in connection with practical structural optimization problems as a result of min/max or max/min criteria.

The objective and the constraint functions g_j,= $j = 0,\ldots,J$, are specified as a part of the problem formulation. These vector functions can be chosen and combined freely among all the analysis results that the system is able to evaluate, as will be described in the next section.

In the interest of simplicity, generality, and, above all, ease of programming, a formulation that enables the system to handle the optimization problem in a uniform way regardless of the blend of local-, integral- and min/max-criteria can be obtained by using the so-called bound formulation (see e.g., Bendøe et al., 1983; Taylor and Bendøe, 1984; and Olhoff, 1989). This technique very elegantly solves the problem of generality, and, assuming an adequate sensitivity analysis scheme, it provides a simple solution to the non-differentiability problem in connection with min/max and max/min problems.

It is assumed that any function g_j in the problem is actually a max over a set of functions (the formulation for max/min problems is completely equivalent), such that

$$g_j(\mathbf{a}) = \max_{k=1,\ldots,p_j} g_{jk}(\mathbf{a}), \quad j = 0,\ldots,J \tag{5-18}$$

Counters $p_j, j = 0,\ldots J$, designate the number of functions among which g_i is given as the max. In the case of, for instance, a max stress criterion, p_j would be the number of nodal stress levels among which the maximum is to be found. Scalar functions are ordinarily just a special case signified by the corresponding $p_j = 1$. This gives us the following form for **Equation 5-17**.

Minimize

$$\mathbf{a} \qquad \max_{k=1,\ldots,p0} g_{0k}(\mathbf{a})$$

Subject to

$$\max_{k=1,\ldots,p0} g_{jk}(\mathbf{a}) \le G_j,\ j = 1,\ldots,J \tag{5-19}$$

$$a_i^{min} \le a_i \le a_i^{max},\ i = 1,\ldots,I$$

Constraint functions $g_j = \mathbf{max}(g_{jk})$, $j = 1,\ldots, J$, do not cause differentiability problems. They may simply be treated separately as

Minimize

$$\mathbf{a} \qquad \max_{k=1,\ldots,p0} g_{0k}(\mathbf{a})$$

Subject to (5-20)

$$g_{jk}(\mathbf{a}) \le G_j, \qquad k = 1,\ldots,p_j, \quad j = 1,\ldots,J$$

$$a_i^{min} \le a_i \le a_i^{max}, \qquad i = 1,\ldots,I$$

This leads to the idea of using a similar approach for the objective function $g_0 = \mathbf{max}(g_{0k})$. In order to make this possible, a new, artificial design variable β and a new artificial objective function $f(\beta)$ are introduced. It is now possible to formulate an equivalent problem in which the previous non-differentiable objective plays the role of a constraint:

Minimize
$\mathbf{a}, \beta$ $\qquad f(\beta)$

Subject to (5-21)

$$g_{0k}(\mathbf{a}) \le f(\beta), \qquad k = 1,\ldots,p_0$$

$$g_{jk}(\mathbf{a}) \le G_j, \qquad k = 1,\ldots,p_j, \quad j = 1,\ldots,J$$

$$a_i^{min} \le a_i \le a_i^{max}, \qquad i = 1,\ldots,I$$

In this formulation, the only way to reduce the value of artificial objective function $f(\beta)$ while fulfilling the constraints, is to simultaneously reduce all the functions comprised in the original objective, in order words, minimize the maximum. Artificial objective function $f(\beta)$ acts as a bound, which suppresses the value of the original objective and gives this technique the name of "bound formula".

The specific form for the artificial objective function $f(\beta)$ has yet to be selected. If a linear method of mathematical programming is used, there is no reason not to select the simplest imaginable function of β :

$$f(\beta) = \beta \tag{5-22}$$

Next, **Equation 5-22** is inserted into **Equation 5-21**. In order to better cope with functions of the varying nature of the scale, we perform a normalization of the problem, namely,

Minimize

$$\underset{\mathbf{a},\beta}{\text{Minimize}} \quad \beta \tag{5-23}$$

Subject to

$$\frac{g_{0k}(\mathbf{a})}{\beta} \le 1, \qquad k = 1,\ldots,p_0$$

$$\frac{g_{jk}(\mathbf{a})}{G_j} \le 1, \qquad k = 1,\ldots,p_j, \quad j = 1,\ldots,J$$

$$a_i^{min} \le a_i \le a_i^{max}, \qquad i = 1,\ldots,I$$

As previously mentioned, counters $p_j, j = 0,\ldots J$, designate the number of functions over which the max for criterion j is to be found. In the case of, for instance, the minimization of the maximum nodal stress, p_j may often be many thousands, and the number of functions on the optimization becomes very large. In order to prevent this, an "active set strategy" can be used, which only includes the nodal stress levels exceeding a certain fraction of the current maximum in the problem.

Tableau 5.23 is valid regardless of the blend of vector functions $g_j, j = 0,\ldots J$, and the numerical operations performed are therefore identical for any problem. Due to this standardization, the bound formulation has greatly simplified the programming of the optimization module.

5.2.5 Structural optimization programming

The structural optimization program is performed in systematic sequences of an analysis, a sensitivity analysis, and an optimization. This is illustrated in **Figure 5.3** where a flow diagram for the calculation procedure is shown.

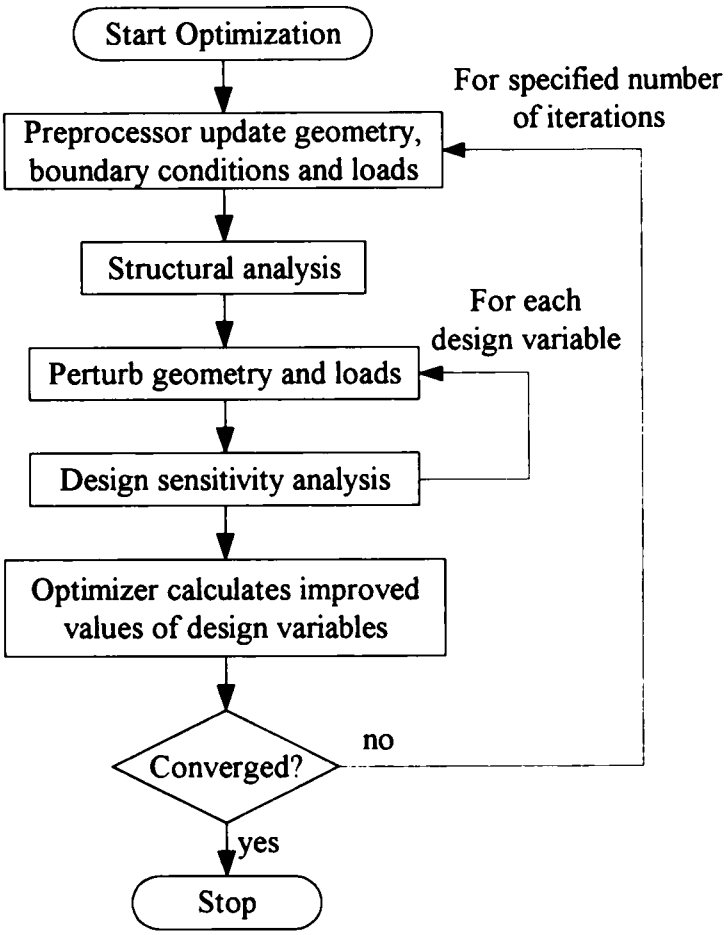

Figure 5.3 Flow diagram for structural optimization

① A preprocessor reads the information from input files and performs a number of operations as follows:

- various checks of the validity of the problem,
- a formation of equation numbers and an imposition of boundary conditions,
- assignments between the parameters of the model and the design variables of the problem.

② A mesh generator, which is in the preprocessor module, reads the current values of the design variables, updates the geometry and generates the current analysis model and force vector.

③ A finite element module performs a traditional displacement-based analysis of the problem and evaluates nodal displacements and stresses.

④ For each design variable, the preprocessor perturbs the geometry and the finite element module evaluates displacement and stress sensitivities.

⑤ A sorting algorithm extracts the necessary results according to the specifications of the objective function and constraints and generates an input tableau for the optimizer.

⑥ A standard SIMPLEX algorithm is used to solve the subproblem and generate an improved set of design variables.

⑦ If the problem has not converged, go back to ②.

5.2.6 Summarization of the developed optimization program

The development of the structural optimization program makes it possible to analyze and design the optimal shape for a tunnel lining. This will be discussed in the next chapter. The developed program is an operational shape optimization system with the following features.

1. One objective function and any number of constraints may be chosen from the material area and the maximum stress at any point, e.g., coordinate direction stress levels, i.e., $\sigma_{xx}, \sigma_{yy}, \sigma_{zz}, \sigma_{rr}, \sigma_{\theta\theta}$, maximum shear stress, principle stress values, and von Misses reference stress.

2. The analysis facilities producing the above mentioned function values incorporate the static linear-elastic analysis

3. The available finite element types are the triangular and the quadrilateral of the isotropic plane stress, the plane strain, and the axisymmetric elements.

4. Boundary conditions can be applied as the specified displacement of a point or an interval of the boundary, zero displacement, roller skate condition, in one or more coordinate, concentrated and distributed forces, and gravitational forces.

5.3 Analyses of the two-way loading tests

In this section, the analytical results of two-way loading tests described in Chapter 4 are shown and discussed. The validity and the reliability of the optimization program are proved by comparing the calculation results with the experimental data.

5.3.1 Optimization model

The design model in the case of the horseshoe-shaped tunnel lining is illustrated in **Figure 5.4**. Since the problem we are going to define is symmetrical in terms of the y-axis, only the right half is modeled. The analysis are carried out for a case in which the lateral pressure ratio equals 0.5, that is to say, a pressure of 60 kPa (P_V) is loaded in the vertical direction and that of 30 kPa (P_H) is loaded in the horizontal direction. The soil boundaries, both of the vertical boundary and the horizontal boundary, are controlled to move uniformly after loading. The iterative calculations between the displacement and the pressure at the boundaries are done for simulating the experimental procedures.

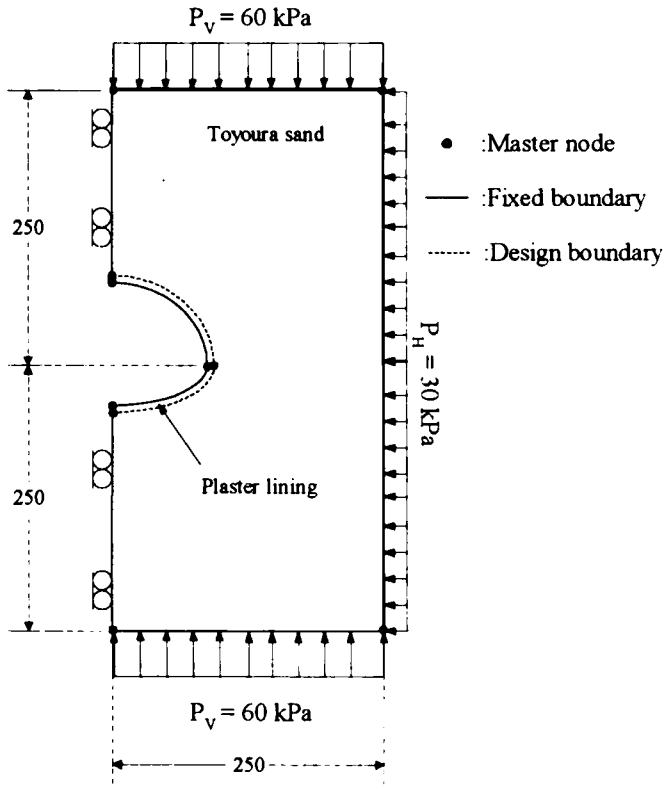

Figure 5.4 Design model for the two-way loading tests

The design model consists of two design elements, namely, sand and lining elements. There are four design boundaries, i.e., boundaries which are allowed to change shape, upper and lower parts of the outer tunnel lining, and two connecting boundaries between the inner and the outer linings. The shape of these boundaries is defined by the position of a number of master nodes. This creates an evident connection between the design variables, the movements of the master nodes, and the shape of the geometry.

In this problem, the direction of the movement of each master node is constrained to follow some predefined move directions as shown in **Figure 5.5**. As shown in the figure, the master nodes are at the tunnel crown, the invert and the spring line. In this problem, design variables a_i, $i = 1,..,I$ being the number of design variables, are the distance of the movements of the master nodes along the associated move directions. The curves of the tunnel lining are designated as elliptic arcs; thus, the movement of the master nodes must satisfy the conditions of the elliptical arc function and must produce the close surface.

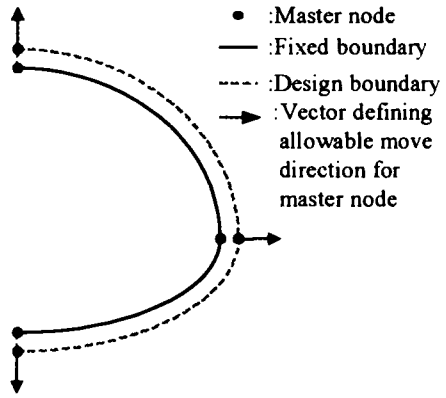

Figure 5.5 Variable design model for tunnel linings

Furthermore, the distribution of finite element nodes on the boundaries and the desired finite element type for each design element must be defined. All necessary specifications including loading conditions, are assigned to the design model and a preprocessor with automatic mesh generation can automatically convert it into a finite element analysis, as shown in **Figure 5.6**. The preprocessor has meshed the design elements with three-node isoparametric plane strain triangular elements.

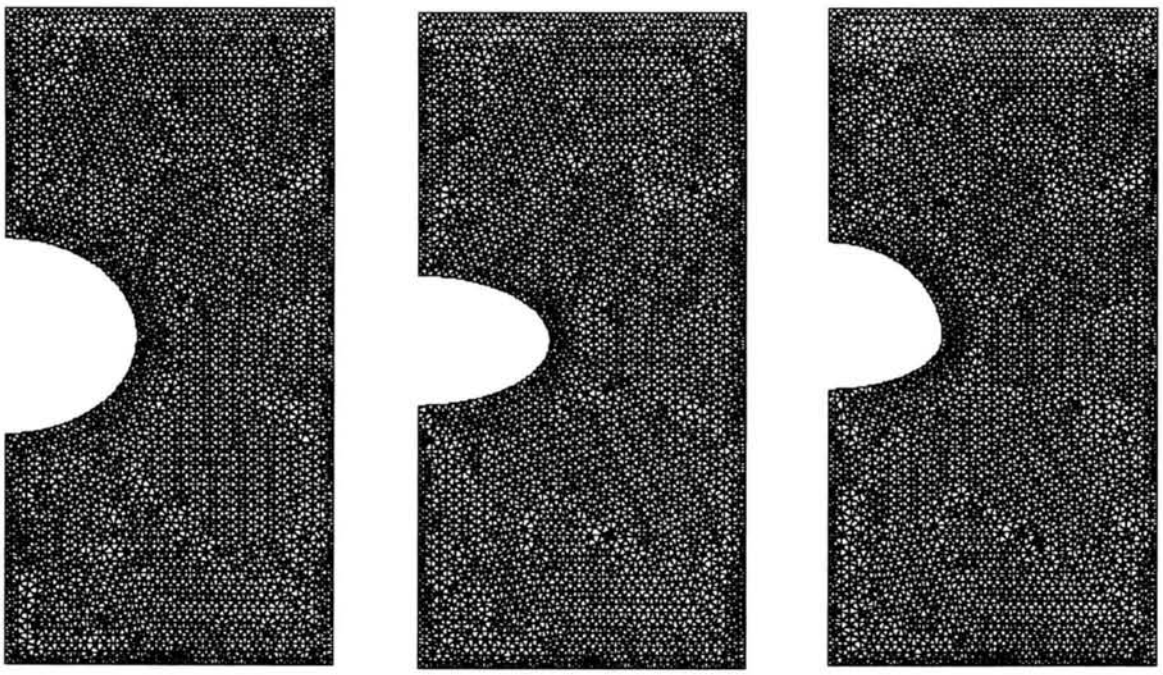

(a) Tunnel with an elliptic ratio of 75%

(b) Tunnel with an elliptic ratio of 50%

(c) Horseshoe-shaped tunnel

Figure 5.6 Finite elment analysis model for the two-way loading tests

Now the design model has been converted into an analysis model. By changing the values of the design variables, the geometry can be changed and many different domain shapes can be obtained. The shape of the structures is thereby described by a set of design variables a_i, $i = 1,.., I$, and the optimal values for the design variables can be determined by the optimization analysis procedure discussed in the next section.

5.3.2 Design criteria

The material properties of the model sand (Toyoura sand) and the model lining (plaster) used in this analysis are shown in **Table 5.1**. The purpose of this analysis is to improve the stability of the tunnel lining without increasing the cross sectional area. The most stable shape or thickness pattern for a tunnel lining is investigated. The stability of the tunnel lining is defined by the intensity of the tensile stress occurring at the lining surface; therefore, the lowest tensile stress means the highest stability. Since all the materials in this analysis are considered to be linear elastic materials, the intensity of the tensile stress has a linear relation with the tensile strain. Moreover, in the experiments, the circumferential strain generated at the lining surface is

measured directly by the strain gauges after loading. Therefore, the objective of the optimization is to minimize the tensile strain of the tunnel's inner surface. The condition of the optimization problem can be summarized as follows:

Minimize the max. tensile strain

Subject to

the cross sectional area $\leq$ initial value

Table 5.1 Material properties of the two-way loading tests

		Toyoura sand	Plaster lining
Unit weight	(kN/m^3)	15.8	8.0
Modulus of elasticity	(MPa)	15.16	1933
Poisson's ratio		0.333	0.218

5.3.3 Results and discussion

The plots for the objective function, namely, the maximum tensile strain of the inner lining, are shown in **Figure 5.7**. The calculation is repeated until the results converge, in order words, the lining shape changes less than 0.01%. The results of the optimal shapes compared with the initial shapes are illustrated in **Figure 5.8**. For all tunnel shapes, namely, with elliptic ratios of 75% and 50% and horseshoe, the optimal shape is thinner at the tunnel crown and the invert, but thicker at the spring line compared with the initial (uniform) thickness pattern. Since the minimum thickness for making the plaster model lining in this analysis is 3 mm, the minimum thickness of the tunnel lining is set as 3 mm. The results show that all patterns yield this limitation. An increase in the spring line causes an increase in the tunnel stiffness and a decrease in the tunnel crown movement such that the earth pressure acting on the tunnel lining is reduced.

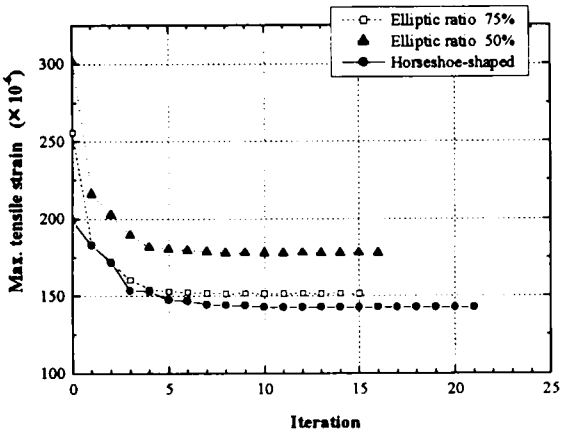

Figure 5.7 Plots between the iteration number and the objective function

Comparisons between the strain levels at the inner surface of the tunnel lining between the analytical and the experimental results are shown in **Figures 5.9**(a)~(c).

The figures show that the calculation results agree well with the experimental data for all tunnel shapes. Thus, it can be concluded that the proposed optimization program can be used to simulate the tunnel problem properly.

The other results of the two-way loading tests in Chapter 4 show the efficiency of the optimal shape for improving the stability of tunnel linings. The data also show that the optimal shape is effective for all ranges of lateral pressure ratios.

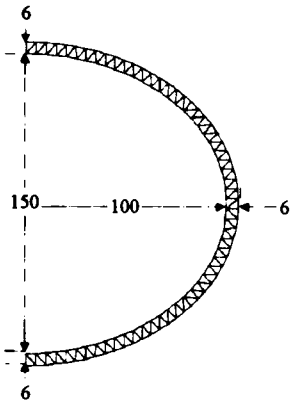

(a) Initial shape of
the 75% elliptical tunnel

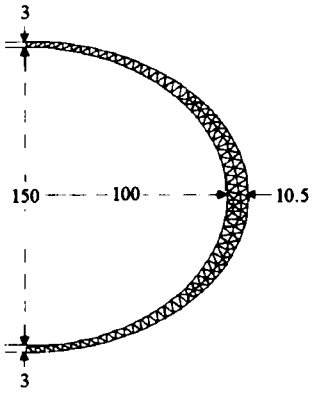

(b) Optimal shape of
the 75% elliptical tunnel

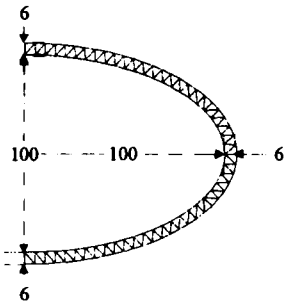

(c) Initial shape of
the 50% elliptical tunnel

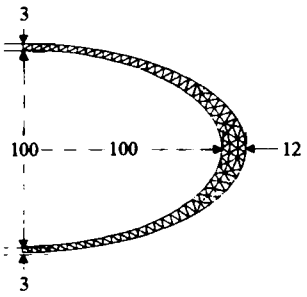

(d) Optimal shape of
the 50% elliptical tunnel

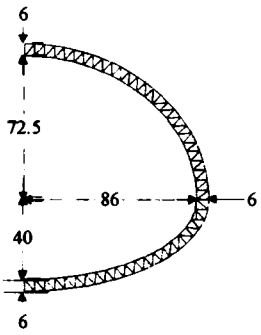

(e) Initial shape of
the horseshoe-shaped tunnel

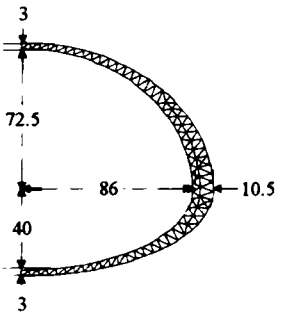

(f) Optimal shape of
the horseshoe-shaped tunnel

Figure 5.8 The Analytical results of the optimal shapes for tunnel linings

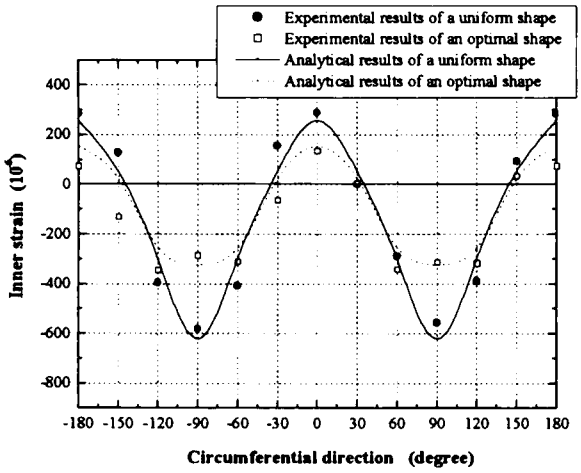

(a) Tunnel with an elliptic ratio of 75%

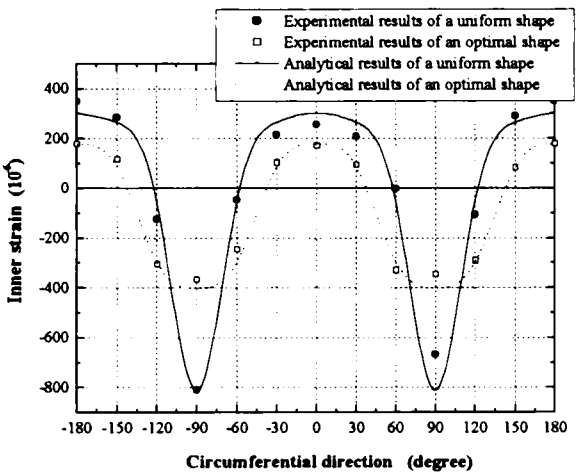

(b) Tunnel with an elliptic ratio of 50%

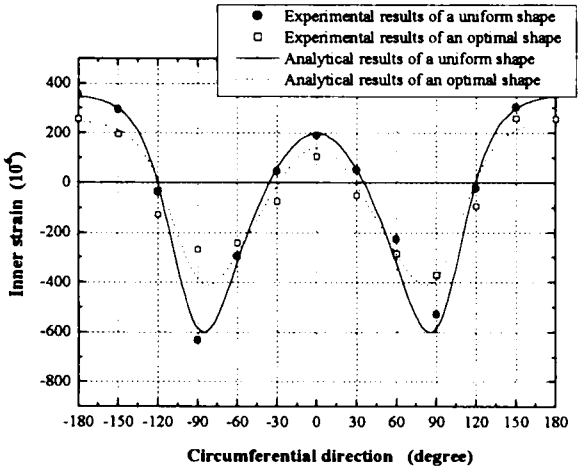

(c) Horseshoe-shaped tunnel

Figure 5.9 Comparisons between the analytical and the experimental results

5.4 Applications to the design of tunnel linings

In this section, the application of the optimization program to improve the design of the road tunnels is illustrated by analyzing an example problem of a road tunnel in the shield tunneling method. The problem used in this section is based on the preliminary design of Hirakata tunnel, as shown in **Figure 5.10** (see Sakayama et al., 2001). Hirakata tunnel is a three-lane road tunnel which was designed as a flat horseshoe-shaped tunnel. The analysis is carried out under the conditions where the overburden depth equals 2B, B is the width of the tunnel, and underground water does not exist.

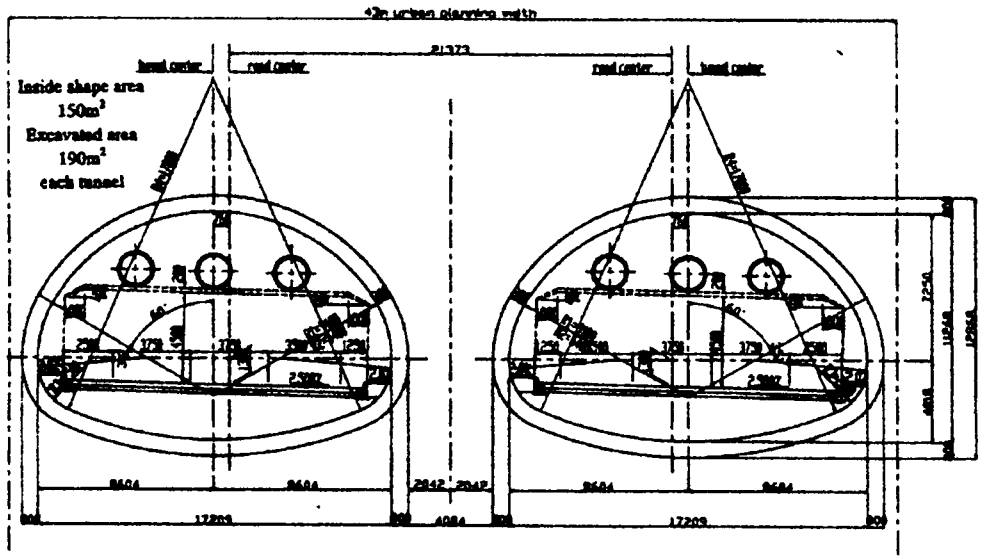

Figure 5.10 Cross section of Hirakata tunnel

5.4.1 Design model

The design model for the horseshoe shaped tunnel is shown in **Figure 5.11**. Since the problem we are going to define is symmetrical in terms of the y-axis only the right half is modeled. The design model consists of two design elements, ground and lining elements. There are four design boundaries, namely, two upper parts and two lower parts of the outer lining.

In this problem, as in the previous section, the direction of the movement of each master node is constrained to follow some predefined move directions, as shown in **Figure 5.5**. In this problem, design variables a_i, $i = 1,..,I$ being the number of design variables, are the distance of the movements of the master nodes along the associated move directions.

The finite element mesh of this problem is generated as shown in **Figure 5.12**. The preprocessor has meshed the design elements with three-node isoparametric plane strain triangular elements.

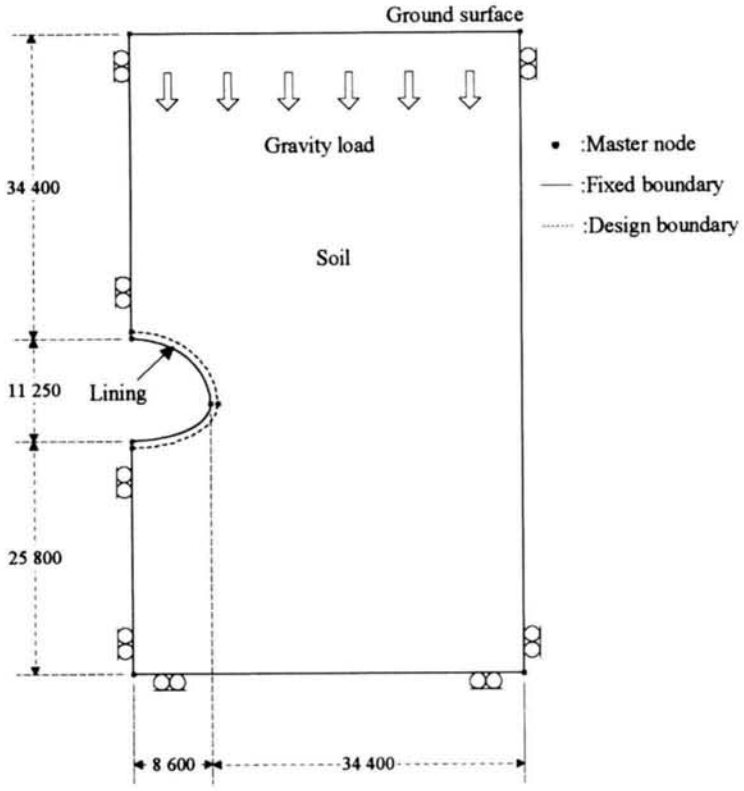

Figure 5.11 Design model of the shield tunneling

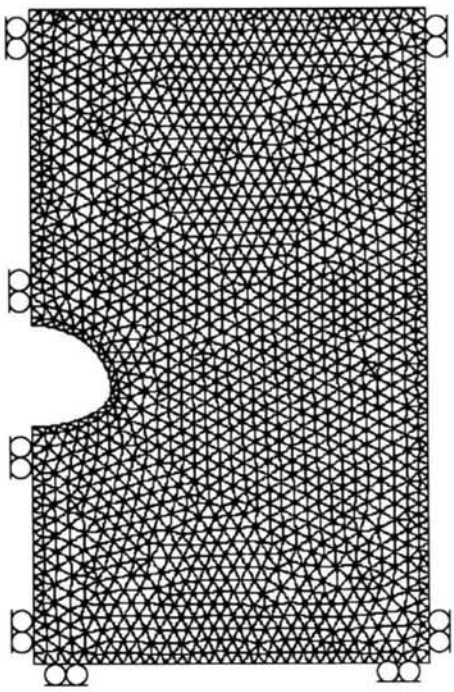

Figure 5.12 Finite element analysis model of the shield tunneling

5.4.2 Design criteria

As is common in tunnel design work, the inside shape of a tunnel is determined by the operation clearance. Therefore, it is only the change of the outside boundary of a tunnel with is thought to determine the optimal shape. As shown in **Figure 5.6**, the master points at the tunnel crown, the spring line, and the invert are allowed to move to determine the optimal shape of the tunnel lining. In order to obtain a calculating shape that is practical for construction work, the shape of the outside lining is constrained to be composed of two elliptical arcs defined by the positions of the master points. The material properties of the soil and the tunnel lining used in this analysis are shown in **Table 5.2**.

Table 5.2 Material properties in the shield tunneling design

		Ground	Lining
Unit weight	(kN/m^3)	19	26
Modulus of elasticity	(MPa)	280	39000
Poisson's ratio		0.40	0.17

The purpose of this analysis is to determine the most stable shape for a tunnel. Typically, linings are made of reinforced concrete that is designed with steel bars to withstand all tensile stress. However, concrete is a significantly weak material against tensile stress. The occurrence of a high level of tensile stress at the tunnel face can cause cracks and a collapse into concrete rubble. For these reasons, the stability of a tunnel lining is defined as the maximum tensile stress. The definition of the optimization problems can be summarized as follows:

Minimize the max. tensile stress

Subject to

the max. compressive stress $\leq$ the allowable compressive stress for bending moment concrete (18 Mpa)

the max. shear stress $\leq$ initial value

the cross sectional area $\leq$ initial value

5.4.3 Results and discussions

The plots for all the constraint functions, namely, the maximum tensile stress, the stress intensity and the lining area, are shown in **Figures 5.13**(a)~(c). Comparisons of all constraint conditions for both shapes are also shown in **Table 5.3**. The maximum tensile stress is reduced from 4.85 to 3.89 Mpa, about 20%, through seven iterations. The results also show that all design constraint conditions are fulfilled after the calculation. The optimal shape determined from the optimization program is illustrated in **Figure 5.14**. Compared with the initial shape that has a uniform thickness of 800 mm, the lining thickness of the optimal shape is thinner at the tunnel crown, but thicker at the spring line and the tunnel invert. The results have the same tendency as the data obtained from both model tests.

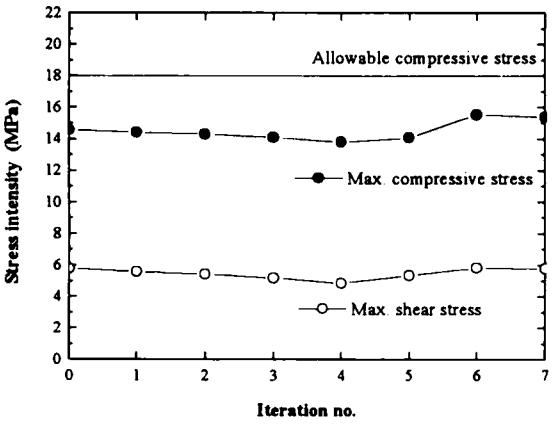

(a) Stress intensity

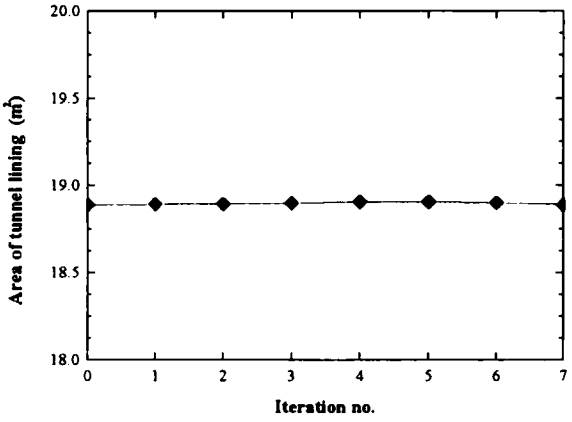

(b) Area of tunnel lining

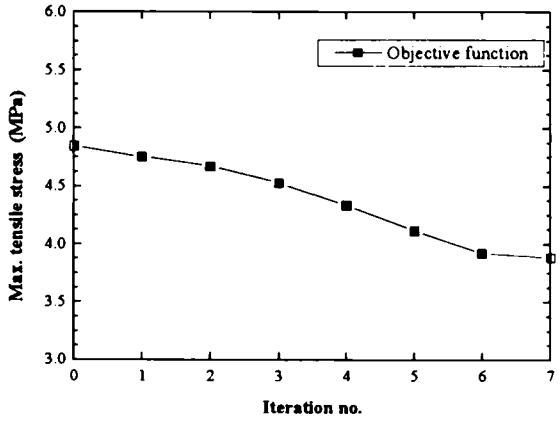

(c) Maximum of tensile stress

Figure 5.13 Constraint functions of the tunnel problem

Table 5.3 Comparisons of the constraint conditions

Constrain conditions		Initial shape	Optimal shape
Max. tensile stress	(MPa)	4.85	3.89
Max. compressive stress	(MPa)	14.56	15.39
Max. shear stress	(MPa)	5.76	5.76
Cross sectional area	(m^2)	18.89	18.89

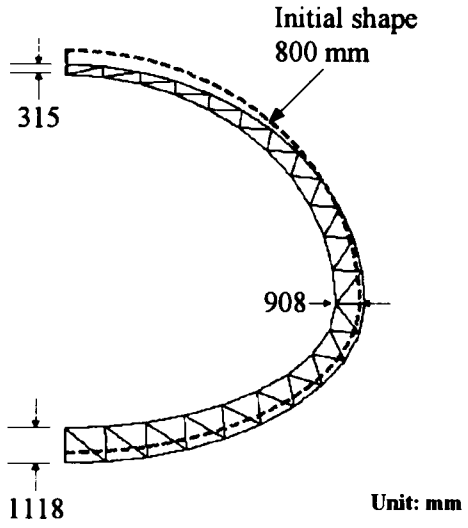

Figure 5.14 Optimal shape of the tunnel lining

5.5 Conclusion

The optimal shape of a tunnel lining can be calculated using the design model concept. The boundary and the surface of a tunnel lining change in each calculation step while searching for the optimal shape. From all the above results, it can be concluded that the optimization program proposed in this paper has the capability of simulating the tunnel problems. Moreover, the optimization program can be applied to improve the stability of tunnel linings.

Chapter 6
SUMMARY AND CONCLUSIONS

The main purposes of this thesis have been (1) to simulate the shield excavation processes by FEM and to use it for the driving control of shield machines, (2) to investigate the mechanical behavior of flat-shaped tunnel linings through model tests, and (3) to develop the optimization program for designing the optimal shape of segmental linings in the shield tunneling method. The results of each chapter are concluded below.

Chapter 3

In this study, it has been shown that the excavation processes of a shield machine can be simulated by remeshing the finite element mesh at every small advancement of the shield. The specially defined elements, namely, the excavated, the interface, and the elongation elements, can be used to model the shield-soil interaction behavior. The properties of the excavated and the interface elements can simply be assumed as the proportion of Young's modulus to the internal friction angle of the surrounding soil. A reduction factor is used to express this relation. The reduction factor can be evaluated by a back analysis from the measurement data in the first step of the excavation.

The driving forces that should be generated for advancing the machine can be calculated by totaling the acting forces on the shield node. The driving moments which program the machine to move along the designated curve can be calculated by summing the products of the nodal forces and the distance from the central point of the machine. From the calculated results of the experimental problems, it has been clarified that the skin friction is a large portion of the total resistant force compared with the earth pressure at the face. At the curved alignment, larger driving forces and driving moments are required in order to control the machine to move along a sharper curve. When considering the earth pressure acting on the skin plate of a shield machine, the pressure increases according to the distance it moves into the soil.

This analysis program can also be applied to investigate the effects of shield excavating on nearby underground structures. The excessive earth pressure acting on the underground structures can be controlled by limiting the distance between the machine and the structure.

The idea of an automatic driving control method for shield machines has been introduced by utilizing the proposed simulation model for the shield excavation processes. In addition to ground properties, the reduction factor should be evaluated carefully in order to obtain accurate results. The reduction factor is thought to correlate with ground and machine types. Continuous research will be conducted until the idea of automatic control systems for shield machines is realized.

Comparisons between the calculated and the measured data show that the required driving forces and the driving moments calculated by the proposed method are slightly greater than those of the actual data from the excavation field. Therefore, it is thought that simulations of the overcutter and the articulated jacks are necessary for obtaining more accurate results.

Chapter 4

The results of model loading tests show that the member forces of a tunnel lining increase when the overburden depth increases. At the same overburden depth, the member forces, namely, the axial force and the bending moment generated in the tunnel lining, grow larger as the tunnel shape becomes flatter, i.e., a smaller elliptic ratio. For a circular tunnel, the axial force is the main supporting force against the acting earth pressure. On the contrary, a flat-shaped tunnel is mainly supported by the bending moment at the spring line. In the case of a uniform lining, the intensity of the member forces, namely, the axial force and the bending moment, can be used effectively to evaluate the stability of the tunnel lining. However, for a nonuniform tunnel, for which the thickness of the tunnel lining is not constant, the intensity of the axial force and the bending moment can not clearly express the stability of the tunnel lining. Thus, the intensity of the stress or the strain generated at the lining surface is instead used to directly evaluate the stability. In this research, the stability of tunnel linings has been evaluated by the intensity of the tensile stress at the surface of the tunnel lining. A lower level of tensile stress means a more stabile tunnel lining. Tensile stress and strain normally occur at the inner surface of the tunnel crown, the invert and the outer surface of the spring line. For a deep overburden depth, the tensile stress at the spring line is dominant. For the same tunnel shape, changes in the thickness pattern cause the stability of

the tunnel lining to change. The thickness pattern, for which the thickness is thicker at the spring line but thinner at the tunnel crown and the invert, is the most stable pattern. This shows that the stability of tunnel linings can be improved by varying the thickness pattern and not increasing the overall lining area.

The newly-developed two-way loading device can be used to investigate the mechanical behavior of flat-shaped tunnels under adjustable applied loads. The effects of the lateral pressure ratio, i.e., the ratio between the load in the spring line direction to the load in the crown and the invert direction, can also be investigated by this device. Increases in the lateral pressure ratio or the load in the spring line direction support the tunnel lining against vertical earth pressure. For the effects of tunnel shape, the tendency in the experimental results is the same as that in the model loading tests, namely, that a circular tunnel shows the most stable pattern and that the stability decreases when the elliptic ratio decreases. The efficiency of nonuniform lining to improve the stability of tunnel linings is demonstrated. It can be concluded that, therefore a nonuniform lining, which is thicker at the spring line and thinner at the crown and the invert, has more potential to withstand external forces than a uniform lining.

Chapter 5

An optimization program, based on the finite element method, has been initially developed to analyze the two-dimensional elasticity of structure problems. However, the program also has the potential to simulate tunnel problems. The validity of the developed program is proved by analyzing two-way loading tests and then comparing the numerical results with the experimental data. The results show that the optimization program can be used effectively to simulate the experiments. Finally, applying the developed program for the purpose of improving the stability of tunnel linings for given conditions is demonstrated. However, several improvements are still necessary in order to refine the developed analysis procedure. These improvements include introducing more sophisticated constitutive equations for materials, simulating the tunnel excavation by stress release, and considering the effects of underground water.

Appendix A

LAW OF SIMILITUDE FOR TUNNEL MODEL TESTS

Model tests are the most popular method used to investigate the mechanical behavior of structures in the field of civil engineering. This is because model tests are more economical than in situ tests which are usually impossible to carry out on a full scale or in the field test. For concrete structures, it is necessary to choose a model material and a size that can best express as close to the some behavior after loading as the prototype structure. In this section, the idea and the concepts of a similitude law for tunnel model tests are proposed and discussed. The proposed method is applied for determining the model properties and the sizes in two-way loading tests, as described in Chapter 4.

To simulate a tunnel structure, the concept of the similitude ratio (N) is widely used. As shown in **Figure A.1**, a model tunnel with a shape $1/N$ times the prototype is loaded under an overburden height $1/N$ times the prototype. However, the model material is ordinarily different from the prototype material. The thickness of the model lining should be determined in order to obtain the same deformation mode as the prototype, which of course is not 1/N times the prototype. The deformation or the deflection of the model lining should be $1/N$ times the prototype; thus, the model material and the size should be determined to reach these objectives.

The tunnel structure is mainly deformed by the bending moment, regardless of the effects of the axial force. Therefore the deflection of the tunnel structure can be expressed by the beam formula, in order words,

$$\delta = \frac{kqL^4}{EI} \tag{A-1}$$

where q is the external load, L is structural length, E is the modulus of elasticity, I is the moment of inertia, and k is the dimensionless value which depends on the load and the boundary conditions.

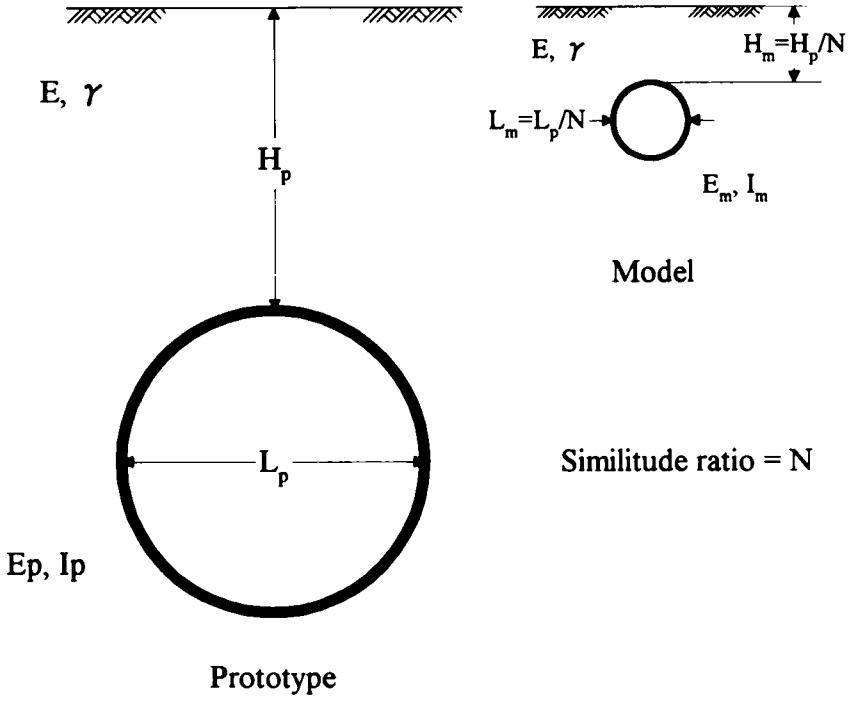

Figure A.1 Simulation of the tunnel structure

As shown in **Figure A.1**, the relations of the model and the prototype can be expressed as $q_m=q_p/N$ and $L_m=L_p/N$. In order to obtain the same deformation mode of the model as the prototype, the relations for both deflections should be

$$\delta_m = \delta_p / N \tag{A-2}$$

The deflection of the model structure can be calculated by the following equation.

$$\delta_m = \frac{kq_m L_m^4}{E_m I_m} = \frac{k(q_p/N)(L_p/N)^4}{E_m L_m^4} = \frac{kq_p L_p^4}{N^5 E_m L_m^4} \tag{A-3}$$

Substituting the **Equation A-3** into **Equation A-2**, the relation of the model and the prototype can be obtained, namely,

$$\delta_m = \frac{kq_p L_p^4}{N^5 E_m L_m^4} = \frac{\delta_p}{N} = \frac{kq_p L_p^4}{N E_m L_m^4} \tag{A-4}$$

Equation A-4 can be rewritten as follows:

$$E_m I_m = E_p I_p / N^4 \tag{A-5}$$

or

$$E_m t_m^3 = E_p t_p^3 / N^4 \tag{A-6}$$

where t_m and t_p are the measurements of thickness for the model and the prototype lining, respectively.

Equation A-6 should be satisfied in order to obtain the reliable test results from the model tests. Thus, the elastic modulus and the size of the model should be chosen to satisfy the above equation. Based **Equation A-6**, the relations between the model and the prototype structure are plotted in **Figures A.2**(a) and (b).

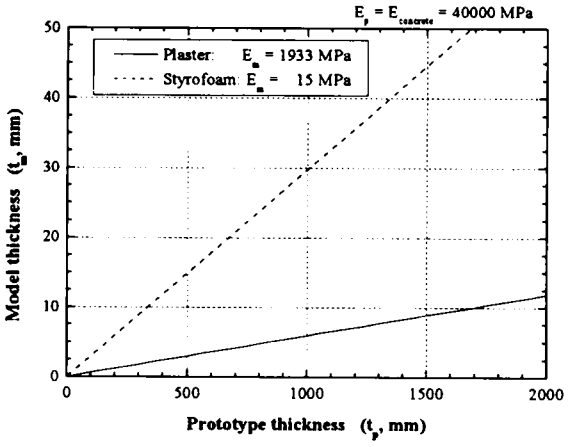

(a) Relations between t_m and t_p

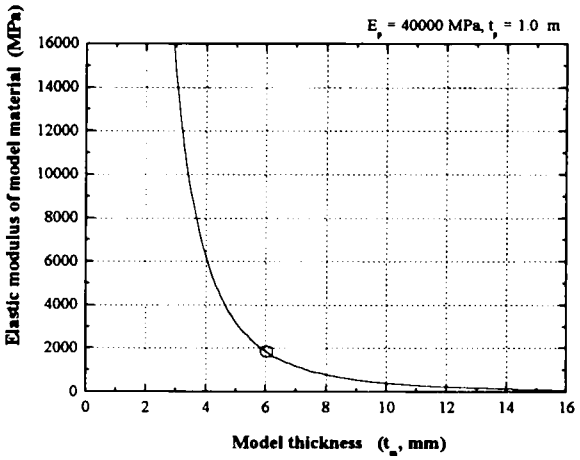

(b) Relation between E_m and t_m

Figure A.2 Similitude law of the bending structure (N=100)

From **Figure A.2**, if plaster with an elastic modulus of 1933 Mpa is used as the model material to simulate a concrete tunnel (E_p=40,000 Mpa, t_p=1.0 m) by a similitude ratio of 100, the thickness of the model lining should be 6 mm. This method is used for designing the model lining in Chapter 4.

The proposed equation is a guideline for designing the shape and the size of the model structures. The accuracy and the reliability of the model tests can be improved by applying this method.

Appendix B

2D SOLID ISOPARAMETRIC FINITE ELEMENTS

Two different 2D finite isoparametric finite elements have been implemented in this optimization program. These isoparametric finite elements are formulated in a unified way for both plane stress, plane strain, and axisymmetric conditions. These elements have 3- and 4-nodes, respectively, and are shown in **Figure B.1**.

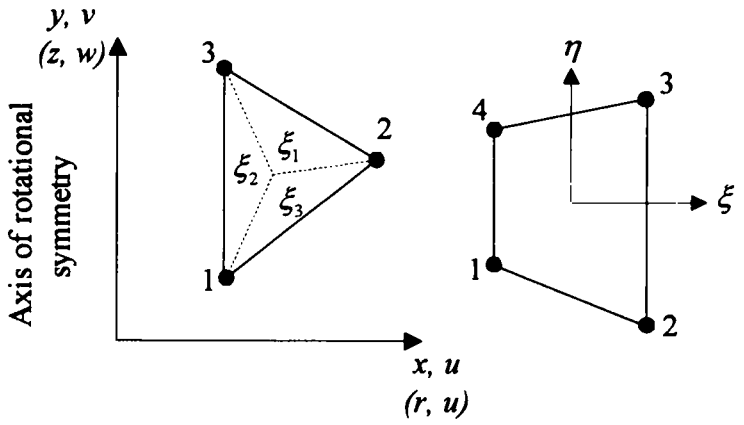

Figure B.1 This figure shows the domain, the node numbering, and the nodal degrees of freedom for the 3-, and 4-node 2D isoparametric finite elements. Local, non-dimensional coordinates ξ, η and area coordinates ξ_1, ξ_2, and ξ_3 are shown for the quadrilateral and triangular elements, respectively

B.1 Shape functions for 2D solid isoparametric finite elements

Within the isoparametric formulation of a finite element with an arbitrary number n of nodal points, the same set of shape functions

$$N_i = N_i(\xi,\eta), \quad i = 1,\ldots,n \tag{B-1}$$

is used for the interpolation of global x, y coordinates from nodal values x_i and y_i and of displacements functions u, v from nodal values u_i and v_i, namely,

$$x = \sum_{i=1}^{n} N_i x_i, \quad y = \sum_{i=1}^{n} N_i y_i \tag{B-2}$$

$$u(x,y) = \sum_{i=1}^{n} N_i u_i, \quad v(x,y) = \sum_{i=1}^{n} N_i u_i \tag{B-3}$$

Shape functions for the 4-node elements are given in **Table B.1**.

Table B.1 Shape functions for the 4-node 2D solid isoparametric elements

$N_1 = \frac{1}{4}(1-\xi)(1-\eta)$	$N_2 = \frac{1}{4}(1+\xi)(1-\eta)$
$N_3 = \frac{1}{4}(1+\xi)(1+\eta)$	$N_4 = \frac{1}{4}(1-\xi)(1+\eta)$

In the case of triangular isoparametric elements, the interpolation functions are conveniently defined in terms of non-dimensional coordinates ξ_1, ξ_2, and ξ_3 within the elements, as shown in **Figure B.1**. Only two of the three dimensionless area coordinates are mutually independent, due to the constraint relation, in other words,

$$\xi_1 + \xi_2 + \xi_3 = 1 \tag{B-4}$$

If ξ_1 and ξ_2 are selected as independent coordinates, the following relations are obtained

$$\xi_1 = \xi, \quad \xi_2 = \eta, \quad \xi_3 = 1 - \xi - \eta \tag{B-5}$$

Derivatives with respect to ξ and η, with constraint in **Equation B-4** taken into account, can be found as

$$\frac{\partial}{\partial \xi} = \frac{\partial}{\partial \xi_1} - \frac{\partial}{\partial \xi_3}, \quad \frac{\partial}{\partial \eta} = \frac{\partial}{\partial \xi_2} - \frac{\partial}{\partial \xi_3} \tag{B-6}$$

The element matrices for the triangular elements can be formulated similarly to the quadrilateral elements by using **Equations B.4-B.6**. The shape function for the 3-node elements are given in **Table B.2**.

Table B.2 Shape functions for the 3-node 2D solid isoparametric elements

$N_1 = \xi_1 \quad N_2 = \xi_2 \quad N_3 = \xi_3$

B.2 Element stiffness matrix

Element stiffness matrix k is given by

$$\mathbf{k} = \int_{\omega} \mathbf{B}^T \mathbf{E} \mathbf{B} |\mathbf{J}| d\omega \tag{B-7}$$

Here, ω is the domain of the finite element in its local coordinate system (see **Figure B.1**) and $|\mathbf{J}|$ is the determinant of Jacobian matrix J which defines the transformation of differentials $d\xi$ and $d\eta$ into dx and dy at each point. Like J, strain-displacement matrix B depends on the coordinates of the nodal points, whereas constitutive matrix E depends only on the constitutive parameters of the assumed linearly elastic material.

For the plane stress and strain conditions, $d\omega = t\, d\xi d\eta$, where t is the thickness of the finite element. For rotational symmetry, $d\omega = 2\pi r\, d\xi d\eta$, For which r is the radius. The axis of rotational symmetry is assumed to be parallel to the y-axis, as shown in **Figure B.1**.

Expressions for Jacobian J and strain-displacement matrix B can be found in a uniform way for the plane stress, the plain strain and the axisymmetric finite elements, if strain vector ε is defined in the following way:

$$\varepsilon(x,y) = \left\{ \varepsilon_x \; \varepsilon_y \; \gamma_{xy} \; \varepsilon_z \right\}^T \tag{B-8}$$

In order to obtain the relations between the standard notations for axisymmetric problems and the notations used here, it should be noted that $y = x$, $z = y$, $w = v$, $\varepsilon_r = \varepsilon_x$, $\varepsilon_z = \varepsilon_y$, $\gamma_{rz} = \gamma_{xy}$, and $\varepsilon_\theta = \varepsilon_z$, as indicated on **Figure B.1**.

Element nodal vector d, containing nodal displacements is given by

$$\mathbf{d} = \left\{ \mathbf{d}_1^T \; \mathbf{d}_2^T \; \ldots \; \mathbf{d}_i^T \ldots \; \mathbf{d}_n^T \right\}^T \tag{B-9}$$

where vector d_i of the nodal degrees of freedom is

$$d_i = \{u_i \; v_i\}^T, \quad i = 1,\ldots,n \tag{B-10}$$

The relation between strain vector ε and displacement vector d is

$$\boldsymbol{\varepsilon} = \mathbf{B}\,\mathbf{d} \tag{B-11}$$

Strain-displacement matrix B can be found to have the following form

$$\mathbf{B} = [\mathbf{b}_1 \; \mathbf{b}_2 \ldots \mathbf{b}_i \ldots \mathbf{b}_n] \tag{B-12}$$

where submatrix b_i, which is associated with nodal point i of the finite element, has taken the form

$$\mathbf{b}_i = \begin{bmatrix} N_{i,x} & 0 \\ 0 & N_{i,y} \\ N_{i,y} & N_{i,x} \\ \dfrac{N_i}{\gamma} & 0 \end{bmatrix}, \quad i = 1,\ldots,n \tag{B-13}$$

The fourth row in b_i is used only in the case of an axisymmetric problem. The derivatives of the shape functions with respect to x and y are given by

$$\begin{Bmatrix} N_{i,x} \\ N_{i,y} \end{Bmatrix} = \begin{bmatrix} \xi_{,x} & \eta_{,x} \\ \xi_{,y} & \eta_{,y} \end{bmatrix} \begin{Bmatrix} N_{i,\xi} \\ N_{i,\eta} \end{Bmatrix} = \boldsymbol{\Gamma} \begin{Bmatrix} N_{i,\xi} \\ N_{i,\eta} \end{Bmatrix}, \quad i = 1,\ldots,n \tag{B-14}$$

where matrix $\boldsymbol{\Gamma}$ is the inverse

$$\boldsymbol{\Gamma} = \mathbf{J}^{-1} \tag{B-15}$$

of the Jacobian

$$J = \begin{bmatrix} x_{,\xi} & y_{,\xi} \\ x_{,\eta} & y_{,\eta} \end{bmatrix} = \sum_{i=1}^{n} \begin{bmatrix} N_{i,\xi} x_i & N_{i,\xi} y_i \\ N_{i,\eta} x_i & N_{i,\eta} y_i \end{bmatrix} \tag{B-16}$$

B.3 Consistent nodal load vector

Consistent element load vector f is given by

$$\mathbf{f} = \int_{\omega} \mathbf{N}^T \mathbf{F}_B |\mathbf{J}| d\omega + \int_{\chi} \mathbf{N}^T \mathbf{F}_S |\mathbf{J}| d\chi \tag{B-17}$$

where ω is the domain of the finite element in its local coordinate system, F_B represents body forces, χ is the boundary described in curvilinear, non-dimensional ξ or η coordinates for the element at which boundary forces F_S are applied, and N contains shape functions N_i. In the boundary integral, N and $|\mathbf{J}|$ are evaluated by χ. For the plane stress and strain conditions, $d\chi = t\, d\chi$, where t is the thickness of the finite element; for rotational symmetry, $d\chi = 2\pi r\, d\chi$, in which r is the radius.

B.4 Consistent and lumped mass matrices

Consistent element mass matrix m is given by

$$\mathbf{m} = \int_{\omega} \rho \mathbf{N}^T \mathbf{N} |\mathbf{J}| d\omega \tag{B-18}$$

Here, ω is the domain of the finite element described in curvilinear, non-dimensional $\xi - \eta$ coordinates for the element (see **Figure B.1**). ρ is the mass density, N contains shape functions N_i, and $|\mathbf{J}|$ is the determinant of Jacobian matrix J.

Lumped mass matrices are used in this analysis program. They are generated using the popular HRZ lumping scheme (see Cook, et al., 1989). The idea of this method is to use only the diagonal terms of the consistent mass matrix, but to scale them down in such a way that the total mass of the element is preserved. The procedural steps are as follows:

- Computer only the diagonal coefficients m_{ii} of the consistent mass matrix.
- Compute the total mass of element m.

- Computer a number s by adding diagonal coefficient m_{ii} associated with the translational d.o.f. (degree of freedom), but not the rotational d.o.f, if any, that are mutually parallel and in the same direction. The number of these translational d.o.f. is denoted by x.

- Scale all the diagonal coefficients by multiplying them by the ratio xm/s, thus preserving the total mass of the element.

This HRZ lumping procedure is used for all the elements in the analysis program when generating lumped mass matrices.

B.5 Element initial stress stiffness matrix

In the derivation of element initial stress stiffness matrices, it is convenient to reorder nodal degrees of freedom by introducing element displacement vector $\mathbf{d}^*$, where the translational d.o.f. are reordered so that first all x-direction d.o.f. are given, and then y, as follows

$$\mathbf{d}^* = \{u_1\ u_2 \ldots u_i \ldots u_n\ v_1\ v_2 \ldots v_i \ldots v_n\}^T \tag{B-19}$$

Relating the d.o.f. to the reordered element vector $\mathbf{d}^*$, the element initial stress stiffness matrix $\mathbf{k}_\sigma$ for the 2D isoparametric finite elements is given by

$$\mathbf{k}_\sigma = \int_\omega \mathbf{G}^T \mathbf{S} \mathbf{G} |\mathbf{J}| d\omega \tag{B-20}$$

Here, ω is the domain of the finite element in its local coordinate system (see **Figure B.1**) G is a matrix obtained by an appropriate differentiation of shape function N_i, S is a matrix of the initial stress level, and $|\mathbf{J}|$ is the determinant of Jacobian matrix J.

Matrix G is given by

$$\mathbf{G} = \begin{bmatrix} \mathbf{g} & \mathbf{0} \\ \mathbf{0} & \mathbf{g} \end{bmatrix} \tag{B-21}$$

where each submatrix g is given by

$$\mathbf{g} = \begin{bmatrix} N_{i,x} \\ N_{i,y} \end{bmatrix}, \quad i = 1,\ldots,n \tag{B-22}$$

Stress matrix S is given by

$$\mathbf{S} = \begin{bmatrix} \mathbf{s} & \mathbf{0} \\ \mathbf{0} & \mathbf{s} \end{bmatrix} \tag{B-23}$$

where each submatrix s is defined as

$$\mathbf{s} = \begin{bmatrix} \sigma_x & \tau_{xy} \\ \tau_{xy} & \sigma_y \end{bmatrix} \tag{B-24}$$

Here, σ_x, τ_{xy}, etc., are stress level found by the initial static stress analysis.

B.6 Gauss quadrature

The Gauss integration rules used for the 2D isoparametric finite elements are given in **Table B.3**.

Table B.3 Gauss quadrature used for the 2D solid isoparametric finite elements

	Integration rule			
Element type	$\mathbf{k}$	$\mathbf{m}$	$\mathbf{k}_\sigma$	ε, σ
3-node	1-point	1-point	1-point	1-point
4-node	4-point	4-point	1-point	1-point

REFERENCES

The references are listed alphabetically according to the last name of the author.

Akagi, H., and Komiya, K. (1993). Finite element analysis of the stress-deformation behavior considering the execution procedures during shield work, *Journal of Geotechnical Engineering*, JSCE **483**, Ⅲ-25: 59-68. (in Japanese)

Bendsøe, M.O., Olhoff, N., and Taylor, J.E. (1983). A variational formulation for multicriteria structural optimization, *Journal of Structural Mechanics* **11**, 523-544.

Bennet, J.A., and Botkin, M.E. (1985). Structural shape optimization with geometric description and adaptive mesh refinement, *AIAA Journal* **23**, 3: 458-464.

Botkin M.E., Yang R.J., and Benet J.A. (1986). Shape optimization of three-dimensional stamped and solid automotive components, *The Optimum Shape Automated Structural Design*, New York, Plenum Press.

Boussinesq, J. (1883). Application des potential à l'etude de l'equilibre et du mouvement des solides elastiques, Paris, Gauthire-Villars. (in France)

Braibant, V., and Fleury, C. (1984). Shape optimal design using b-splines, *Computer Methods in Applied Mechanics and Engineering* **44**, 247-267.

Cao, D., Konda, T., and Nishimura K. (1993). The basic study on the behavior of large-section with flat tunnel lining, *Proceedings of Annual Conference of the Japan Society of Civil Engineers* **48**, 3B: 252-253. (in Japanese)

Cheng, G., and Liu, Y. (1987). A new computational scheme for sensitivity analysis, *Engineering Optimization* **12**, 219-235.

Cook, R.D., Malkus, D.S., and Plesha, M.E. (1989). *Concepts and applications of finite element analysis, 3rd ed.*, New York, Wiley & Sons.

Das, B. M. (1994). *Principal of Geotechnical Engineering, 3rd ed.*, Boston, PWS, 44, 301, 320.

Date K., Igarashi H., Sasakura T., and Tateyama K. (1998). Evaluation of Posture Change Characteristics of a Multi-Faced Shield Machine, *Journal of Geotechnical Engineering*, JSCE **554**, VI-37: 1-13. (in Japanese)

Dhatt, G., and Touzot, G. (1984). *The Finite element method displayed*, New York, Wiley & Sons.

Ding, Y. (1986). Shape optimization of structures: a literature survey, *Computers & Structures* **40**, 6: 1461-1467.

Drucker, D. C. and Prager, W. (1952). Soil Mechanics and Plasticity Analysis in Limit Design, *Quarterly of Applied Mathematics* **10**, 157-162.

Esping B.J.D. (1984a). The OASIS structural optimization system, *Computers & Structures* **23**, 367-377.

Esping, B.J.D. (1984b). Minimum weight design of membrane structures using eight node isoparametric elements and numerical derivatives, *Computer & Structures* **19**, 4: 591-604.

Fujita, K. (1989). Underground construction, tunnel, underground transportation, Special lecture B., *Proceedings of 12th International Conference on Soil Mechanics and Foundation Engineering*, Rio de Janeiro, **5**: 2159-2176.

Furuyama, M. et al. (1980). Monitoring of ground displacement in shield tunneling work, *Proc. 15th Annual Meeting for Geotechnical Engineering*, JSCE, 1549-1552. (in Japanese)

George, P.L. (1988). Modulef: Génération automatique de maillages, *Collection Dedactique*, edité par Institut National de Racherache en Informatique et en Automatique, 75-80. (in France)

Haftka, R.T., and Adelman, H.M. (1989). Recent developments in structural sensitivity analysis, *Structural Optimization* **1**, 127-151.

Hergarden, H.J., Poel, J.T., and Schrier, J.S. (1996). Ground movements due to tunneling: Influence on pile foundation, *Proceedings of the International Symposium on Geotechnical Aspects of Underground Construction in Soft Ground*, Mair & Taylor (Eds.), Rotterdam, Balkema, 519-524.

Hisatake M., and Shibuya T. (1999). Error characteristics of tunnel model test of two-dimensions, *Proceedings of Annual Conference of the Japan Society of Civil Engineers* **54**, 3B: 30-31. (in Japanese)

Hisatake M., and Shibuya T. (2000). Optimum design of tunnel model device based on genetic algorithm, *Proceedings of Tunnel Engineering* **10**, *JSCE*, 25-32. (in Japanese)

Horikawa S., and Kawahara, M. (1999). Optimal shape analysis of tunnel, *Proceedings of Annual Conference of the Japan Society of Civil Engineers* **54**, 3B: 760-761. (in Japanese)

Ishimura, T., and Inokuma, A. (1992). Centrifuge model test on the load acting on the elliptical tunnel, *Proceedings of Annual of the Japan Society of Civil Engineers* **47**, 3B: 90-91. (in Japanese)

Imanishi, H., Ogata, T., Hongo, T., Mandai K., and Takai, T. (1999). Development of an experimental device consisted of a pile of aluminum sticks taking account of tunnel excavation in the loosen zone, *Proceedings of Annual of the Japan Society of Civil Engineers* **54**, 3B: 250-251.

Inokuma, A. and Fujimoto, A. (1996). An improvement of FEM analysis in ground settlement prediction in shield tunneling, *Proceedings of the International Symposium on Geotechnical Aspects of Underground Construction in Soft Ground*, Mair & Taylor (Eds.), Rotterdam, Balkema, 537-542.

Japanese Society of Civil Engineers (1996). *Japanese standard for shield tunneling, 3rd ed.* Tokyo, Maruzen, 30-77.

Kimura, S., and Koizumi, A. (1999). A design method of shield tunneling taking into account of the interaction between the lining and the ground, Journal *of Geotechnical Engineering*, JSCE **624**, III-47: 123-134. (in Japanese)

Nagamura, N. et al. (1986). Ground behavior around tunnel in large section slurry type shield tunneling work, Proc. 41st Annual Academic Lecture Meeting, JSCE, 851-852. (in Japanese)

Nagayama, T., Nagayama N., and Nagajima, M. (1988). Analysis of stiff soil behavior caused by tunnel driving with pressurized shield machine, Proceedings of Japan Society of Civil Engineers, JSCE, 379: 133-141. (in Japanese)

Mair, R.J., Gunn, M.J., and O'Reilly, M.P. (1981). Ground movements around shallow tunnels in soft clay, *Proc. 10th International Conference on Soil Mechanics and Foundation Engineering*, Stockholm, **1**: 323-328.

Makata, H. (1980). Ground settlement prevention measures is sewer shield tunneling work (Part 1), *Bulletin of Japan Sewage Works Association* **17**, JSA, 191: 9-19. (in Japanese)

Mori, A. and Akagi, K. (1980). Consolidation settlement due to disturbance of cohesive soil in shield tunnelling, *Tunnel and Underground* **11**, 8: 563-567. (in Japanese)

Mori, A. and Akagi, K. (1983). Consolidation phenomena due to soil disturbance under undrained shear deformation, *Journal of Japan Society of Civil Engineers*, JSCE, 117-125. (in Japanese)

Okano, N., Konishi, S., Ihara, S., Arai, Y., and Ogawa, S., (1997). Experimental study on loads acting on shield tunnel, *Proceedings of Annual Conference of the Japan Society of Civil Engineers* **52**, 3B: 212-213.

Olhoff, N. (1989). Multicriterion structural optimization via bound formulation and mathematical programming, *Structural Optimization* **1**, 11-17.

Olhoff, N., Bendsøe, M.P., and Rasmussen, J. (1991). On CAD-integrated structural topology and design optimization, *Computer Methods in Applied Mechanics and Engineering* **89**, 259-279.

Onishi, H., Kobayashi, M., Koizumi, A., Hanafusa, K., and Takamoto, H. (1996). Experimental studies on the design method of the elliptical and rectangular cross sectioned shield tunnel, *Proceedings of Annual Conference of the Japan Society of Civil Engineers* **51**, 3B: 208-209. (in Japanese)

Ooishio, Y. (1989). *Study on Cutter Torque Mechanism of Shield Machine*, Ph.D. Thesis, Kyoto Univ., Japan. (in Japanese)

Rasmussen, J. (1990). The structural optimization system CAOS, *Structural Optimization* **2**, 109-115.

Rasmussen J. (1991). Shape optimization and CAD, International Journal of Systems Automation: Research and Applications **1**, 33-45.

Rodrigues, H.C. (1988). Shape optimal design of elastic bodies using a mixed variational formulation, *Computer Methods in Applied Mechanics and Engineer* **69**, 29-44.

Sakajo, S., Toshimura, T., and Kamimura M. (1996). Analytical and geotechnical consideration on ground settlement induced by tail void closure of shield tunnel construction, *Proceedings of the International Symposium on Geotechnical Aspects of Underground Construction in Soft Ground*, Mair & Taylor (Eds.), Rotterdam, Balkema, 585-590.

Sakayama, Y., Kodama, T., Sunami A., and Hashimoto T. (2001). Study on large section shield tunneling for practical use, *Proceedings of the International Symposium on Modern Tunneling Science and Technology*, Adachi, Tateyama and Kimura (Eds.), Kyoto, Balkema, 681-686.

Sakurai, S., Kawashima, I., Kawabata, Y., and Saragai, A. (1994). Model tests on deformation and loosening pressure of shallow tunnel, *Journal of Geotechnical Engineering*, JSCE **487**, III-26: 271-274. (in Japanese)

Simpson, B., Atkinson, J.H., and Jovicic, V. (1996). The influence of anisotropy on calculations of ground settlements above tunnels, *Proceedings of the International Symposium on Geotechnical Aspects of Underground Construction in Soft Ground*, Mair & Taylor (Eds.), Rotterdam Balkema, 591-594.

Stalebrass, S.E., Jovicic, V., and Taylor, R.N. (1994). The influence of recent stress history on ground movements around tunnels, *Proceedings of International Symposium on Pre-Failure Deformation Characteristics of Geomaterials*, Shibuya, Mitachi & Miura (Eds.), Rotterdam, Balkema, **1**: 615-620.

Stanon, E.L. (1986). Geometric modeling for structural and material shape optimization, *The Optimum Shape Automated Structural Design*, New York, Plenum Press.

Sugihara, Y., Igarashi, H., and Sasakura T. (1997). Centrifuge model tests for earth pressure on doubly-faced shield tunnel, *Proceedings of Annual Conference of the Japan Society of Civil Engineers* **52**, 3B: 202-203. (in Japanese)

Sugimoto, M. (1994). Modeling of Acting Load on Shield, *Int. Symposium on Underground Construction in Soft Ground*, New Delhi, Balkema, 135-138.

Sukiyama, H., and Goto, S. (1999). Centrifuge test on the mechanism of lining stresses, *Proceedings of Annual Conference of the Japan Society of Civil Engineers* **54**, 3B: 212-213. (in Japanese)

Takamoto, H., Kobayashi, M., and Koizumi, A. (1996). Model experiment on the design method of the elliptical and rectangular cross sectioned shield tunnel, *Proceedings of Annual Conference of the Japan Society of Civil Engineers* **51**, 3B: 306-307. (in Japanese)

Tamura, T., and Saito J. (2001). Optimal shape of underground structure, *Proceedings of the International Symposium on Modern Tunneling Science and Technology*, Adachi, Tateyama and Kimura (Eds.), Kyoto, Balkema, 69-72.

Taylor, J.E., and Bendsøe, M.P. (1984). An interpolation of min-max structural design problems including a method for relaxing constraints, *International Journal of Solids and Structures* **20**, 301-314.

Terzaghi, K. (1943). *Theoretical soil mechanics*, New York, Wiley & Son, 194-197.

Westergaard, H.M. (1938). A problem of elasticity suggested by a problem in soil mechanics: soft material reinforced by numerous strong horizontal sheets, *in Contribution to the Mechanics of Solids*, Stephen Timoshenko 60th Anniversary Vol., New York, Macmillan.

Yamada, K. et al. (1979). Analysis of ground settlement due to shield tunneling work by finite element method. *Proc. 14th Annual Meeting for Geotechnical Engineering, JSCE,* 817-820. (in Japanese)

Zienkiewicz, O.C., and Campbell, J.S. (1973). Shape optimization and sequential linear programming, *Optimum Structural Design, Theory and Applications,* Gallangher, R.H., and Zienkiewicz, O.C. (Eds.), London, Wiley & Sons, 109-102.